ISTANBUL TECHNICAL UNIVERSITY ★ GRADUATE SCHOOL

PHYSICAL LAYER SECURITY PERFORMANCE OF SATELLITE NETWORKS

Ph.D. THESIS

Olfa BEN YAHIA

Department of Electronics and Communications Engineering

Telecommunications Engineering Programme

JULY 2022

ISTANBUL TECHNICAL UNIVERSITY ★ GRADUATE SCHOOL

PHYSICAL LAYER SECURITY PERFORMANCE OF SATELLITE NETWORKS

Ph.D. THESIS

Olfa BEN YAHIA
(504162314)

Department of Electronics and Communications Engineering

Telecommunications Engineering Programme

Thesis Advisor: Prof. Dr. Güneş KARABULUT KURT
Thesis Co-Advisor: Doç. Dr. Eylem ERDOĞAN

JULY 2022

İSTANBUL TEKNİK ÜNİVERSİTESİ ★ LİSANSÜSTÜ EĞİTİM ENSTİTÜSÜ

UYDU AĞLARININ FİZİKSEL KATMAN GÜVENLIK BAŞARIMI

DOKTORA TEZİ

Olfa BEN YAHIA
(504162314)

Elektronik ve Haberleşme Mühendisliği Anabilim Dalı

Telekomünikasyon Mühendisliği Programı

Tez Danışmanı: Prof. Dr. Güneş KARABULUT KURT
Eş Danışman: Doç. Dr. Eylem ERDOĞAN

TEMMUZ 2022

Olfa BEN YAHIA, a Ph.D. student of ITU Graduate School student ID 504162314, successfully defended the dissertation entitled “PHYSICAL LAYER SECURITY PERFORMANCE OF SATELLITE NETWORKS”, which she prepared after fulfilling the requirements specified in the associated legislations, before the jury whose signatures are below.

Thesis Advisor : **Prof. Dr. Güneş KARABULUT KURT** ....
Istanbul Technical University

Co-advisor : **Doç. Dr. Eylem ERDOĞAN** ....
Istanbul Medeniyet University

Jury Members : **Prof. Dr. Sıddıka Berna ÖRS YALÇIN** ....
Istanbul Technical University

Doç. Dr. Enver ÖZDEMIR ....
Istanbul Technical University

Doç. Dr. Tunçer BAYKAŞ ....
Kadir Has University

Prof. Dr. Halim YANIKÖMEROĞLU ....
Carleton University

Prof. Dr. İbrahim ALTUNBAŞ ....
Istanbul Technical University

Date of Submission : 24 May 2022
Date of Defense : 06 July 2022

To my family,

FOREWORD

I reserve these lines sign of gratitude and appreciation to all those who contributed directly or indirectly to the realization of this work.

I express my deep sense of respect and gratitude to my supervisors **Prof. Güneş KARABULUT KURT** and **Prof. Eylem ERDOĞAN** for believing in my abilities to accomplish this research work. I am deeply grateful for their guidance, advice, encouragement, and continuous support during my Ph.D. journey. They granted me great flexibility and freedom during my research. They taught me academic knowledge, research, and writing skills. It is my honor to have this opportunity to do research under their supervision.

I take this opportunity to express my special gratitude to our collaborators Prof. İbrahim ALTUNBAŞ and Prof. Halim YANIKOMEROGLU for their instructive and valuable contributions during the progression of the dissertation. It is a great honor to collaborate with them.

I would like to thank the members of the thesis steering committee, Prof. Sıddıka Berna ÖRS YALÇIN, Prof. Enver ÖZDEMIR, and Prof. Tunçer BAYKAŞ for their valuable contributions during the progression of the dissertation as the thesis progress committee members. They have honored me by accepting to judge this work.

I would like to dedicate my dissertation work to my loving parents, my beloved husband, my dear sister and brothers, and my lovely niece.

I would like to thank all my friends, especially Amenallah, Asma, Farnoush, Wissem, and Azza for their support and encouragement.

Finally, I would like to thank everyone who is dear to me and I inadvertently omitted to mention.

July 2022

Olfa BEN YAHIA
(Telecommunication Engineer)

TABLE OF CONTENTS

Page

ABBREVIATIONS

6G : Sixth Generation
AWGN : Additive White Gaussian Noise
AF : Amplify and Forward
ASC : Average Secrecy Capacity
BER : Bit Error Rate
CDF : Cumulative Distribution Function
DF : Decode and Forward
EW : Exponentiated Weibull
FSO : Free-Space Optical
GS : Ground Station
GEO : Geostationary Earth Orbit
HAPS : High Altitude Platform Station
IM/DD : Intensity Modulated Direct Detection
LEO : Low Earth Orbit
LOS : Line-of-Sight
MEO : Meduim Earth Orbit
MC : Monte Carlo
NTN : Non-Terrestrial Networks
PDF : Probability Density Function
PPSC : Probability of Positive Secrecy Capacity
PLS : Physical Layer Security
PSD : Power Spectral Density
RF : Radio Frequency
SatCom : Satellite Communication
SOP : Secrecy Outage Probability
SC : Selection Combining
SNR : Signal-to-Noise Ratio
UAV : Unmanned Aerial Vehicle
VHetNets : Vertical Heterogeneous Network

SYMBOLS

$\boldsymbol{L}$: Propagation distance
$\boldsymbol{m}$: Nakagami-m fading severity parameter
$\boldsymbol{\lambda}$: Wavelength
$\boldsymbol{\gamma}$: Average SNR
$\bar{\boldsymbol{\gamma}}$: Average SNR
$\boldsymbol{\sigma_{\mathrm{I}}}^{2}$: Scintillation index
$\boldsymbol{h}$: Altitude
$\boldsymbol{h_{\mathrm{E}}}$: Height of the GS above mean sea level
$\boldsymbol{\sigma_{\mathrm{R}}}^{2}$: Rytov variance
$\boldsymbol{C_{\mathrm{n}}}^{2}$: Refractive index constant
$2\boldsymbol{b}$: Average power of the non-LOS component
$\boldsymbol{\Omega}$: Average power of the LOS component
$\boldsymbol{\sigma_{\mathrm{s}}}$: Jitter standard deviation
$\boldsymbol{B}$: Bandwidth
$\boldsymbol{T}$: Temperature
$\boldsymbol{P}$: Power
$\boldsymbol{N_0}$: Noise power
$\boldsymbol{V}$: Visibility
$(\cdot)_{\mathrm{k}}$: Pochhammer symbol
$\boldsymbol{r_0}$: Fried’s parameter
$\boldsymbol{\theta}$: Transmit divergence angle
$\boldsymbol{R_{\mathrm{s}}}$: Secrecy rate
$\boldsymbol{G_{\mathrm{p,q}}^{\mathrm{m,n}}}$: Meijer G-function
$\mathbf{erf}(\cdot)$: Error function

LIST OF TABLES

Page

LIST OF FIGURES

Page

PHYSICAL LAYER SECURITY PERFORMANCE OF SATELLITE NETWORKS

SUMMARY

A vision of a three-layer Vertical Heterogeneous Network (VHetNet) is being discussed in the state-of-the-art Sixth Generation (6G) network design. This concept is in line with the 3rd Generation Partnership Project (3GPP)'s non-terrestrial network (NTN) activities. A satellite (space) network, an aerial network, and a terrestrial network represent the three levels. The space layer includes geostationary Earth orbit (GEO) satellites and non-GEO satellites including low Earth orbit (LEO) and medium Earth orbit (MEO) satellites. This layer will provide orbit or space Internet services in applications including space travel as well as wireless coverage for unserved and underserved areas not served by terrestrial networks by densely deploying LEO, MEO, and GEO constellations. By intensively utilizing flying base stations (BS), including unmanned aerial vehicles (UAV), and floating BSs, such as high altitude platform systems (HAPS), the aerial layer would enable a more flexible and better quality of service for critical events or in inaccessible areas. For most human activities, the terrestrial layer will continue to be the primary method for delivering wireless coverage.

Satellite communication (SatCom) systems are typically radio frequency (RF)-based, with multiple frequency bands employed for different applications. However, RF channels suffer from spectrum congestion, license issues, interference with other frequency bands, and security threats. To address these issues, free-space optical (FSO) communication has lately been recommended for use in SatCom links because of its capacity to provide exceptionally large bandwidth, unlicensed spectrum, better security, low interference, ease of deployment, and other features over its RF counterpart. Nevertheless, similar to RF channels, FSO communication presents several drawbacks related to atmospheric effects, including atmospheric turbulence, scattering, and attenuation. Furthermore, FSO communication suffers from beam wander, beam divergence, and pointing issues. Different techniques have been proposed in the current literature to reduce these effects and enhance the overall performance including the incorporation of the RF link with the FSO to benefit from their complementary characteristics. This combination includes two possible architectures: mixed RF-FSO and hybrid RF/FSO communications. In mixed RF-FSO communication, a dual-hop network is considered, in which an RF channel is employed at one hop and an FSO channel is used at the other. For hybrid RF/FSO communication, RF and FSO channels are used in parallel. These combinations may reap all the advantages of both RF and FSO communications while minimizing weather-related issues. On the one hand, hybrid RF/FSO communication has received much attention in the recent literature. On the other hand, for satellite networks, there

is a substantial gap in hybrid RF/FSO communication. In addition, there are a few works about mixed RF-FSO networks in NTNs while sending the same information to a group of users on a particular multicast group address, known as multicast services.

Due to the broadcasting nature of the wireless channel, security is the most critical issue and challenging concern in NTNs. Unlike conventional methods, which often handle security at the application layer, physical layer security (PLS) guarantees information-theoretic security by extracting the variations in the physical properties of channels such that a degraded signal at an eavesdropper is always assured and therefore the original message can be hardly obtained regardless of how the signal is processed at the illegitimate receiver. PLS has been investigated as a good alternative to provide a solid form of security. Many studies have been conducted up to date to determine the fundamental performance limits of PLS under various wiretap channel models. It's worth noting that none of the available studies have investigated PLs in NTN systems.

This Ph.D. research has been motivated by these key challenges involving future networks. In this thesis, our work sheds light on the PLS performance in NTNs. Therefore, understanding the outage and error performance of the physical layer for future networks from the communication point of view is of great importance to studying the security aspect.

In the first part of the thesis, we study the hybrid RF/FSO transmission and mixed RF-FSO approaches for SatCom motivated by the complementary characteristics of RF and FSO communication. In the first proposed model, we assume a single-hop SatCom system where the satellite selects RF or FSO links based on weather conditions collected from sensors and employed for context awareness. We obtain the outage probability (OP) expressions by considering various weather situations to assess the performance of the proposed network. In addition, asymptotic analysis is carried out to determine the diversity order. We also consider the effects of non-zero boresight pointing errors and show how aperture averaging can significantly mitigate the effects of misalignment and atmospheric turbulence. The results reveal that the suggested technique outperforms dual-mode traditional hybrid RF/FSO communication in terms of OP while providing some power gain. Then, we present a novel downlink dual-hop SatCom model using an intermediate HAPS node. FSO communication is adopted between the LEO satellite and the HAPS node, whereas a hybrid FSO/RF transmission mechanism is considered between the HAPS node and the ground station (GS). The satellite chooses the HAPS node with the best signal-to-noise ratio in the initial phase of transmission. The signal is decoded and forwarded to the GS in the second phase by the designated HAPS. To examine the proposed system's performance, OP expressions for exponentiated Weibull and shadowed-Rician fading models are obtained, by considering atmospheric turbulence, scattering, stratospheric attenuation, path loss, and pointing errors. Aside from that, asymptotic analysis and diversity gain are obtained. The effect of the aperture averaging technique, wind speed, and temperature are also explored. Finally, the results show that using a HAPS node increases system performance and that the suggested model outperforms all other models currently in use.

Thereafter, we investigate the performance of a multiple-hop mixed RF-FSO communication-based decode-and-forward protocol for multicast networks. So far, delivering real-time applications to a large number of users at the same time has been seen as a promising technique to deal with high data traffic demands. Thus, we present two realistic use-cases. In the first model, we propose a mixed RF/FSO/RF communication strategy assisted by a HAPS node, in which a terrestrial node communicates with a cluster GSs via two HAPS systems. In the second model, we consider that due to substantial attenuation produced by wide propagation distances, we consider that line of sight (LOS) connectivity between the two HAPS systems is unavailable. As a result, we propose a mixed RF/FSO/FSO/RF communication system supported by an LEO satellite. Closed-form expressions of OP and bit error rate are obtained for the given scenarios. In addition, diversity gains are derived to show the asymptotic behavior of the proposed models. For both scenarios, ergodic capacity and energy efficiency (EE) are also presented. Finally, simulation results are presented in order to verify the theoretical derivations. The obtained results demonstrate that the satellite-assisted mixed RF/FSO/FSO/RF model outperforms the HAPS-assisted mixed RF/FSO/RF model in terms of OP, whereas the HAPS-assisted mixed RF/FSO/RF scenario achieves better EE.

From the security perspective, we propose different wiretap models and analyze the PLS performance. At first, for a HAPS-aided SatCom system, we study the secrecy performance of RF eavesdropping. In the proposed architecture, FSO communication is used between HAPS and the LEO satellite, while RF communication is used between HAPS and the GS as LOS communication cannot be established. Closed-form of secrecy outage probability (SOP) and probability of positive secrecy capacity (PPSC) expressions are derived to interpret the overall secrecy performance of the proposed approach. We also consider the impact of the pointing error and shadowing severity parameters. In what follows, we introduce optical eavesdropping in NTNs for different practical scenarios. In this context, we consider that a HAPS eavesdropper node is seeking to collect sensitive data from an LEO satellite, and a UAV eavesdropper is attempting to intercept confidential data from a HAPS node. We obtain closed-form SOP and PPSC expressions and validate them with Monte Carlo (MC) simulations to evaluate the overall performance of both scenarios. Secondly, a satellite eavesdropping strategy is presented, in which an attacker spacecraft trying to intercept optical communications established between an LEO satellite and a HAPS node. We assume satellite-to-HAPS (downlink) and HAPS-to-satellite (uplink) optical communications, in which the eavesdropper spacecraft can capture either the transmitted or received signal. The average secrecy capacity and SOP expressions are obtained and validated with MC simulations to quantify the secrecy performance. We also investigate secrecy throughput performance. Finally, according to our findings, turbulence-induced fading has a considerable impact on the secrecy performance of FSO communication.

UYDU AĞLARININ FİZİKSEL KATMAN GÜVENLIK BAŞARIMI

ÖZET

Altıncı nesil (sixth generation; 6G) ağ tasarımında üç katmanlı Dikey Heterojen Ağ (VHetNet) vizyonu üzerinde durulmaktadır. Bu konsept, 3rd Generation Partnership Project (3GPP) organizasyonun karasal olmayan ağ (non-terrestrial network; NTN) faaliyetleri ile uyumludur. Bu sistemde bulunan uydu (uzay) ağı, hava ağı ve karasal ağ, VHetNet'in üç katmanını temsil etmektedir. Uzay katmanı, alçak Dünya yörüngesi (low Earth orbit; LEO), orta Dünya yörüngesi (medium Earth orbit; MEO) uyduları dahil olmak üzere, yere göre durağan (sabit) Dünya yörüngesi (geostationary Earth orbit; GEO) uydularını içerir. Bu katman LEO, MEO ve GEO takım yıldızlarını yoğun bir şekilde dağıtarak hizmet verilmeyen ve yetersiz hizmet verilen alanlar için kablosuz haberleşme dahil farklı uygulamalarda yörünge veya İnternet hizmetleri sağlayabilecektir. Uydu katmanından farklı olarak hava katmanı insansız hava araçları (unmanned aerial vehicles; UAV'ler), yüksek irtifa platform sistemleri (HAPS) gibi yüzer modeller dahil olmak üzere uçan baz istasyonlarının (base stations; BSs) yoğun bir şekilde kullanılmasıyla daha esnek ve daha iyi hizmet kalitesi sağlayabilecektir. Bu modelde üçüncü katman olan karasal haberleşme katmanı kablosuz kapsama sağlamak için birincil yöntem olarak kullanılmaya devam edecektir.

Uydu iletişim (Satellite Communications; SatCom) sistemleri tipik olarak radyo frekansı (radio frequency; RF) tabanlıdır ve farklı uygulamalar için birden fazla frekans bandı kullanılır. Bununla birlikte, RF kanalları, spektrum tıkanıklığı, lisanslı bant, diğer frekans bantlarıyla etkileşim ve güvenlik tehditlerinden muzdariptir. Bu sorunları ele almak için, son derece geniş bant genişliği, lisanssız spektrum, daha iyi güvenlik, düşük parazit, dağıtım kolaylığı ve diğer özellikler sağlama kapasitesi nedeniyle, son zamanlarda SatCom bağlantılarında serbest alan optik (free-space optical; FSO) iletişiminin kullanılması önerilmiştir. RF muadili üzerinde. Bununla birlikte, RF kanallarına benzer şekilde, FSO iletişimi, atmosferik türbülans, saçılma ve zayıflama dahil olmak üzere atmosferik etkilerle ilgili bir takım dezavantajlar barındırmaktadır. Ayrıca, FSO iletişimi, ışın gezinmesi, ışın sapması ve işaret sorunlarından muzdariptir. Bu etkileri azaltmak ve tamamlayıcı özelliklerinden yararlanmak için FSO ile RF bağlantısının dahil edilmesi dahil olmak üzere genel performansı artırmak için mevcut literatürde farklı teknikler önerilmiştir. Bu kombinasyon iki olası mimariyi içerir: karma RF-FSO ve hibrit RF/FSO iletişimi. Karışık RF-FSO iletişiminde, bir atlamada bir RF kanalının ve diğerinde bir FSO kanalının kullanıldığı bir çift atlamalı ağ ele alınmıştır. Hibrit RF/FSO iletişimi için RF ve FSO kanalları paralel olarak kullanılmıştır. Bu kombinasyonlar, hava ile ilgili sorunları en aza indirirken hem RF hem de FSO iletişiminin tüm avantajlarından yararlanabilir. Bir yandan, hibrit RF/FSO iletişimi son literatürde büyük ilgi

görmüştür. Öte yandan, uydu ağları için hibrit RF/FSO iletişiminde önemli bir boşluk vardır. Ayrıca, NTN'lerde aynı bilgiyi belirli bir çok noktaya yayın grubu adresi üzerinden bir grup kullanıcıya gönderirken, çok noktaya yayın hizmetleri olarak bilinen karışık RF-FSO ağları hakkında birkaç çalışma bulunmaktadır.

Kablosuz kanalın yayın niteliğinden dolayı güvenlik, NTN'lerde en kritik konu ve zorlu bir problemdir. Genellikle uygulama katmanında güvenliği ele alan geleneksel yöntemlerden farklı olarak, fiziksel katman güvenliği (physical layer security; PLS), kanalların fiziksel özelliklerindeki varyasyonları çıkararak bilgi-teorik güvenliği garanti eder, böylece bir dinleyicideki bozulmuş bir sinyal her zaman garanti edilir ve dolayısıyla orijinal mesaj sağlanabilir. Sinyalin gayri meşru alıcıda nasıl işlendiğine bakılmaksızın zorlukla elde edilebilir. PLS, sağlam bir güvenlik biçimi sağlamak için iyi bir alternatif olarak araştırılmıştır. Çeşitli dinleme kanalı modelleri altında PLS'nin temel performans sınırlarını belirlemek için bugüne kadar birçok çalışma yapılmıştır. Fakat mevcut çalışmaların hiçbiri NTN sistemlerinde PLS kavramını araştırmamıştır.

Bu doktora tezinin temeli gelecekteki ağları içeren bu temel zorluklardır. Çalışmamız NTN'lerde PLS'nin fiziksel performansına ışık tutmayı amaçlamaktadır. Bu nedenle, gelecekteki ağlar için fiziksel katmanın kesinti ve hata performansını iletişim açısından anlamak, güvenlik seviyesini incelemek için önem taşımaktadır.

Tezin ilk bölümünde, RF ve FSO iletişiminin tamamlayıcı doğası tarafından motive edilen SatCom için hibrit RF/FSO iletimi ve karma RF-FSO yaklaşımları incelenmiştir. Önerilen ilk modelde, uydunun sensörlerden toplanan ve bağlam farkındalığı için kullanılan hava koşullarına dayalı olarak RF veya FSO bağlantılarını seçtiği tek atlamalı bir SatCom sistemi varsayılmıştır. Önerilen ağın performansını değerlendirmek için çeşitli hava durumlarını göz önünde bulundurarak kesinti olasılığı (outage probability; OP) ifadeleri elde edilmiştir. Ayrıca çeşitlilik sırasını belirlemek için asimptotik analiz yapılmıştır. Ayrıca sıfır olmayan ön görüş işaretleme hatalarının etkilerini de göz önünde bulundurularak ve açıklık ortalamasının yanlış hizalama ve atmosferik türbülansın etkilerini önemli ölçüde nasıl azaltabileceği gösterilmiştir. Sonuçlar, önerilen tekniğin, bir miktar güç kazancı sağlarken, OP açısından çift modlu geleneksel hibrit RF/FSO iletişiminden daha iyi performans gösterdiğini ortaya koymaktadır. Ardından, bir ara HAPS düğümü kullanan yeni bir aşağı bağlantı çift atlamalı SatCom modeli sunuyoruz. LEO uydusu ile HAPS düğümü arasında FSO iletişimi yaparken, HAPS düğümü ile yer istasyonu (ground station; GS) arasında bir hibrit FSO/RF iletim mekanizması ele alınmıştır. Uydu, iletişiminin ilk aşamasında en iyi sinyal-gürültü oranına (signal to noise ratio; SNR) sahip HAPS düğümünü seçilmektedir. Sinyalin kodu çözülür ve ikinci aşamada belirlenen HAPS tarafından GS'ye iletilir. Önerilen sistemin performansını incelemek için, atmosferik türbülans, saçılma, stratosferik zayıflama, yol kaybı ve işaret hataları dikkate alınarak üstel Weibull (EW) ve gölgeli-Rician sönüm modelleri için OP ifadeleri elde edilmiştir. Bunun dışında asimptotik analiz ve çeşitlilik kazancı bulunmuştur. Açıklık (aperture) ortalama alma tekniği, rüzgar hızı ve sıcaklığın etkisi de araştırılmıştır. Son olarak, sonuçlar bir HAPS düğümü kullanmanın sistem performansını artırdığını ve önerilen modelin şu anda kullanımda olan tüm diğer modellerden daha iyi performans gösterdiğini göstermektedir.

Bu çalışmayı takiben, çok noktaya yayın ağları için çok atlamalı karma RF-FSO iletişim tabanlı kod çözme ve iletme protokolünün performansı araştırılmıştır. Şimdiye kadar, gerçek zamanlı uygulamaları çok sayıda kullanıcıya aynı anda sunmak, yüksek veri trafiği taleplerinin üstesinden gelmek için umut verici bir teknik olarak tespit edilmiştir. Bu nedenle, iki gerçekçi kullanım durumu ele alınmıştır. İlk modelde, karasal bir GS'nin iki stratosferik HAPS sistemi aracılığıyla bir düğüm kümesi ile iletişim kurduğu bir HAPS düğümü tarafından desteklenen karma bir RF/FSO/RF iletişim stratejisi önerilmiştir. İkinci modelde, geniş yayılma mesafeleri tarafından üretilen önemli zayıflama nedeniyle, iki HAPS sistemi arasındaki görüş hattı (LOS) bağlantısının mevcut olmadığını varsayılmıştır. Sonuç olarak, bir LEO uydusu tarafından desteklenen karma bir RF/FSO/FSO/RF iletişim sistemi önerilmiştir. Verilen senaryolar için OP'nin kapalı form ifadeleri ve bit hata oranı elde edilmiştir. Ayrıca, önerilen modellerin asimptotik davranışını göstermek için çeşitlilik kazanımları ifadeleri verilmiştir. Her iki senaryo için de ergodik kapasite ve enerji verimliliği (enerji verimliliği; EE) sunulmaktadır. Son olarak, teorik türevleri doğrulamak için simülasyon sonuçları verilmiştir. Elde edilen sonuçlar, uydu destekli karma RF/FSO/FSO/RF modelinin OP açısından HAPS destekli karma RF/FSO/RF modelinden daha iyi performans gösterdiğini, HAPS destekli karma RF/FSO/RF senaryosunun daha yüksek EE değerleri elde ettiğini doğrulamaktadır.

Güvenlik açısından farklı dinleme modelleri önerilmiş ve PLS performansının analizi sunulmuştur. Öncelikle, HAPS destekli bir SatCom sistemi için, RF gizli dinlemenin gizlilik performansı incelenmiştir. Önerilen mimaride HAPS ile LEO uydusu arasında FSO iletişimi kullanılırken, LOS iletişimi kurulamadığı için HAPS ile GS arasında RF iletişimi kullanılmaktadır. Kapalı form gizlilik kesinti olasılığı (secrecy outage probability; SOP) ve pozitif gizlilik kapasitesi olasılığı (probability of positive secrecy capacity; PPSC) ifadeleri, önerilen yaklaşımın genel gizlilik performansını yorumlamak için türetilmiştir. Ayrıca işaretleme hatası ve gölgeleme şiddeti parametrelerinin etkisi de dikkate alınmıştır. Aşağıda, farklı pratik senaryolar için NTN'lerde optik gizli dinlemeyi problemi ele alınmıştır. Bu bağlamda, bir HAPS düğümünün bir LEO uydusundan hassas verileri toplamaya çalıştığı ve bir İHA dinleyicisinin HAPS düğümünden gelen gizli verileri ele geçirmeye çalıştığı varsayılmıştır. Her iki senaryonun genel performansını değerlendirmek için kapalı form SOP ve PPSC ifadeleri elde edilmiştir ve ifadeler Monte Carlo (MC) simülasyonları ile doğrulanmıştır. İkinci olarak, bir saldırgan uzay aracının bir LEO uydusu ve bir HAPS düğümü arasında kurulan optik iletişimi engellediği bir uydu dinleme stratejisi sunulmaktadır. Uydudan HAPS'a (downlink) ve HAPS'tan uyduya (uplink) optik iletişimleri varsayılmıştır, burada yetkisiz kulak misafiri uzay aracı iletilen veya alınan sinyali yakalayabilir. Ortalama gizlilik kapasitesi ve SOP ifadeleri, gizlilik performansını ölçmek için MC simülasyonları ile elde edilmiş ve doğrulanmıştır. Ayrıca, gizlilik aktarım hızı performansı da araştırılmıştır. Son olarak, bulgularımıza göre, türbülansa bağlı sönümleme, FSO iletişiminin gizlilik performansı üzerinde önemli bir etkiye sahiptir.

1. INTRODUCTION

This thesis mainly focuses on studying and investigating the channel characterization of the next-generation wireless networks from two aspects. First, we propose novel architectures for future networks while studying the physical layer performance from a communication perspective and propose some solutions to improve communication. Thereafter, we evaluate the physical layer performance from a security aspect. In particular, we introduce the physical layer security (PLS) for optical communication in non-terrestrial networks (NTN).

In this chapter, we introduce the background and motivation for the development of network architecture through the integration of three-dimensional layers. Then, we describe the motivations of this thesis. Furthermore, we present the elements of the new architecture, channel impairments, and mitigation techniques. Finally, the contributions alongside the outline of this thesis are presented.

1.1 Research Motivation and Background

Sixth Generation (6G) networks are expected to provide performance superior to the Fifth Generation (5G) and fulfill developing services and applications, making them a crucial enabler for the intelligent information society of 2030. The primary enabler for the information society of 2020 is 5G wireless networks. The 3rd Generation Partnership Project (3GPP) is continuing to support 5G development in a big way. Meanwhile, to meet the requirements for the smart data society of 2030, research on 6G wireless networks has been introduced to the agenda. Near-instant and unrestricted broad wireless connectivity will enable the smart data society of the 2030s to be fully digitized, worldwide data-driven, and intelligence-based. 6G will be fundamental to accomplishing this blueprint; it will connect everything, enable full coverage, and combine all features, including communication, sensing, caching, computation, control, location, radar, navigation, and imaging, to provide full-vertical applications. As a result, a multi-dimensional network integrating non-terrestrial and terrestrial networks is required to serve a variety of applications, such as aerial flight, maritime voyages, and land vehicles.

The development of NTN systems as an effective solution to complement terrestrial networks in providing services over uncovered or under-served geographical areas is driven by the evolution of telecommunication technologies, the ever-increasing demand for new services, and the rapid evolution of smart devices [1]. An NTN, as defined by the 3GPP in [2], is a network in which spaceborne (i.e., geostationary Earth orbit (GEO), medium Earth orbit (MEO), and low Earth orbit (LEO)) or airborne (i.e., unmanned aircraft system (UAS) and high altitude platform station (HAPS)) vehicles function as relay nodes or base stations, distinguishing transparent and regenerative satellite systems. The potential of NTNs to provide wide-area connectivity by delivering connections across regions that are costly or hard to serve with terrestrial networks (i.e., rural areas, vessels, airplanes) is its distinguishing feature. As a result, the NTN is a coverage expansion for the terrestrial network in a global market where customer requirements are rapidly changing. Furthermore, NTN guarantees scalability, service continuity, and availability resulting in a revolution in the existing cellular communications infrastructure. Therefore, the initial inspiration for this research derives from an industrial and academic interest in NTN systems throughout the last decade.

In particular, LEO satellites and HAPS systems are expected to be the key enablers of next-generation wireless networks. LEO satellites, which are one of the main components of the space network layer and orbiting at altitudes of less than 2,000 km, have attracted broad interest due to their potential to provide low round trip delay and a high data rate. In this regard, they become a potent enabler for real-time traffic such as voice and video for global coverage, especially in remote areas, where wired communication is challenging or cannot be employed.

Aerial networks can be divided into three groups; low altitude platform stations, unmanned aerial vehicles (UAV), and HAPS systems [3]. According to the definition of the International Telecommunication Union (ITU), a HAPS system is a fixed object at an altitude of 20 to 50 km [4]. However, the majority of recent deployments focused on an altitude of 18 to 20 km [3]. In particular, HAPS systems that are positioned in the stratosphere can combine the characteristics of the terrestrial network (low cost and latency) and of satellites (wide coverage area) [5]. In addition, HAPS systems are quasi-stationary aerial vehicles that suffer less from atmospheric turbulence as they are positioned above cloud formations [6]. However, HAPS systems are subject to stratospheric attenuation, which can be caused by sulfuric acid ingredients due to volcanic activity, gases, and polar clouds [7]. Alongside the HAPS systems, the UAV platforms employed near the ground level, play an important role by providing a low-cost solution for temporary wireless delivery services to remote areas that cannot be reached by satellites or HAPS systems [8].

The current architecture of satellite communication (SatCom) relies on the microwave radio frequency (RF) band for most of the applications [9]. However, RF communication suffers from limited capacity, congested spectrum, low bandwidth, and regulatory restrictions. Also, RF links are vulnerable to interception or jamming, which arises security problems. In this context, to successfully fulfill the high data rate requirements, free-space optical (FSO) communication links are considered a key component for NTN. FSO communication ensures high data rate transmission with a low probability of interception [10, 11] and it offers line-of-sight (LOS) connectivity over an unlicensed spectrum [12]. Despite their unique features, FSO links are prone to significant variations in both phase and intensity of the received signal due to fluctuations in the index of refraction caused by variations in temperature and pressure mostly for long-range communications [13]. Furthermore, FSO communication is weather-dependent and highly affected by turbulence-induced fading and attenuation. More precisely, FSO links may be significantly degraded by fog or snow, whereas attenuation due to rain has fewer impacts [14]. In addition, optical SatCom suffers from beam scintillation and beam wander effects, which are mainly caused by large-scale inhomogeneities in the atmosphere. Beam wander can be a significant factor in the uplink communication, as the turbulent eddies are significantly larger than the beam size, which leads to beam displacement and link failure [15]. However, it can be negligible for downlink communication. Also, acquisition and pointing are challenging in FSO SatCom, which are mainly caused by device vibration, platform jitter, or any type of stress in electronic or mechanical equipment. Thus, to avoid link failure, a LOS connection should be maintained between the transmitter and receiver [15].

It has been shown that shadowed-Rician fading fits very well to model the RF channels in SatCom. Shadowed-Rician was first proposed in 2003 by [16]. It finds potential applications in different frequency bands. In addition, the amplitude of the LOS that follows the Nakagami fading is assumed to be random due to LOS path obstructions by buildings, trees, and mountains, which makes it more realistic. The major advantage of this model is that it leads to closed-form and mathematically-tractable expressions [16].

Performance analyses of FSO communication have been reported in the literature using Log-normal, Gamma-Gamma, and Malága fading channels. Empirical studies, for their part, have proven that the exponentiated Weibull (EW) fading can be the best fit for different aperture sizes in all weather conditions, especially when aperture averaging is used [17]. The scintillation is spatially averaged over the aperture in the aperture averaging technique to mitigate the impacts of turbulence and improve the overall performance [18, 19]. Like aperture averaging, spatial diversity can be established between satellites and HAPS systems to provide reliable communication and mitigate the impact of atmospheric turbulence [19]. Furthermore, the optical beam is limited to masking effects over large distances and LOS connectivity can not be established between the satellites and the ground users due to shadowing and obstacles. Thus, in SatCom, cooperative relaying in which a HAPS is used as an intermediate relay node can be considered an effective solution to mitigate the channel impairments and to reap the benefits offered by both communication systems including higher coverage and lower delay. Another way of reducing the effects of atmospheric turbulence and enhancing the performance of HAPS systems is to use RF and FSO communications together to benefit from the complementary characteristics [20]. This combination consists of two possible configurations. The first one is the so-called mixed RF-FSO model, in which RF communication is used at one hop and FSO communication at the other in a dual-hop configuration [21, 22]. The second model is the hybrid RF/FSO communication, where the RF channel is incorporated in parallel with the FSO channel. Such hybrid RF/FSO communication can reap all the advantages of RF and FSO communication while minimizing adverse weather-dependent effects. FSO and RF links are sensitive to non-overlapping conditions and are considered to have a complementary nature [14]. So far, different approaches have been proposed in this context by considering soft-switching or hard-switching techniques [23]. In hard-switching, which is more practical, only one link might be active at a time. In this method, the FSO link is active initially, and the RF link acts as a backup when the FSO becomes unavailable. In the case of soft-switching, there is a simultaneous transmission on both links depending on their availability. Hybrid RF/FSO communication has been studied from different perspectives and in various scenarios in [24–26]. The authors in [27] and [28] proposed a parallel transmission of the same information through RF and FSO links, by considering different diversity-combining techniques. In the literature, different diversity combining techniques including selection combining (SC) and maximal ratio combining (MRC) are used to maximize the overall SNR, hence they can reduce the adverse effects of turbulence [29]. In the current literature, hybrid RF/FSO communication has been well investigated. However, these studies are mostly limited to horizontal terrestrial transmission, in which the distance is about 1-3 km. However, only a few papers have investigated hybrid RF/FSO communication for satellite systems [30,31] and none of them have studied the practical effects of weather conditions. The use of HAPS systems in hybrid RF/FSO communication has also been studied in the literature. In [32], the authors proposed a hybrid scheme for downlink SatCom using a HAPS node as an intermediate terminal between an LEO satellite and a ground station (GS). In doing so, they derived the average symbol error probability (ASEP) while considering DF relaying and a backup RF channel in the second hop. More recently, in [33], the authors compared a single-hop hybrid RF/FSO SatCom with a dual-hop hybrid RF/FSO communication by using a HAPS node for the uplink. Their results showed that the hybrid RF/FSO outperforms the FSO systems and that the use of the HAPS node improves the performance of uplink SatCom. In addition, the performance analysis for downlink SatCom systems has been extensively carried out for single-hop FSO or RF communication and dual-hop mixed RF-FSO communication. Therefore, there is a significant gap in hybrid RF/FSO communication for satellite networks.

With the increase in the proliferation of streaming media, video conference, IP-TV, and many other applications of broadcast communication, it is expected that the spectral efficiency of wireless communications can be enhanced by serving a group of users simultaneously [34]. Therefore, multicasting is well suitable for these services as it exploits the resources of the network efficiently. According to the ITU recommendations, a multicast group is defined as a set of nodes that have specified their intention to receive packets on a particular multicast group address [35]. Several studies have been conducted to investigate multicasting protocols. In the literature, the performance analysis of multicast services was mainly limited to terrestrial communication [36–38]. In SatCom, most of the recent works have considered direct satellite to ground downlink unicast instead of multicast transmission. However, when compared to unicasting, this mode of transmission improves the efficiency of the use of radio resources and is commonly utilized to send the same information to a group of users in any network [39].

One major challenge in non-terrestrial networks is to guarantee a secure exchange of information. Typically, communication security is ensured by employing encryption techniques that rely on the open systems interconnection (OSI) model's upper layers. These methods can be divided into two categories based on whether the shared key is public or private. Complex methods and computer capacity are required to encrypt plain text and it is anticipated that eavesdroppers will be unable to expose the secret key and decrypt the message. These protocols, however, are no longer appropriate for applications that demand a high level of security due to the expansion of computers in computing capacity and methods to disrupt encryption techniques. Lately, we are seeing growing attention on physical layer security (PLS), which has been shown to effectively increase information security. Unlike cryptographic algorithms that ignore the randomness of wireless channels, PLS is achieved by exploring signal and channel characteristics such as difference and reciprocity, allowing for secure transmission between users without regard for illegitimate users' computation power. Information-theoretic security is commonly referred to as PLS. Shannon was the first to introduce information-theoretic security in cipher systems in 1949 by avoiding the use of computational limitations [40]. Later, Wyner [41] proposed a model called "wiretap channel" in which he considered that the main channel should be superior to the eavesdropper to satisfy perfect secrecy.

In the current literature, most of the existing studies focus on RF eavesdropping, in which the eavesdropper tackles the information from the RF communication. Lately, PLS has been introduced for FSO communication. In FSO communication, the eavesdropper should be positioned very close to the communicating peers, so that it can capture the beam that is reflected by the aerosols or gases in the atmosphere. However, if the eavesdropper blocks the laser beam while capturing information, the receiver can notice the leakage of power and thus stop the communication for security issues. An alternative scenario can occur when misalignment arises between the communicating peers due to severe pointing errors or diffraction. In such a case, the beam spreads out and the eavesdropper may receive the refracted beam [42]. Even though optical communication can be intercepted, little work has been done on PLS performance. Y. Ai *et al.* [43] discussed the PLS for three different realistic scenarios by assuming different positions of the eavesdropper. Atmospheric condition imposes less impact on the secrecy performance when the eavesdropper is placed near the transmitter. In [44], the cases in which the eavesdropper is placed in proximity to the receiver or proximity to the transmitter are investigated. It was observed that when the eavesdropper is close to the legitimate transmitter, it can easily intercept the communication by taking advantage of the larger attenuation affecting the signal when propagating through the FSO channel. In [45], the closed-form expressions of average secrecy capacity (ASC), secrecy outage probability (SOP), and strictly positive secrecy capacity (SPSC) over Málaga atmospheric turbulence channels in the presence of pointing errors are obtained. The authors in [46] studied the PLS performance of FSO communication in terms of a recent proposed metric named effective secrecy throughput. Furthermore, under generalized misalignments and atmospheric turbulence conditions, the authors in [47] studied the ASC for the log-normal fading model. Recently, the authors in [48] proposed artificial noise injection to improve the secrecy performance of FSO channels over Gamma-Gamma fading in the presence of pointing errors. The latest studies witness a growing interest in security issues for FSO communication systems. However, these works are limited to optical terrestrial communications. Thus, there is a significant gap in the current research of PLS for FSO in NTNs. Also, the threat introduced by an eavesdropping spacecraft has not been studied in the literature.

1.2 Contribution and Outline

1.2.1 Contribution

In this thesis, the overall aim is to provide a comprehensive study of the physical layer of the next-generation wireless networks from two different perspectives: communication and security. The thesis' organization flow and primary contributions, which give innovations to the literature and research area, are detailed here, with an emphasis on the thesis' originality from various perspectives.

1.2.2 Outline

In chapter 2, different from the current literature, we provide a reliable communication strategy for the downlink SatCom by using hybrid RF/FSO communication considering soft-switching technique according to weather characteristics. More precisely, the proposed strategy enables us to switch between FSO and RF links based on the weather situation which can be obtained from the sensors on the satellite and used for context-awareness. In this concept, we assume that the satellite detectors can scan the weather conditions of the atmosphere continuously within the LOS region. Then, based on the extracted information, the satellite determines to activate the most favorable channel immediately. By doing so, the overall performance of the presented strategy improves as the LEO satellite is aware of the weather conditions. Furthermore, we study the effect of atmospheric turbulence, scattering, and non-zero boresight pointing errors, and consider the impact of shadowing on communication performance. We also highlight the impact of aperture averaging to mitigate the effect of turbulence-induced fading and the misalignment of the transmitting beam to achieve better directivity. Outage probability (OP) expressions are derived for the proposed configuration. In addition, an asymptotic performance analysis is conducted and the achievable diversity gain is obtained. Finally, we compare our proposed strategy with the conventional dual-mode RF/FSO soft-switching communication and provide interesting design guidelines.

The study described in this chapter has been published in the following journal paper.

J1: O. Ben Yahia, E. Erdogan, G. Karabulut Kurt, I. Altunbas, and H. Yanikomeroglu, "A weather-dependent hybrid RF/FSO satellite communication for improved power efficiency", IEEE Wireless Communications Letters, vol. 11, no. 3, pp. 573–577, 2022.

Chapter 3 introduces a novel model for downlink SatCom where the HAPS node with the best channel characteristics is selected. To the best of the authors' knowledge, the HAPS selection for downlink SatCom has not yet been studied in the literature, and its potential to improve the system performance is still unknown. To guarantee reliable communication, we consider FSO communication between the satellite and HAPS systems, and hybrid RF/FSO communication is adopted between the HAPS systems and GS. Furthermore, for different weather conditions, we consider the effects of atmospheric turbulence, attenuation resulting from scattering, path loss, and pointing errors to provide realistic modeling for the proposed setup. In addition, we investigate the effects of temperature and consider an aperture averaging technique to reduce fluctuations due to turbulence-induced fading and to mitigate the performance degrading effect of pointing errors. Moreover, we derive the OP expressions and validate them with Monte Carlo (MC) simulations. Furthermore, asymptotic analysis is carried out to understand the behavior of the proposed system at a high signal-to-noise ratio (SNR). We also provide important design guidelines.

The study presented in this chapter has been published in the following journal paper.

J2: O. Ben Yahia, E. Erdogan, G. Karabulut Kurt, I. Altunbas, and H. Yanikomeroglu, "HAPS selection for hybrid RF/FSO satellite networks", IEEE Transactions on Aerospace and Electronic Systems (early access), pp. 1–13, 2022.

Chapter 4 discusses the physical layer performance of multicast services for future networks from a communication aspect. To the best of the authors' knowledge, multicast services in satellite or aerial networks are studied from a network layer perspective. However, the performance analysis of HAPS-aided or satellite-aided-HAPS for multicast services has not been investigated in the literature from a physical layer perspective. Thus, different from the current literature, in this work, we investigate the physical layer performance of multicast services for HAPS-assisted mixed RF-FSO networks. In particular, two use-cases have been proposed for multicast downlink communication. In the first one, we consider a ground transmitter communicating with a multicast group through the use of two intermediate HAPS systems. In the second use case, the communication is conducted through two HAPS systems connected with an LEO satellite. For the proposed schemes, we investigate the effect of beam wander-induced pointing error for the uplink, the effect of aperture averaging technique and pointing error for the downlink, and the effect of shadowing severity for RF communication. We derive closed-form OP and bit error rate (BER) expressions for both scenarios by considering stratospheric attenuation, stratospheric turbulence induced-fading for FSO communication, and shadowing for RF communication. Moreover, to gain further insights and to reveal the asymptotic behavior of the proposed systems, high SNR analysis is conducted and diversity gain is obtained. We also obtain upper-bounded ergodic capacity expressions and energy efficiency for both scenarios.

The study explained in this chapter has been prepared in the following paper.

J3: O. Ben Yahia, E. Erdogan, G. Karabulut Kurt, “HAPS-assisted Hybrid RF-FSO Multicast Communications: Error and Outage Analysis”, IEEE Transactions on Aerospace and Electronic Systems (early access), pp. 1–13, 2022.

Chapter 5 investigates the RF eavesdropping for HAPS-aided FSO-RF SatCom, where the illegitimate user is located on the ground level. We evaluate the security performance of HAPS-aided downlink FSO-RF SatCom. Furthermore, we emphasize the use of the HAPS to mitigate the effect of weather conditions on the FSO link. We elaborate on the effect of the severity of fading, the severity of scintillation, and the zenith angle. Furthermore, we also consider the effect of pointing errors and the heterodyne detection (HD) technique in the proposed scheme. We derive the closed-form of the probability of positive secrecy capacity (PPSC) and SOP expressions by considering RF eavesdropping.

The study presented in this chapter has been published in the following paper.

W1: O. Ben Yahia, E. Erdogan, and G. Karabulut Kurt, “On the use of HAPS to increase secrecy performance in satellite networks”, in IEEE International Conference on Communications Workshops (ICC Workshops), 2021, pp. 1–6.

Chapter 6 introduces a novel FSO eavesdropping framework for NTNs by considering both satellite-to-HAPS and HAPS-to-UAV communications. We quantify the overall performance by considering the effects of aperture averaging, zenith angle, atmospheric, and stratospheric attenuation where closed-form SOP and PPSC expressions are obtained.

The study presented in this chapter has been published in the following paper.

W2: O. Ben Yahia, E. Erdogan, G. Karabulut Kurt, I. Altunbas, and H. Yanikomeroglu, "Physical layer security framework for optical non-terrestrial networks (invited paper)", in International Conference on Telecommunications (ICT), 2021, pp. 162–166.

Chapter 7 presents a framework for the security of LEO constellations by introducing the concept of eavesdropping by a spacecraft. Specifically, we investigate the secrecy performance of optical communication under two realistic scenarios. In the first one, we assume a downlink communication between an LEO satellite and a HAPS node. In the second one, we consider an uplink communication from the HAPS node to the satellite. In both cases, we assume that an external observer (attacker spacecraft), which intends to intercept the communication, is located very close to the satellite, within the convergence area of its optical beam. We study the impact of the amount of the leaked power and the impact of the stratospheric turbulence on the secrecy performance. We obtain new closed-form expressions for SOP and ASC for EW fading while considering the amount of power captured by the eavesdropping spacecraft. In addition, secrecy throughput (ST) analysis is provided.

The study presented in this chapter has been prepared in the following paper.

J4: O. Ben Yahia, E. Erdogan, G. Karabulut Kurt, I. Altunbas, and H. Yanikomeroglu, "Optical Satellite Eavesdropping", IEEE Transactions on Vehicular Technology (early access), pp. 1–6, 2022.

Chapter 8 sums up the thesis by presenting the main findings and summarizing the chapters' contributions. We also provide future work directions.

It should be noted that the notation of each chapter is self-contained.

1.3 List of Published, Submitted, and in Preparation Manuscripts

1. **O. Ben Yahia**, E. Erdogan, G. Karabulut Kurt, I. Altunbas, and H. Yanikomeroglu, “Secure RF/FSO Communications Towards the 6G Era”, in *IEEE Tech Focus on Security and Privacy*, accepted.
2. M. Y. Abdelsadek, A. U. Chaudhry, T. Darwish, E. Erdogan, G. Karabulut Kurt, P. G. Madoery, **O. Ben Yahia**, and H. Yanikomeroglu, “Future Space Networks: Toward the Next Giant Leap for Humankind”, in *IEEE Transaction On Communications*, under review.

2. A WEATHER-DEPENDENT HYBRID RF/FSO SATELLITE COMMUNICATION FOR IMPROVED POWER EFFICIENCY

In the near future, LEO satellites, which can cross over the continents within a few minutes, are expected to play a key role in the next generation networks, due to their intrinsic features [49]. In addition, in SatCom systems, FSO or RF channels are used depending on the communication environment. As mentioned in the previous chapter, to investigate the PLS performance of satellite networks, we first need to study the characteristics of RF and FSO channels and understand their performance from a physical layer perspective. Furthermore, we need to understand the parameters that affect a downlink SatCom communication. Therefore, motivated by the complementary nature of RF and FSO communication, in this chapter, we propose a hybrid RF/FSO transmission strategy for a single-hop SatCom system, where an LEO satellite selects RF or FSO links depending on the weather conditions obtained from sensors and used for context-awareness.

As mentioned before, this work has been published in the following journal paper:

O. Ben Yahia, E. Erdogan, G. Karabulut Kurt, I. Altunbas, and H. Yanikomeroglu, "A weather-dependent hybrid RF/FSO satellite communication for improved power efficiency", IEEE Wireless Communications Letters, vol. 11, no. 3, pp. 573–577, 2022.

The chapter is organized as follows: Signals and system models are presented in section 2.1. In Section 2.2, our proposed scheme is presented and the expressions of OP are derived along with the diversity gain. Numerical results are outlined and discussed followed by some design guidelines in Section 2.3 and Section 2.4 concludes this work.

2.1 Signals and System Model

In this work, we consider a downlink SatCom, where an LEO satellite aims to communicate with a GS where both RF and FSO channels are used in parallel to

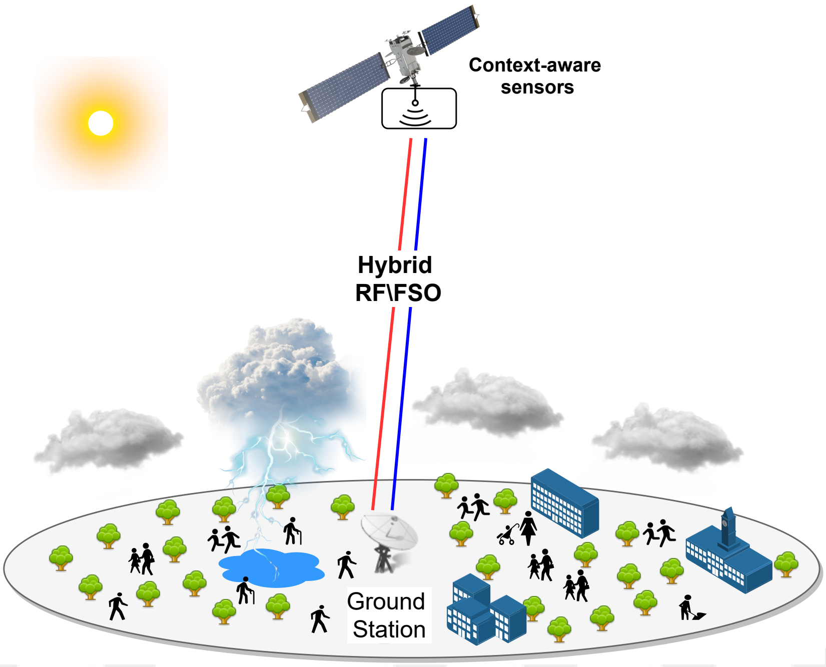

Figure 2.1 : Illustration of weather-dependent hybrid RF/FSO SatCom.

transmit identical rate information, based on their availability as shown in Figure 2.1. More precisely, the LEO satellite, which is deployed with context-aware sensors, can detect the weather conditions on the ground continuously and adapt to the situation immediately. Thereafter, it uses the most favorable channel or both channels at the same time to transmit the information and accordingly adapts the transmission power. In the state where both channels are activated, the received signals are combined at the GS using SC technique to maximize the overall performance. Although the MRC technique provides better performance, we consider SC due to its practical relevance. For the proposed setup, FSO communication is modeled with EW fading, whereas shadowed-Rician distribution is used to model the RF communication. Table 2.1 summarizes the proposed scheme. The signal models for both channels are given in the following subsections.

2.1.1 FSO channel

The received optical signal[1] detected by the photodetector of the GS is modeled as $y = \sqrt{\zeta P_1} I x + n$ where $0 \leq \zeta \leq 1$ denotes the optical-to-electrical conversion coefficient, P_1 is the transmit power of the satellite through the FSO link, I indicates the irradiance

---

[1] For FSO transmission, we consider intensity-modulated direct detection (IM/DD) as it is largely used in practical urban networks owing to its simplicity and low-cost [50].

Table 2.1 : Proposed scheme.

State (k)	**Description**	**Observation**	**Transmission strategy**
0	Thin Cloud	Both FSO and RF channels exhibit a higher performance	Dual (SC)
1	Rain	Only the FSO communication is favorable with full power	FSO
2	Fog	Only the RF channel is available with full power	RF

of the channel where $I = I^t I^p I^a$, where I^t indicates the atmospheric turbulence-induced fading [19], I^p is the pointing error, and I^a defines the atmospheric attenuation that includes Mie scattering and geometrical scattering [19, eqn. (10)]. In clear weather conditions, the geometrical scattering is mainly caused by thin cirrus clouds, and the attenuation coefficient is expressed as given in [19, eqn. (8)], whereas under rainy conditions, the extinction coefficient can be expressed as $\Theta = 1.067\mathscr{R}^{0.67}$ [23], where $\mathscr{R}$ is the rainfall rate in (mm/h), x is the transmitted signal and n is the zero-mean additive white Gaussian noise (AWGN) with one-sided power spectral density (PSD) N_0. Thus, the instantaneous SNR at GS can be expressed as

$$\gamma_{FSO} = \frac{\zeta P_1 I^2}{N_0} = \overline{\gamma}_{FSO} I^2, \tag{2.1}$$

where $\overline{\gamma}_{FSO} = \frac{\zeta P_1}{N_0}$ is the average SNR of FSO channel and $\mathbb{E}[I^2] = 1$. In FSO communication, we consider the combined effects of atmospheric turbulence, non-zero boresight error and jitter. Thereby, the cumulative distribution function (CDF) of I is given as [51]

$$\begin{aligned} F_I(I) = {} & \frac{\alpha g^2}{\beta} \exp\Big(-\frac{s^2}{2\sigma_s^2}\Big) \sum_{i=0}^{\infty} \frac{(-1)^i \Gamma(\alpha)}{(1+i)!\Gamma(\alpha-i)} \\ & \times \sum_{j=0}^{\infty} \frac{(\frac{s^2 g^2}{2\sigma_s^2 \beta})^j}{j!} G_{j+2,j+3}^{j+2,1}\left(T_3(i) \middle| \begin{array}{c} 1, \overbrace{T_1+1, \ldots, T_1+1}^{(j+1)\text{terms}} \\ 1, \underbrace{T_1, \ldots, T_1}_{(j+1)\text{terms}}, 0 \end{array} \right), \end{aligned} \tag{2.2}$$

where α, β denote the shape parameters [17], $g = w_{eq}/(2\sigma_s)$ is the ratio between the equivalent beam which is given as $w_{eq}^2 = w_z^2 \sqrt{\pi} \mathrm{erf}(v)/(2ve^{-v^2})$ and the jitter standard deviation σ_s, η is the scale parameter [17], s presents the boresight value, $T_3(i) = (1+i)\left[\frac{I}{(\eta A_0)}\right]^{\beta}$ with $A_0 = [\mathrm{erf}(v)]^2$ is the gathered optical power for zero difference between the optical spot center and the detector center, and $\mathrm{erf}(\cdot)$ is the error function. Moreover, $v = \sqrt{\pi/2a}/w_z$ is the ratio of the aperture radius a and the beam-width w_z at the distance z with $w_z = \theta z$, where θ denotes the transmit divergence angle, and $T_1 = g^2/\beta$ [52]. Finally, $\Gamma(\cdot)$ is the Gamma function and $G_{p,q}^{m,n}\left(x \left| \begin{matrix} a_1,\ldots,a_p \\ b_1,\ldots,b_q \end{matrix} \right.\right)$ is the Meijer G-function [53]. In the absence of pointing error, the CDF of I is given as [19, eqn. (12)]. The parameters α, β, and η depend on the zenith angle of the satellite ξ, the wind speed level v_g expressed in m/s, the wavelength λ, the refractive index C_n^2, and the aperture diameter D_G [19].

2.1.2 RF channel

Let x denote the transmitted signal with power P_2 from the satellite to the GS through the RF link. The received signal at GS can be expressed as $y = \sqrt{P_2 h_l} h x + n$. h denotes the channel response of the path from the satellite to the GS that follows the shadowed-Rician fading [54], h_l is the path loss modeled as $h_l[dB] = G_T + G_R - 20\log_{10}\left(\frac{4\pi L}{f}\right) - \omega_{oxy}L - \omega_{rain}L$ [23], where G_T and G_R are the gains of the transmitting and receiving antennas respectively, f is the RF wavelength, L is the propagation distance in km, ω_{oxy}, ω_{rain} are the attenuation coefficients due to the oxygen and rain scattering respectively [55], and n is the AWGN with one-sided power spectral density N_0. Therefore, the instantaneous SNR at the GS can be written as

$$\gamma_{RF} = \frac{P_2 h_l |h|^2}{N_0} = \overline{\gamma}_{RF}|h|^2, \tag{2.3}$$

where $\overline{\gamma}_{RF} = \frac{P_2 h_l}{N_0}$ indicates the average SNR of the RF link with $\mathbb{E}[|h|^2] = 1$.

The main attenuation factor for the RF communication is the rain, where it rises linearly with the rainfall rate. Thus, the rain attenuation coefficient ω_{rain} (dB/km) can be expressed based on the rain rate $\mathscr{R}$ as $\omega_{rain} = k_r \mathscr{R}^{\rho}$, where k_r and ρ depend on the channel frequency f [56]. The CDF of the squared envelope of shadowed-Rician channel $|h|^2$ can be expressed as [57]

$$F_{|h|^2}(h) = \mu h \Phi_2\Big(1-m, m; 2; -\nu h, -\vartheta h\Big), \tag{2.4}$$

where $\mu = \frac{1}{2b}\left(\frac{2bm}{2bm+\Omega}\right)^m$, with m representing the Nakagami-m severity parameter of the corresponding link and Ω and $2b$ are the average power of the LOS component and multi-path component, $\nu = \frac{1}{2b}$, and $\vartheta = \frac{m}{2bm+\Omega}$. Finally, Φ_2 defines the bivariate confluent hypergeometric function given in [58, Section 9.26].

2.2 Performance Analysis

In this work, we propose a new scheme in which an LEO satellite adapts its power and switches between FSO and RF links based on the weather situation obtained from the satellite sensors as shown in Table 2.1. To this end, the overall system performance can be improved. Considering P_t is the total transmit power of the satellite, we allocate equal transmit power on both RF and FSO links where $P_1 = P_2 = P_t/2$ when both links are used as given in State-0. However, power allocation scheme can be adopted here to adjust the power levels if needed. For this state, we assume clear weather conditions (thin cloud), where both RF and FSO channels provide higher performance. For State-1, we consider the presence of heavy rain, which strongly affects the RF transmission and has fewer effects on FSO transmission. Thus, the RF link is not suitable for transmission, and the communication is conducted through the FSO link using the total transmit power is $P_1 = P_t$. Likewise, in State-2, we consider that FSO is totally unavailable due to heavy fog and the RF transmission is activated using the total transmit power $P_2 = P_t$. Furthermore, we denote the probability of occurrence of each state by p_k for $k \in \{0,1,2\}$.

2.2.1 Outage probability

To study the performance of our proposed scheme, we derive the OP expressions. The OP can be defined as the probability that the instantaneous SNR γ falls below a predefined threshold γ_{th} and it can be written for the k-th state as $P_{\text{out},k}(\gamma_{th}) = \Pr[\gamma \leq \gamma_{th}]$ for $k \in \{0,1,2\}$. For State-0, where both RF and FSO links might be active simultaneously, the GS uses SC. Thus, the final expression of OP for State-0 in the absence of pointing errors can be obtained as[2]

$$P_{\mathrm{out},0}(\gamma_{th}) = \sum_{\rho=0}^{\infty} \left(\begin{array}{c} \alpha \\ \rho \end{array} \right) (-1)^{\rho} \exp\left[-\rho \left(\frac{\gamma_{th}}{\eta^2 \frac{P_1 (I^a)^2}{N_0}} \right)^{\frac{\beta}{2}} \right]$$

$$\times \left(1 - \sum_{p=0}^{m-1} \sum_{q=0}^{p} \frac{\mu (1-m)_p (-\delta)^p}{q! \phi^{p-q+1} (\frac{P_2 h_l}{N_0})^{p+1} p!} \gamma_{th}^{q} \exp(-\phi \gamma_{th}) \right), \tag{2.5}$$

where $(\cdot)_p$ is the Pochhammer symbol, $\delta = \frac{\Omega}{2b(2bm+\Omega)}$, and $\phi = \frac{\nu-\delta}{\overline{\gamma}_{RF}}$ [59]. In the presence of non-zero boresight pointing errors, the OP for State-0 can be easily derived. On the contrary, the OP expressions for State-1 and State-2 can be simply obtained from their CDFs by using $P_{out}(\gamma_{th}) = F(\gamma_{th})$. In the presence of non-zero boresight pointing error on State-1, the OP can be expressed as

$$P_{\mathrm{out},1}(\gamma_{th}) = \frac{\alpha g^2}{\beta} \exp(-\frac{s^2}{2\sigma_s^2}) \sum_{i=0}^{\infty} \frac{(-1)^i \Gamma(\alpha)}{(1+i)! \Gamma(\alpha - i)}$$

$$\times \sum_{j=0}^{\infty} \frac{(\frac{s^2 g^2}{2\sigma_s^2 \beta})^j}{j!} G_{j+2,j+3}^{j+2,1} \left(T_3'(i) \middle| \begin{array}{c} 1, \overbrace{T_1+1, \ldots, T_1+1}^{(j+1)\text{terms}} \\ 1, \underbrace{T_1, \ldots, T_1}_{(j+1)\text{terms}}, 0 \end{array} \right), \tag{2.6}$$

where $T_3'(i) = (1+i)\left(\frac{1}{\eta A_0} \sqrt{\frac{\gamma_{th}}{P_t (I^a)^2 / N_0}} \right)^{\beta}$. [3] In the absence of pointing error, the OP expression for State-1 can be given similarly to [19, eqn. (23)]. For State-2, the OP is given as

$$P_{\mathrm{out},2}(\gamma_{th}) = 1 - \sum_{p=0}^{m-1} \sum_{q=0}^{p} \frac{\mu (1-m)_p (-\delta)^p}{q! \phi^{p-q+1} (\frac{P_t h_l}{N_0})^{p+1} p!} \gamma_{th}^{q} \exp(-\phi \gamma_{th}). \tag{2.7}$$

Finally, the average performance of our proposed model can be given as $P_{out}(\gamma_{th}) = \sum_{k=0}^{2} p_k P_{out,k}(\gamma_{th})$.

2.2.2 High SNR analysis

In this subsection, we focus on the high SNR analysis and obtain the diversity order to gain more insights about the system behavior. The diversity order defines the slope of the OP versus the average SNR at asymptotically high SNR [22]. To do so, for FSO transmission in the absence of pointing errors, we apply $\exp(-x/a) \simeq 1 - x/a$ into the

---

[2] The infinite summation in (2.5) converges very fast after 5 to 10 iterations with 10^{-6} convergence error.

[3] The double infinite summations, require 3 to 5 terms to converge with a convergence error 2×10^{-7}.

CDF of EW fading given in [19]. Thus, after few manipulations, the asymptotic OP can be obtained as

$$P_{\text{out},1}^{\infty} = \left[\left(\frac{\gamma_{th}}{(\eta I^{a})^{2}}\right)^{\frac{\alpha\beta}{2}}\right]\left(\frac{1}{P_1/N_0}\right)^{\frac{\alpha\beta}{2}} = G_c(\overline{\gamma})^{-G_d^{FSO}}, \tag{2.8}$$

where $G_c = \left(\frac{\gamma_{th}}{(\eta I^{a})^{2}}\right)^{\frac{\alpha\beta}{2}}$ defines the shift of the curve in SNR and $G_d^{FSO} = \frac{\alpha\beta}{2}$ presents the diversity order.

For the RF transmission, we need to apply Maclaurin series expansion [58] for the exponential function and consider only the first term as the higher-order terms are neglected. Accordingly, the OP at high SNR can be obtained as

$$P_{\text{out},2}^{\infty} \simeq \mu\gamma_{th}\frac{1}{P_2 h_l/N_0}. \tag{2.9}$$

Thus, the diversity order is $G_d^{RF} = 1$ as we use a single antenna. Therefore, for State-0, where SC is adopted on the GS, the diversity gain is $G_d = \max(\frac{\alpha\beta}{2}, 1)$.

2.3 Numerical Results and Discussions

In this section, we evaluate the performance of our system in terms of OP. The satellite is assumed to be orbiting at an altitude of 500 km, communicating with a GS located at 0.8 km above sea level. For the FSO link, $\lambda = 1550$ nm wavelength is considered, whereas the RF link is operating at $f = 40$ GHz. For FSO communication, the zenith angle is set to $\xi = 65^\circ$, the nominal value of the refractive index is $C_0 = 5\times\ 10^{-14}$ [23], and the wind speed is set to $v_g = 2.8$ m/s for thin cirrus clouds. In the presence of heavy rain, we consider $C_0 = 0.4\times\ 10^{-14}$ [23], $v_g = 11.176$ m/s, and the specific attenuation of foggy weather is considered as 339.62 dB/km. For the RF link, we consider the presence of frequent heavy shadowing where $m = 1.0, b = 0.063, \Omega = 8.94\times 10^{-4}$. Moreover, the transmitter and receiver gains are set to $G_T = G_R = 45$ dB, the oxygen scattering parameter $\omega_{oxy} = 0.1$ dB/km, and the rain rate is given as $\mathscr{R} = 25$ mm/h. Furthermore, in the presence of non-zero boresight pointing errors, we set $\theta = 0.2$ mrad, $\sigma_s = 20$ cm and we consider different sizes of boresight and aperture. In all simulations, the threshold is set to $\gamma_{th} = 7$ dB. Without loss of generality, we simply assume that the different states of weather have the same probability of occurrence satisfying $\sum_{k=0}^{2} p_k = 1$. Thereafter, the probabilities are given as $p_k = 1/3$ for

$k = 0,1,2$. In addition, we compare our proposed scheme with the conventional dual-mode hybrid RF/FSO, in which the total power is always divided into $P_t/2$ for all states. Finally, the derived expressions are verified using MC simulations, however, not explicitly included to guarantee the clarity of the figure.

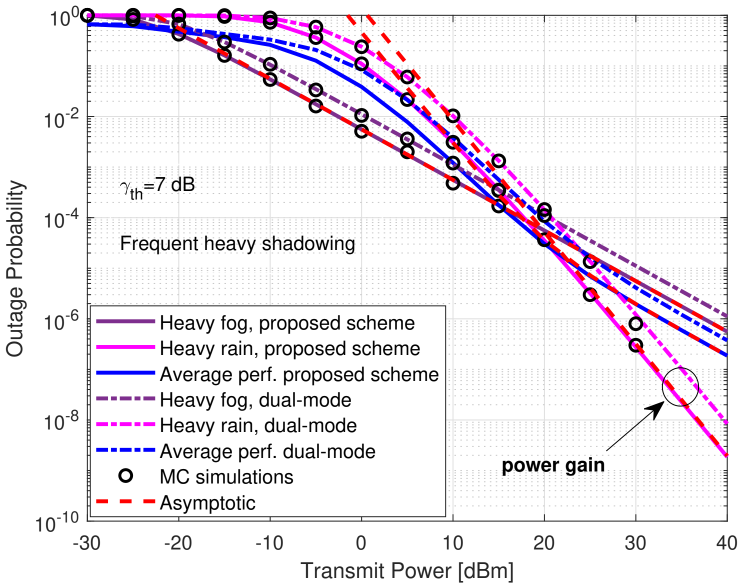

Figure 2.2 : OP performance of the proposed scheme.

Figure 2.2 illustrates the OP vs. transmit power for the proposed strategy in the absence of pointing errors. As we can see, the analytical results match the MC simulations with good accuracy. In addition, the high SNR analysis shows that for the heavy fog state, the overall gain is 1, whereas, for the heavy rain state, the overall gain is close to $\frac{\alpha\beta}{2} = 2.2117$. Moreover, as can be seen in the figure, at lower transmit power, the performance of foggy weather is better than the performance of rainy weather. However, after $P_t = 16$ dBm, the performance of rainy weather improves, causing a crossing point between the two curves. We also compare our proposed strategy with the dual-mode scheme. Furthermore, the figure shows that the proposed strategy achieves better outage performance than the conventional dual-mode hybrid RF/FSO communication.

Figure 2.3 investigates the impact of non-zero boresight pointing errors and the impact of aperture averaging. As can be seen in the figure, the average performance of the proposed strategy highly deteriorates in the presence of non-zero boresight pointing errors. As observed in the figure, for thin cloud conditions, the proposed hybrid

RF/FSO configuration performs better than FSO-only and RF-only transmissions. In addition, in the presence of non-zero boresight pointing errors, we can observe that the proposed strategy performs better than the dual-mode hybrid communication. Moreover, we can see that RF-only scheme outperforms FSO-only scheme due to the huge impact of non-zero boresight pointing errors. Furthermore, the results demonstrate that increasing the aperture size D_G enhances the overall performance by reducing the impact of atmospheric turbulence and pointing errors. Also, when the boresight displacement s increases, the misalignment between the satellite and the GS increases, therefore, less power is collected by the receiver aperture yielding a serious degradation in the OP performance.

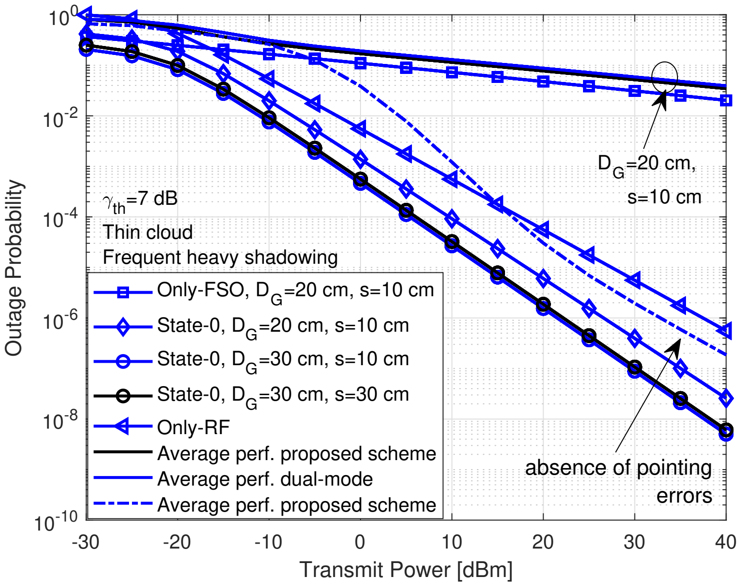

Figure 2.3 : Impact of non-zero boresight pointing errors in terms of OP.

In summary, we present the main findings of this work.

- We observe from the results that the proposed model is superior to the dual-mode hybrid RF/FSO communication method for SatCom.
- In the absence of pointing errors, only at lower transmission power, the RF communication outperforms FSO communication. However, in the presence of non-zero boresight pointing errors, the RF transmission performs better than FSO transmission.

- The results have shown that the non-zero boresight pointing error strongly deteriorates the overall performance of FSO communication as it increases the misalignment between communicating parts.

- It is shown in Figure 2.3 that the aperture averaging technique is an effective solution in SatCom to mitigate the effects of atmospheric turbulence and pointing errors.

2.4 Summary and Discussion

In this chapter, we proposed a new soft-switching setup for hybrid RF/FSO downlink SatCom. According to the context-aware by the measurements of sensors system, an LEO satellite adapts its power and switches between RF and FSO links by selecting the channel with the highest performance based on the weather conditions. To quantify the performance of our model, OP expressions are derived and simulation results are provided to confirm the accuracy of our analytical results. Moreover, the results have shown that our proposed strategy improves power efficiency compared to the conventional dual-mode hybrid RF/FSO. Furthermore, we have studied the impact of non-zero boresight pointing errors to observe the misalignment effect for hybrid RF/FSO communication. The study indicates that increasing the boresight leads to severe performance degradation. However, the aperture averaging technique can be used to improve the performance and alleviate pointing error effects.

In the next chapter, we continue by investigating the physical performance of hybrid RF/FSO communication for SatCom systems by proposing a novel dual-hop SatCom architecture by using a HAPS node as a relay.

3. HAPS SELECTION FOR HYBRID RF/FSO SATELLITE NETWORKS

To study the physical layer performance of RF and FSO channels in SatCom systems, in the previous chapter, we introduced the downlink single-hop hybrid RF/FSO communication between an LEO satellite and a GS. Similarly, in this chapter, we also continue to investigate the physical performance of hybrid RF/FSO communication. Different from the previously proposed model, in order to enhance the communication performance and ensure reliable communication, we propose a novel dual-hop multi-relay hybrid RF/FSO communication by using HAPS nodes as relays between the LEO satellite and the ground user. A HAPS system that can provide the best channel characteristics is selected in the first hop and acts as a decode-and-forward (DF) relay. In the second hop, the selected HAPS decodes and forwards the signal to the GS through hybrid RF/FSO communication, where both RF and FSO channels are used based on the soft-switching model.

As mentioned above, this work has been published in the following journal paper:

O. Ben Yahia, E. Erdogan, G. Karabulut Kurt, I. Altunbas, and H. Yanikomeroglu, “HAPS selection for hybrid RF/FSO satellite networks”, IEEE Transactions on Aerospace and Electronic Systems (early access), pp. 1–13, 2022.

This chapter is organized as follows: The signals and system model are outlined in Section 3.1. Channel modeling and impairments are described in Section 3.2. The mathematical expressions of OP and asymptotic analysis are derived in Section 3.3. In Section 3.4, numerical results are presented and discussed, followed by design guidelines. Finally, the conclusion is provided in Section 3.5.

3.1 Signals and System Model

As depicted in Figure 3.1, we consider a hybrid cooperative SatCom model consisting of an LEO satellite (S), a GS (G), and N DF HAPS ($\mathscr{H}$) nodes distributed randomly [60]. The direct link between S and G is unavailable due to atmospheric attenuation

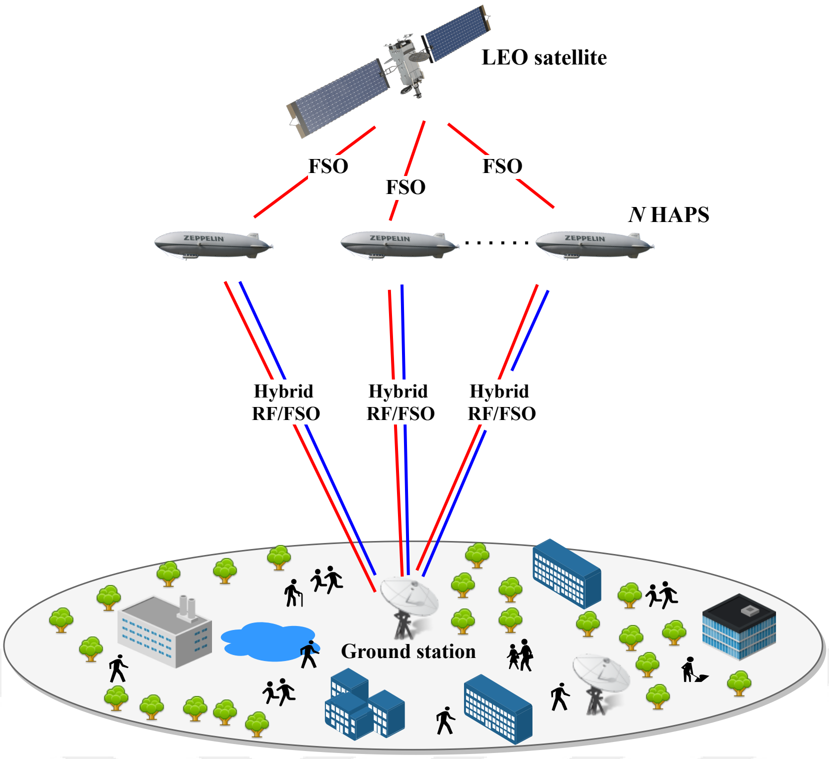

Figure 3.1 : Illustration of the HAPS node selection for hybrid RF/FSO SatCom.

or heavy shadowing. In this setup, S selects the HAPS node denoted by ($\mathscr{H}_J$) that can provide the best channel characteristics, based on the channel state information (CSI) feedback from the HAPS nodes [61]. In the first hop, S transmits its information to $\mathscr{H}_J$ by using FSO communication. In the second hop, $\mathscr{H}_J$ decodes the optical received signal and forwards it to G by using hybrid RF/FSO communication. At the destination node G, the received signal with the highest SNR is selected to maximize the utilization of the channel spectrum. In the S to $\mathscr{H}_J$ communication, the Doppler shift effect can be reduced to enable reliable communication. Furthermore, due to the appealing quasi-stationary nature of the HAPS node, tracking and precision problems can be ignored, as well as the introduction of the Doppler shift. In this setup, the FSO links follow the EW fading, whereas the RF link is modeled with the shadowed-Rician distribution. Table 3.1 summarizes all the parameters used in this work.

3.1.1 Satellite-HAPS communication

Considering the communication between S and $\mathscr{H}_j$, stratospheric turbulence-induced fading can be caused by non-static stratospheric winds and temperature variations due to altitude and pressure. By assuming stratospheric turbulence-induced fading and

Table 3.1 : List of parameters.

Parameter	Definition
N	Number of HAPS systems
λ	Optical wavelength
K	Optical wave number
L	Propagation distance
ξ	Zenith angle
$\mathscr{D}$	Hard receiver aperture diameter
Θ	Elevation angle
u	RMS wind speed
h	Altitude
h_S	Altitude of the satellite
h_E	The GS's elevation above mean sea level
$h_{\mathscr{H}}$	Altitude of the HAPS node
α, β	Shape parameters of the EW fading
η	Fading severity parameter of the EW fading
ω	Geometrical attenuation coefficient
$\mathscr{L}_{\mathscr{W}}$	Liquid water content
V	Visibility
Ψ	Stratospheric attenuation coefficient
σ_R^2	Rytov variance
C_n^2	Refractive index constant
σ_I^2	Scintillation index
σ_s	Jitter standard deviation
$\mathscr{F}$	Path loss
m	Nakagami-m fading severity parameter
θ	Transmit divergence angle
φ_{rain}	Rain attenuation coefficient
φ_{oxy}	Oxygen attenuation coefficient
$\mathscr{R}$	Rain rate
n_f	Noise figure
T	Temperature
B	Bandwidth
γ_{th}	Predefined threshold for acceptable communication quality

stratospheric attenuation, the received signal[1] by $\mathscr{H}_j$ can be expressed as follows:

$$y_{S\mathscr{H}_j} = \sqrt{\zeta P_S} I_{S\mathscr{H}_j} x_S + n_{\mathscr{H}}, \tag{3.1}$$

where $0 \leq \zeta \leq 1$ is the optical-to-electrical conversion coefficient, P_S is the transmit power of S, $I_{S\mathscr{H}_j}$ represents the irradiance of the FSO channel, which can be expressed as $I_{S\mathscr{H}_j} = I^a_{S\mathscr{H}_j} I^t_{S\mathscr{H}_j}$, where $I^a_{S\mathscr{H}_j}$ stands for the stratospheric attenuation, $I^t_{S\mathscr{H}_j}$ indicates

---

[1] As widely adopted in the literature, we assume a time-invariant statistical model, so that we can obtain the OP in closed-form.

the stratospheric turbulence, x_S denotes the transmitted signal, and n_H is the AWGN with one-sided power spectral density N_0. With respect to (3.1), the instantaneous received SNR at $\mathscr{H}_j$ can be expressed as

$$\gamma_{S\mathscr{H}_j} = \frac{\zeta P_S I^2_{S\mathscr{H}_j}}{N_0} = \overline{\gamma}_{S\mathscr{H}_j} I^2_{S\mathscr{H}_j}, \tag{3.2}$$

where $\overline{\gamma}_{S\mathscr{H}_j} = \frac{\zeta P_S}{N_0}$ is the average SNR with $\mathbb{E}[I^2_{S\mathscr{H}_j}] = 1$.

In this setup, the HAPS selection is based on the satellite-HAPS channel quality, where the HAPS node with the best channel quality among N HAPS is selected to maximize the instantaneous SNR between S and $\mathscr{H}_j$ as follows:

$$J = \arg \max_{j=1,\ldots,N} [\gamma_{S\mathscr{H}_j}], \tag{3.3}$$

where $1 \leq j \leq N$ shows the HAPS index. Considering the EW fading, the CDF of $\gamma_{S\mathscr{H}_J}$ can be given as follows [18]:

$$F_{\gamma_{S\mathscr{H}_J}}(\gamma) = \prod_{j=1}^{N} \left(1 - \exp\left[-\left(\frac{\gamma}{(\eta_{S\mathscr{H}_j} I^a_{S\mathscr{H}_j})^2 \overline{\gamma}_{S\mathscr{H}_j}} \right)^{\frac{\beta_{S\mathscr{H}_j}}{2}} \right] \right)^{\alpha_{S\mathscr{H}_j}}, \tag{3.4}$$

where $\eta_{S\mathscr{H}_j}$ is the scale parameter, $\alpha_{S\mathscr{H}_j}$ and $\beta_{S\mathscr{H}_j}$ present the shape parameters which are directly related to the atmosphere and the scintillation index. These parameters can be expressed as follows [17]:

$$\begin{aligned}
\alpha_{S\mathscr{H}_j} &= \frac{7.220 \times \sigma^{2/3}_{I_{S\mathscr{H}_j}}}{\Gamma\left(2.487\sigma^{2/6}_{I_{S\mathscr{H}_j}} - 0.104\right)}, \\
\beta_{S\mathscr{H}_j} &= 1.012\left(\alpha_{S\mathscr{H}_j}\sigma^2_{I_{S\mathscr{H}_j}}\right)^{-13/25} + 0.142, \\
\eta_{S\mathscr{H}_j} &= \frac{1}{\alpha_{S\mathscr{H}_j}\Gamma\left(1 + 1/\beta_{S\mathscr{H}_j}\right) \mathrm{g}_1(\alpha_{S\mathscr{H}_j}, \beta_{S\mathscr{H}_j})},
\end{aligned} \tag{3.5}$$

where $\Gamma(\cdot)$ indicates the Gamma function and $\mathrm{g}_1(\alpha_{S\mathscr{H}_j}, \beta_{S\mathscr{H}_j})$ is $\alpha_{S\mathscr{H}_j}$ and $\beta_{S\mathscr{H}_j}$-dependent constant variable given by [19]

$$\mathrm{g}_1(\alpha_{S\mathscr{H}_j}, \beta_{S\mathscr{H}_j}) = \sum_{k=0}^{\infty} \frac{(-1)^k \Gamma(\alpha_{S\mathscr{H}_j})}{k!(k+1)^{1+1/\beta_{S\mathscr{H}_j}} \Gamma(\alpha_{S\mathscr{H}_j} - k)}. \tag{3.6}$$

$\sigma^2_{I_{S\mathscr{H}_j}}$ is the scintillation index, which can be written as follows [13, Sect. (12)]:

$$\sigma^2_{I_{S\mathscr{H}_j}} = \exp\left[\frac{0.49\sigma^2_{R_{S\mathscr{H}_j}}}{(1 + 1.11\sigma^{12/5}_{R_{S\mathscr{H}_j}})^{7/6}} + \frac{0.51\sigma^2_{R_{S\mathscr{H}_j}}}{(1 + 0.69\sigma^{12/5}_{R_{S\mathscr{H}_j}})^{5/6}} \right] - 1, \tag{3.7}$$

where $\sigma^2_{R_{S\mathcal{H}_j}}$ denotes the Rytov variance given as follows [13, Sect. (12)]:

$$\sigma^2_{R_{S\mathcal{H}_j}} = 2.25K^{7/6}\sec^{11/6}(\xi_{S\mathcal{H}_j})\int_{h_{\mathcal{H}}}^{h_S} C^2_{n_{S\mathcal{H}_j}}(h)(h-h_{\mathcal{H}})^{5/6}dh. \tag{3.8}$$

Here, $K=\frac{2\pi}{\lambda_{FSO}}$ denotes the optical wave number, $\xi_{S\mathcal{H}_j}$ is the zenith angle, h_S stands for the altitude of the satellite, $h_{\mathcal{H}}$ indicates the altitude of the selected HAPS above ground, and $C^2_{n_{S\mathcal{H}_j}}(h)$ represents the refractive-index parameter depending on the altitude h expressed as follows [35]:

$$\begin{aligned} C^2_{n_{S\mathcal{H}_j}}(h) &= 8.148\times 10^{-56}u^2_{S\mathcal{H}_j}h^{10}\exp(-h/1000) \\ &+2.7\times 10^{-16}\exp(-h/1500)+C_0\exp(-h/100), \end{aligned} \tag{3.9}$$

where $u_{S\mathcal{H}_j}=\sqrt{v^2_{S\mathcal{H}_j}+30.69v_{S\mathcal{H}_j}+348.91}$ represents the root-mean-square (RMS) of the wind speed, $v_{S\mathcal{H}_j}$ is the wind speed in m/s at $\mathcal{H}_j$, and C_0 is the nominal value of $C^2_{n_{S\mathcal{H}_j}}(h)$ at the HAPS node in $\mathrm{m}^{-2/3}$.

3.1.2 HAPS-ground station communication

3.1.2.1 FSO communication

Temperature and pressure gradients can cause variations in the atmosphere's refractive index in the form of eddies causing atmospheric turbulence-induced fading. In the presence of atmospheric turbulence, the instantaneous SNR at G can be expressed as follows:

$$\gamma^{FSO}_{\mathcal{H}_J G} = \frac{\zeta P_{\mathcal{H}_J} I^2_{\mathcal{H}_J G}}{N_0} = \overline{\gamma}^{FSO}_{\mathcal{H}_J G} I^2_{\mathcal{H}_J G}, \tag{3.10}$$

where $P_{\mathcal{H}_J}$ represents the transmit power of the selected HAPS, $I_{\mathcal{H}_J G}$ denotes the FSO channel gain (irradiance), which is given as $I_{\mathcal{H}_J G}=I^t_{\mathcal{H}_J G}I^a_{\mathcal{H}_J G}$, where $I^t_{\mathcal{H}_J G}$ indicates the atmospheric turbulence-induced fading and $I^a_{\mathcal{H}_J G}$ indicates the atmospheric attenuation. Moreover, $\overline{\gamma}^{FSO}_{\mathcal{H}_J G}=\frac{\zeta P_{\mathcal{H}_J}}{N_0}$ is the average FSO SNR of the $\mathcal{H}_J$ to G link with $\mathbb{E}[I^2_{\mathcal{H}_J G}]=1$. Finally, the CDF of $\gamma^{FSO}_{\mathcal{H}_J G}$ can be expressed similarly to (3.4) and the fading severity parameters can be obtained as in (3.5) by replacing $S\mathcal{H}_j$ subscript with $\mathcal{H}_J G$.

3.1.2.2 RF communication

Let $x_{\mathscr{H}_J}$ denote the transmitted signal of $\mathscr{H}_J$ with power $P_{\mathscr{H}_J}$ through the RF link. The received signal at G can be expressed as follows:

$$y_{\mathscr{H}_J G} = \sqrt{P_{\mathscr{H}_J} \mathscr{F}_{\mathscr{H}_J G}} f_{\mathscr{H}_J G} x_{\mathscr{H}_J} + n_G, \tag{3.11}$$

where n_G is the zero-mean AWGN with power spectral density N_0, $f_{\mathscr{H}_J G}$ is the channel coefficient of the RF link that follows the shadowed-Rician fading, and $\mathscr{F}_{\mathscr{H}_J G}$ is the path-loss model which can be expressed as [23]

$$\begin{aligned} \mathscr{F}_{\mathscr{H}_J G}[dB] = G_T + G_R - 20\log_{10}\left(\frac{4\pi L_{\mathscr{H}_J G}}{\lambda_{RF}}\right) \\ - \varphi_{oxy} L_{\mathscr{H}_J G} - \varphi_{rain}^{RF} L_{\mathscr{H}_J G}, \end{aligned} \tag{3.12}$$

where G_T and G_R represent the gains of the transmitting and receiving antennas in dB, respectively. $L_{\mathscr{H}_J G}$ indicates the propagation distance between $\mathscr{H}_J$ and G, λ_{RF} is the RF wavelength, φ_{oxy} and φ_{rain}^{RF} are the RF attenuation coefficients due to the oxygen and rain scattering [55]. In RF communication, the main attenuation factor is rain, where the corresponding attenuation increases linearly in relation to the rate of rainfall. Thus, the rain attenuation coefficient φ_{rain}^{RF} (dB/km) can be expressed as [56]

$$\varphi_{rain}^{RF} = k_r \mathscr{R}^{\rho}. \tag{3.13}$$

The parameters k_r and ρ depend on the channel's wavelength λ_{RF}(GHz) and can be given as follows [56]:

$$\begin{aligned} k_r &= [k_H + k_V + (k_H - k_V)\cos^2(\Theta)\cos(2\iota)]/2, \\ \rho &= [k_H \rho_H + k_V \rho_V + (k_H \rho_H - k_V \rho_V)\cos^2(\Theta)\cos(2\iota)]/2k_r, \end{aligned} \tag{3.14}$$

where the constants k_H, k_V, ρ_H, and ρ_V are given in [56] and ι is the polarization tilt angle [56]. Therefore, with the help of (3.11), the instantaneous SNR at G can be written as follows:

$$\gamma_{\mathscr{H}_J G}^{RF} = \frac{P_{\mathscr{H}_J} \mathscr{F}_{\mathscr{H}_J G} |f_{\mathscr{H}_J G}|^2}{N_0} = \overline{\gamma}_{\mathscr{H}_J G}^{RF} |f_{\mathscr{H}_J G}|^2. \tag{3.15}$$

where $\overline{\gamma}_{\mathscr{H}_J G}^{RF} = \frac{P_{\mathscr{H}_J} \mathscr{F}_{\mathscr{H}_J G}}{N_0}$ presents the average SNR for the RF channel between $\mathscr{H}_J$ and G with $\mathbb{E}[|f_{\mathscr{H}_J G}|^2] = 1$. Furthermore, the probability density function (PDF) of the received SNR for the RF link is given by [59]:

$$f_{\gamma_{\mathscr{H}_J G}}^{RF}(\gamma) = \sum_{l=0}^{m-1} \frac{\mu (1-m)_l (-\delta)^l}{(\overline{\gamma}_{\mathscr{H}_J G}^{RF})^{l+1} (l!)^2} (\gamma)^l \exp(-\vartheta\gamma), \tag{3.16}$$

where $\mu = \frac{1}{2b}(\frac{2bm}{2bm+\Omega})^m$, $\delta = \frac{\Omega}{2b(2bm+\Omega)}$, $\vartheta = \frac{\nu-\delta}{\gamma^{RF}_{\mathscr{H}_j G}}$, and $\nu = \frac{1}{2b}$ with m is a positive integer that indicate the Nakagami-m fading parameter. Furthermore, Ω and $2b$ are the average power of the LOS component and multi-path component.

3.2 Attenuation, Pointing Loss, and Temperature Variations

3.2.1 Satellite-HAPS communication

3.2.1.1 Stratospheric attenuation

In addition to its low costs and faster services, at the HAPS level, there are no clouds, which means clean solar energy without atmospheric pollution [62]. However, for long-distance communication, the possibility of volcanic eruptions and resulting aerosol emissions needs to be considered, given that such aerosols can penetrate the stratosphere [6]. Moreover, stratospheric attenuation caused by molecular absorption and scattering by droplets can take place [7]. Considering the stratospheric conditions, polar clouds can cause temperature differences between HAPS and satellites and this can result in fluctuations in the optical beam. In optical communication, the stratospheric attenuation can be modeled as follows:

$$I^a_{S\mathscr{H}_j} = \exp(-\Psi_{S\mathscr{H}_j} L_{S\mathscr{H}_j}), \tag{3.17}$$

where $\Psi_{S\mathscr{H}_j}$ represents the attenuation factor between the satellite and the HAPS systems and $L_{S\mathscr{H}_j}$ is the propagation distance between S and $\mathscr{H}_j$ [23]. In Table 3.2, we present stratospheric aerosol models for different levels of volcanic activity at the optical wavelength $\lambda_{FSO} = 1550$ nm [7].

Table 3.2 : Stratospheric attenuation coefficient for $h_{\mathscr{H}} = 19$ km.

Stratospheric aerosol model	Attenuation coefficient Ψ (km^{-1})
Extreme volcanic	2×10^{-1}
High volcanic	5×10^{-2}
Moderate volcanic	8×10^{-3}
Background volcanic	10^{-4}

3.2.1.2 Pointing errors

For FSO communication, another critical impairment consists of beam-pointing errors, which significantly affect the performance of networks, especially over large distances.

Due to vibrations in the transmitter telescope and thermal expansion, a misalignment between the transmitter and receiver can occur. Pointing errors can be divided into two components. First, the boresight, which is the fixed displacement between the beam center and center of the detector. Second, jitter, which represents the random offset of the beam center at the detector plane [51]. In the presence of pointing errors, the irradiance of the FSO channel can be expressed as $I_{S\mathscr{H}_j} = I^a_{S\mathscr{H}_j} I^t_{S\mathscr{H}_j} I^p_{S\mathscr{H}_j}$, where $I^p_{S\mathscr{H}_j}$ indicates the pointing errors component. In our model, we will assume zero-boresight pointing errors for the link between S and all instances of H. Hence, the PDF of $I^p_{S\mathscr{H}_j}$ can be given as follows [52]:

$$f_{I^p_{S\mathscr{H}_j}}(I^p) = \frac{g^2 \exp(\frac{-s^2}{2\sigma_s^2})}{A_0^{g^2}} (I^p)^{g^2-1} I_0\left(\frac{s}{\sigma_s^2}\sqrt{\frac{-w_{eq}^2 \ln \frac{I^p}{A_0}}{2}}\right), \tag{3.18}$$

where the parameter $g = w_{eq}/(2\sigma_s)$ is the ratio between the equivalent beam w_{eq} and the jitter standard deviation σ_s, where $w_{eq}^2 = w_z^2 \sqrt{\pi}\mathrm{erf}(y)/(2ye^{(-y^2)})$. $y = \sqrt{\pi/2\varpi}/w_z$ indicates the ratio of the aperture radius ϖ and the beam-width w_z at distance z, $w_z = \theta z$ with θ is the beam divergence angle, and $\mathrm{erf}(\cdot)$ indicates the error function. Moreover, s denotes the boresight, which is considered to be zero in our case. Finally, $A_0 = [\mathrm{erf}(y)]^2$ defines the gathered optical power for a zero difference between the optical spot center and the detector center, and $I_0(x)$ defines the modified Bessel function of the first kind with order zero [52].

3.2.1.3 Aperture averaging

For downlink optical communication, when the receiving aperture is lower than the correlation width of irradiance fluctuations, the turbulence-induced signal fluctuations can deteriorate the system performance. Hence, aperture averaging takes place, and increasing the aperture size not only improves the signal level but also reduces the fluctuations in the received signal. More specifically, the aperture size-dependent scintillation index can be given as follows [13, Sect. (12)]:

$$\sigma^2_{I_{S\mathscr{H}_j}} = 8.7k^{7/6}(h_S - h_{\mathscr{H}})^{5/6} \sec^{11/6}(\xi_{S\mathscr{H}_j}) \times \Re\left\{ \int_{h_{\mathscr{H}}}^{h_S} C^2_{n_{S\mathscr{H}_j}}(h) \right.$$
$$\left. \times \left[\left(\frac{k\mathscr{D}^2_{S\mathscr{H}_j}}{16L_{S\mathscr{H}_j}} + i\frac{h - h_{\mathscr{H}}}{h_S - h_{\mathscr{H}}} \right)^{5/6} - \left(\frac{k\mathscr{D}^2_{S\mathscr{H}_j}}{16L_{S\mathscr{H}_j}} \right)^{5/6} \right] \right\} dh, \tag{3.19}$$

where $\mathscr{D}_{S\mathscr{H}_j}$ is the hard aperture diameter of the HAPS node in meter.

3.2.2 HAPS-ground station communication

In $\mathscr{H}_J$ to G communication, we adopt hybrid RF/FSO communication in which the FSO or RF channel is selected at ground level depending on the channel characteristics. In other words, G chooses the best link that maximizes the instantaneous SNR between $\mathscr{H}_J$ and G.

3.2.2.1 Atmospheric attenuation

The main problem in the optical wireless links is attenuation resulting from scattering and absorption. The scattering of optical signals is mainly caused by weather conditions such as clouds, fog, snow, and rain [14].

In optical communication, Mie scattering is considered to be one of the main sources of signal loss in downlink channels operating at frequencies below 375 THz. It affects the signal when the wavelength and the diameter of the particles present in the medium are equals. First, we calculate the wavelength-dependent empirical coefficients as follows [63]:

$$\begin{aligned}
a &= -0.000545\lambda_{FSO}^2 + 0.002\lambda_{FSO} - 0.0038\\
b &= 0.00628\lambda_{FSO}^2 - 0.0232\lambda_{FSO} + 0.0439\\
c &= -0.028\lambda_{FSO}^2 + 0.101\lambda_{FSO} - 0.18\\
d &= -0.228\lambda_{FSO}^3 + 0.922\lambda_{FSO}^2 - 1.26\lambda_{FSO} + 0.719,
\end{aligned} \tag{3.20}$$

where h_E indicates the altitude of G above sea level. Then, the extinction ratio can be expressed as follows [63]:

$$\tau = ah_E^3 + bh_E^2 + ch_E + d, \tag{3.21}$$

and the attenuation due to Mie scattering is given as follows:

$$I_{\mathscr{H}_J G}^m = \exp\left(-\frac{\tau}{\sin(\Theta)}\right), \tag{3.22}$$

where Θ indicates the elevation angle of the GS.

In optical communication, geometrical scattering can also deteriorate the signal in the atmosphere. In geometrical scattering, fog and cloud-induced fading are the primary causes of FSO communication deterioration. To estimate the attenuation based on the visibility range parameters, the well-known Kim's model can be used to define the attenuation coefficient as [14]

$$\omega = \frac{3.91}{V}\left(\frac{\lambda_{FSO}}{550}\right)^{-x}, \tag{3.23}$$

where V defines the visibility range in km, and x implies the particle size coefficient of scattering given by the Kim's model as follows:

$$x = \begin{cases} 1.6 & V > 50 \\ 1.3 & 6 < V < 50 \\ 0.16V + 0.34 & 1 < V < 6 \\ V - 0.5 & 0.5 < V < 1 \\ 0 & V < 0.5. \end{cases} \tag{3.24}$$

Table 3.3 : Atmospheric attenuation parameters at $\lambda_{FSO} = 1550$ nm.

Fog	V (km)	Attenuation coefficient ω (dB/km)
Dense	0.05	339.62
Thick	0.20	84.90
Moderate	0.50	33.96
Light	0.77	16.67
Thin	1.90	4.59

Table 3.4 : Geometrical scattering parameters.

Cloud type	$\mathscr{N}$ (cm^{-3})	$\mathscr{LW}$ (g/m^{-3})	V (km)
Cumulus	250	1.0	0.0280
Stratus	250	0.29	0.0626
Stratocumulus	250	0.15	0.0959
Altostratus	400	0.41	0.0369
Nimbostratus	200	0.65	0.0429
Cirrus	0.025	0.06405	64.66
Thin cirrus	0.5	3.128×10^{-4}	290.69

In Table 3.3, the visibility and attenuation coefficient parameters are presented for different fog conditions. Based on this model, for different cloud types, the visibility can be given as [64]:

$$V = \frac{1.002}{(\mathscr{L}_{\mathscr{W}}\mathscr{N})^{0.6473}}, \tag{3.25}$$

where $\mathscr{L}_{\mathscr{W}}$ indicates the liquid water content and $\mathscr{N}$ presents the cloud number concentration.

The corresponding parameters are summarized in Table 3.4. Accordingly, the geometrical attenuation is given by applying the Beer-Lambert law as $I^{g}_{\mathscr{H}_J G} =$

$\exp(-\omega L_{\mathscr{H}_J G})$. Hence, the total atmospheric attenuation at ground level can be expressed as [65]:

$$I^a_{\mathscr{H}_J G} = I^m_{\mathscr{H}_J G} I^g_{\mathscr{H}_J G}. \tag{3.26}$$

Among the different atmospheric effects on the FSO link, rain is the weakest attenuation factor. However, the size of rain droplets increases when the rainfall rate increases, so it may cause refraction and reflection. Considering the FSO communication, the specific rain attenuation coefficient can be expressed on the basis of the rainfall rate $\mathscr{R}$ (mm/h) as follows [14]:

$$\varphi^{FSO}_{rain} = 1.076\mathscr{R}^{0.67}. \tag{3.27}$$

Therefore, the rain attenuation can be obtained as $I^{rain}_{\mathscr{H}_J G} = \exp(-\varphi^{FSO}_{rain} L_{\mathscr{H}_J G})$. Thus, in the presence of rain, the total attenuation can be considered as $I^a_{\mathscr{H}_J G} = I^m_{\mathscr{H}_J G} I^g_{\mathscr{H}_J G} I^{rain}_{\mathscr{H}_J G}$.

3.2.2.2 Aperture averaging

Aperture averaging technique is also considered in the second-hop link to improve the communication from $\mathscr{H}_J$ to G. Therefore, the scintillation index dependent aperture diameter can be similarly expressed as in (3.19) by just changing the subscripts as $\sigma^2_{I_{\mathscr{H}_J G}}$ for the scintillation index and $\mathscr{D}_{\mathscr{H}_J G}$ for the hard aperture.

3.2.2.3 Pointing errors

In this subsection, pointing errors due to misalignment between $\mathscr{H}_J$ and G is taken into consideration. Thus, in the presence of zero-boresight pointing errors for $\mathscr{H}_J$ to G communication, the irradiance of the channel can be written as $I_{\mathscr{H}_J G} = I^t_{\mathscr{H}_J G} I^a_{\mathscr{H}_J G} I^p_{\mathscr{H}_J G}$, where $I^p_{\mathscr{H}_J G}$ shows the pointing errors. The PDF of $I^p_{\mathscr{H}_J G}$ can be written similarly as in (3.18).

3.2.3 Impact of the temperature variations

The Earth's atmosphere extends up to 700 km above ground level and is divided into four distinct layers on the basis of temperature. SatCom can be affected by thermal noise, which varies with altitude. For our proposed model, we consider the troposphere and stratosphere layers [13, Sect. (1)].

- Troposphere: This layer extends up to 11 km and contains 75% of the Earth's atmospheric mass. The maximum air temperature takes place near the ground and decreases up to -55°C with an increase of altitude.
- Stratosphere: This layer starts at 20 km and extends up to 48 km. The air temperature level decreases with an increase of the altitude starting from -55°C.

We analyze the impact of the thermal noise associated with these layers. We show that the use of the HAPS node improves the system's performance as the link between the satellite and the HAPS node is less affected by the noise. The noise power N_0 can be given as $N_0 = P_n n_f$, where n_f is the noise figure of the receiver and P_n is given as follows [33]:

$$P_n(dB) = k + T + B, \tag{3.28}$$

where $k = -228.6$ dBW/K/Hz represents the Boltzmann's constant, T is the system noise temperature in dBK, and B denotes the noise bandwidth in dBHz. Please note that (3.28) can be used either for a HAPS node or GS, depending on the temperature.

3.3 Performance Analysis

3.3.1 Outage probability

As mentioned before, the OP can be expressed as follows [10]:

$$\begin{aligned} P_{out} &= \Pr[\gamma_0 \leq \gamma_{th}] \qquad (3.29) \\ &= F_{\gamma_0}(\gamma_{th}), \end{aligned}$$

where $F_{\gamma_0}(\gamma_{th})$ is the CDF of the end-to-end SNR at G, which can be given as:

$$\gamma_0 = \min(\gamma_{S\mathscr{H}_J}, \gamma_{\mathscr{H}_J G}), \tag{3.30}$$

where $\gamma_{\mathscr{H}_J G} = \max(\gamma^{FSO}_{\mathscr{H}_J G}, \gamma^{RF}_{\mathscr{H}_J G})$ is the output SNR of the SC at G, and the CDF of the γ_0 can be written as follows:

$$\begin{aligned} F_{\gamma_0}(\gamma) &= 1 - \Pr[\gamma_{S\mathscr{H}_J} > \gamma] \Pr[\gamma_{\mathscr{H}_J G} > \gamma] \\ &= 1 - \left(1 - F_{\gamma_{S\mathscr{H}_J}}(\gamma)\right)\left(1 - F_{\gamma_{\mathscr{H}_J G}}(\gamma)\right) \\ &= 1 - \left(1 - F_{\gamma_{S\mathscr{H}_J}}(\gamma)\right)\left(1 - \left(F_{\gamma^{FSO}_{\mathscr{H}_J G}}(\gamma) F_{\gamma^{RF}_{\mathscr{H}_J G}}(\gamma)\right)\right), \end{aligned} \tag{3.31}$$

where $F_{\gamma^{FSO}_{\mathscr{H}_J G}}(\gamma)$ and $F_{\gamma^{RF}_{\mathscr{H}_J G}}(\gamma)$ are the CDF of $\gamma^{FSO}_{\mathscr{H}_J G}$ and $\gamma^{RF}_{\mathscr{H}_J G}$, respectively, given as follows:

$$F_{\gamma^{FSO}_{\mathscr{H}_J G}}(\gamma) = \sum_{\rho=0}^{\infty} \begin{pmatrix} \alpha_{\mathscr{H}_J G} \\ \rho \end{pmatrix} (-1)^{\rho} \times \exp\left[-\rho \left(\frac{\gamma}{(\eta_{\mathscr{H}_J G} I^{a}_{\mathscr{H}_J G})^{2} \overline{\gamma}^{FSO}_{\mathscr{H}_J G}} \right)^{\frac{\beta_{\mathscr{H}_J G}}{2}} \right], \tag{3.32}$$

$$F_{\gamma^{RF}_{\mathscr{H}_J G}}(\gamma) = 1 - \sum_{l=0}^{m-1} \sum_{q=0}^{l} \frac{\mu (1-m)_{l} (-\delta)^{l}}{q! \vartheta^{l-q+1} (\overline{\gamma}^{RF}_{\mathscr{H}_J G})^{l+1} l!} \times (\gamma)^{q} \exp(-\vartheta \gamma). \tag{3.33}$$

Furthermore, $F_{\gamma_{S\mathscr{H}_J}}(\gamma)$ is the CDF of $\gamma_{S\mathscr{H}_J}$, which can be expressed as given in (3.4) in the absence of pointing errors. However, in the presence of pointing errors, $F_{\gamma_{S\mathscr{H}_J}}(\gamma)$ can be obtained as [51]:

$$F_{\gamma_{S\mathscr{H}_J}}(\gamma) = \prod_{j=1}^{N} \left(\frac{\alpha_{S\mathscr{H}_j} g^{2}}{\beta_{S\mathscr{H}_j}} \left(\frac{1}{\eta_{S\mathscr{H}_j} A_0} \sqrt{\frac{\gamma}{\overline{\gamma}_{S\mathscr{H}_j} (I^{a}_{S\mathscr{H}_j})^{2}}} \right)^{g^{2}} \times \sum_{i=0}^{\infty} T_2(i) G^{2,1}_{2,3} \left(T_3(i) \middle| \begin{matrix} 1-T_1, 1 \\ 0, 1-T_1, -T_1 \end{matrix} \right) \right), \tag{3.34}$$

where $T_1 = g^{2}/\beta_{S\mathscr{H}_j}$, $T_2(i) = (-1)^{i} \Gamma(\alpha_{S\mathscr{H}_j}) / [i! \Gamma(\alpha_{S\mathscr{H}_j} - i)(1+i)^{1-T_1}]$ and $T_3(i) = (1+i) \left(\frac{1}{\eta_{S\mathscr{H}_j} A_0} \sqrt{\frac{\gamma}{\overline{\gamma}_{S\mathscr{H}_j} (I^{a}_{S\mathscr{H}_j})^{2}}} \right)^{\beta_{S\mathscr{H}_j}}$.

Similarly, in the presence of zero-boresight pointing errors from $\mathscr{H}_J$ to G, the CDF of $\gamma^{FSO}_{\mathscr{H}_J G}$ can be written as in (3.34) after changing the subscripts by $\mathscr{H}_J G$.

Finally, by substituting (3.32) and (3.33) into (3.31), then into (3.29), the final expression of the OP can be obtained, as can be seen in (3.35)

3.3.2 High SNR analysis

In this subsection, the asymptotic expressions of OP are derived to get the diversity order of the proposed system. Similar to (3.31), the OP at higher SNR can be written

$$
\begin{aligned}
P_{out}(\gamma_{th}) = {} & \prod_{j=1}^{N} \sum_{\rho=0}^{\infty} \binom{\alpha_{S\mathscr{H}_j}}{\rho} (-1)^{\rho} \exp\left(-\rho \left(\frac{\gamma_{th}}{(\eta_{S\mathscr{H}_j} I^{a}_{S\mathscr{H}_j})^{2} (\frac{P_S}{N_0})} \right)^{\frac{\beta_{S\mathscr{H}_j}}{2}} \right) + \left[\sum_{p=0}^{\infty} \binom{\alpha_{\mathscr{H}_J G}}{p} \right. \\
& \times (-1)^{p} \exp\left(-p \left(\frac{\gamma_{th}}{(\eta_{\mathscr{H}_J G} I^{a}_{\mathscr{H}_J G})^{2} (\frac{P_{\mathscr{H}_J}}{N_0})} \right)^{\frac{\beta_{\mathscr{H}_J G}}{2}} \right) \left(1 - \sum_{l=0}^{m-1} \sum_{q=0}^{l} \frac{\mu (1-m)_{l} . (-\delta)^{l}}{q! \vartheta^{l-q+1} (\frac{P_{\mathscr{H}_J} \mathscr{F}_{\mathscr{H}_J G}}{N_0})^{l+1} l!} \right. \\
& \left. \left. \times \gamma_{th}^{q} \exp(-\vartheta \gamma_{th}) \right) \right] - \left[\prod_{j=1}^{N} \sum_{\rho=0}^{\infty} \binom{\alpha_{S\mathscr{H}_j}}{\rho} (-1)^{\rho} \exp\left(-\rho \left(\frac{\gamma_{th}}{(\eta_{S\mathscr{H}_j} I^{a}_{S\mathscr{H}_j})^{2} (\frac{P_S}{N_0})} \right)^{\frac{\beta_{S\mathscr{H}_j}}{2}} \right) \right. \\
& \times \left(1 - \sum_{l=0}^{m-1} \sum_{q=0}^{l} \frac{\mu (1-m)_{l} . (-\delta)^{l}}{q! \vartheta^{l-q+1} (\frac{P_{\mathscr{H}_J} \mathscr{F}_{\mathscr{H}_J G}}{N_0})^{l+1} l!} \gamma_{th}^{q} \exp(-\vartheta \gamma_{th}) \right) \times \sum_{p=0}^{\infty} \binom{\alpha_{\mathscr{H}_J G}}{p} (-1)^{p} \\
& \left. \times \exp\left(-p \left(\frac{\gamma_{th}}{(\eta_{\mathscr{H}_J G} I^{a}_{\mathscr{H}_J G})^{2} (\frac{P_{\mathscr{H}_J}}{N_0})} \right)^{\frac{\beta_{\mathscr{H}_J G}}{2}} \right) \right] . \qquad (3.35)
\end{aligned}
$$

as

$$
\begin{aligned}
P^{\infty}_{\text{out}} &= F^{\infty}_{\gamma_{S\mathscr{H}_J}}(\gamma_{th}) + F^{\infty}_{\gamma^{FSO}_{\mathscr{H}_J G}}(\gamma_{th}) F^{\infty}_{\gamma^{RF}_{\mathscr{H}_J G}}(\gamma_{th}) \\
&\quad - F^{\infty}_{\gamma_{S\mathscr{H}_J}}(\gamma_{th}) F^{\infty}_{\gamma^{FSO}_{\mathscr{H}_J G}}(\gamma_{th}) F^{\infty}_{\gamma^{RF}_{\mathscr{H}_J G}}(\gamma_{th}) \\
&\approx F^{\infty}_{\gamma_{S\mathscr{H}_J}}(\gamma_{th}) + F^{\infty}_{\gamma^{FSO}_{\mathscr{H}_J G}}(\gamma_{th}) F^{\infty}_{\gamma^{RF}_{\mathscr{H}_J G}}(\gamma_{th}). \qquad (3.36)
\end{aligned}
$$

The negative term in (3.36) is neglected as its value is very small compared to the sum of the other terms. By using the Taylor series approximation of $\exp(-x/a) \simeq 1 - x/a$, and after few manipulations, $F^{\infty}_{\gamma_{S\mathscr{H}_J}}(\gamma_{th})$ can be written as

$$
F^{\infty}_{\gamma_{S\mathscr{H}_J}}(\gamma_{th}) = \prod_{j=1}^{N} \left[\left(\frac{\gamma_{th}}{(\eta_{S\mathscr{H}_j} I^{a}_{S\mathscr{H}_j})^{2} \overline{\gamma}_{S\mathscr{H}_j}} \right)^{\frac{\alpha_{S\mathscr{H}_j} \beta_{S\mathscr{H}_j}}{2}} \right] . \qquad (3.37)
$$

Note that in $\mathscr{H}_J$ to G FSO communication, $F^{\infty}_{\gamma^{FSO}_{\mathscr{H}_J G}}(\gamma_{th})$ can be obtained similarly as in (3.37) after changing the subscripts as $F^{\infty}_{\gamma^{FSO}_{\mathscr{H}_J G}}(\gamma_{th}) = \left(\frac{\gamma_{th}}{(\eta_{\mathscr{H}_J G} I^{a}_{\mathscr{H}_J G})^{2} \overline{\gamma}^{FSO}_{\mathscr{H}_J G}} \right)^{\frac{\alpha_{\mathscr{H}_J G} \beta_{\mathscr{H}_J G}}{2}}$. On the contrary, for $\mathscr{H}_J$ to G RF communication, we obtain $F^{\infty}_{\gamma^{RF}_{\mathscr{H}_J G}}(\gamma_{th})$ by applying Maclaurin series expansion [58] for the exponential function. Thereafter, by considering only the first term as the higher-order terms are negligible, $F^{\infty}_{\gamma^{RF}_{\mathscr{H}_J G}}(\gamma_{th})$ can be written as

$$F^{\infty}_{\gamma^{RF}_{\mathscr{H}_J G}}(\gamma_{th}) \simeq \mu \gamma_{th} \frac{1}{\overline{\gamma}^{RF}_{\mathscr{H}_J G}}. \tag{3.38}$$

Furthermore, at high SNR values, the OP can be written as $P^{\infty}_{\text{out}} = k(\overline{\gamma})^{-\mathscr{G}_d}$, where k is a constant variable, which defines the coding gain of the system. The diversity order $\mathscr{G}_d$ defines the slope of the OP curve. In the case when the average SNRs of all links tend to infinity, the diversity gain is obtained as $\mathscr{G}_d = \min\left(N\frac{\alpha_{S\mathscr{H}_j}\beta_{S\mathscr{H}_j}}{2}, \max(\frac{\alpha_{\mathscr{H}_J G}\beta_{\mathscr{H}_J G}}{2}, 1)\right)$. Finally, the asymptotic OP P^{∞}_{out} can be easily obtained.

3.4 Numerical Results

In this section, we first validate the theoretical results with the MC simulations. Then, we evaluate the OP of our system model under different weather conditions. In the simulations, the effects of aperture averaging, pointing errors, wind speed, and different levels of thermal noise are investigated in terms of OP. Furthermore, we assume that all HAPS systems experience the same atmospheric conditions without losing the generality and we assume equal transmit power at S and $\mathscr{H}_j$. The fading severity parameters for the RF link, which is modeled as a shadowed-Rician fading channel, are simulated depending on different shadowing severity levels as given in [59]. In addition, the following rain rate parameters are set: light rain ($\mathscr{R}$ =2.5 mm/h), moderate rain ($\mathscr{R}$ = 12.5 mm/h), and heavy rain ($\mathscr{R}$ = 25 mm/h) [23]. Moreover, for the FSO link between $\mathscr{H}_J$ and G in the absence of aperture averaging, the atmospheric turbulence parameters are set to ($\alpha_{\mathscr{H}_J G} = 3.3419$, $\beta_{\mathscr{H}_J G} = 2.3131$, $\eta_{\mathscr{H}_J G} = 0.78693$) for $u_{\mathscr{H}_J G} = 21$ m/s, whereas the stratospheric turbulence parameters are set to ($\alpha_{S\mathscr{H}_j} = 1.5825$, $\beta_{S\mathscr{H}_j} = 8.9870$, $\eta_{S\mathscr{H}_j} = 1.0025$) for $u_{S\mathscr{H}_j} = 65$ m/s. In all simulations, we assume the sky to be homogeneous and the atmospheric attenuation to change in function of altitude. Finally, the OP is plotted relative to the transmit power at a threshold $\gamma_{th} = 7$ dB. Table 3.5 provides the simulation parameters used in the numerical results section.

3.4.1 Verification of the theoretical expressions

In Figure 3.2, we have compared the outage performance of the proposed scheme with the single-hop FSO, single-hop RF, single-hop hybrid RF/FSO, HAPS-aided FSO, and

Table 3.5 : Parameters of FSO and RF links.

Satellite-HAPS (FSO)	
Parameter	Value
Zenith angle ($\xi_{S\mathcal{H}_j}$)	65°
Wind speed ($u_{S\mathcal{H}_j}$)	65 m/s
Optical wavelength (λ_{FSO})	1550 nm
Temperature (T)	-55 °C
Noise figure (n_f)	1 dB
Satellite height (h_S)	500 km
HAPS altitude ($h_{\mathcal{H}}$)	19 km
Stratospheric attenuation (Ψ)	2.15×10^{-1}
Bandwidth (B)	0.5 GHz
Nominal value (C_0)	10^{-18}
HAPS-GS (FSO)	
Zenith angle ($\xi_{\mathcal{H}_jG}$)	20°
Wind speed ($u_{\mathcal{H}_jG}$)	21 m/s
Optical wavelength (λ_{FSO})	1550 nm
Elevation above sea level (h_E)	0.8 km
Nominal value (C_0)	1.7×10^{-14}
HAPS-GS (RF)	
RF wavelength (λ_{RF})	40 GHz
Transmitter gain (G_T)	45 dB
Receiver gain (G_R)	45 dB
Polarization tilt angle (ι)	45°
Oxygen scattering (φ_{oxy})	0.1 dB/km [66]
Common parameters for HAPS-GS RF and FSO	
Bandwidth (B)	0.5 GHz
Temperature (T)	18 °C
Noise figure (n_f)	1 dB
Threshold (γ_{th})	7 dB

HAPS-aided RF systems with respect to the transmit power and assuming the same atmospheric conditions. It is clear from the plots that the outage performance of the proposed scheme is better than all other systems. In addition, the figure shows that single-hop hybrid RF/FSO performs better than single-hop RF and single-hop FSO, and this gain is obtained from hybrid communication. It is also inferred from the figure that using a HAPS as the relay node improves the overall communication. This is due to the fact that the FSO link from the satellite to the HAPS node is less vulnerable to atmospheric attenuation. Also, for single-hop RF communication, the simulation results have shown that the outage performance is highly degraded by oxygen attenuation due to the large distance between the satellite and the GS. Furthermore, we observe a validation of the theoretical results with the MC simulations, which

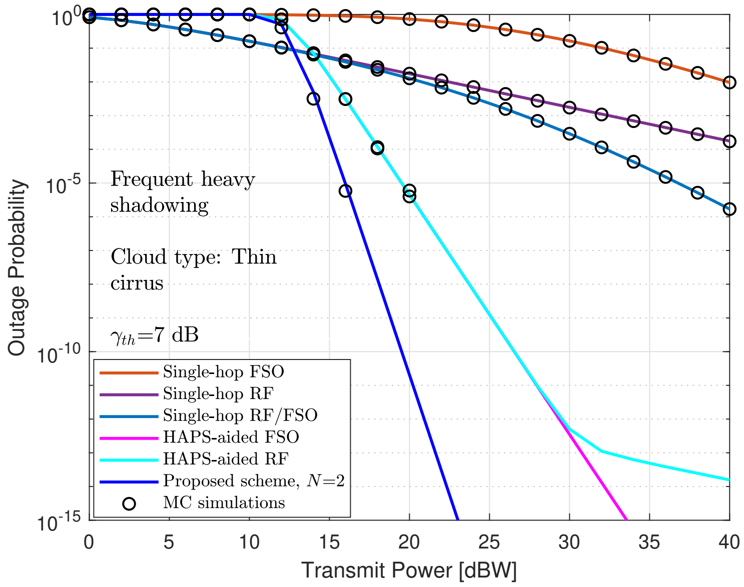

Figure 3.2 : OP performance of different system models under clear weather conditions.

justifies the correctness of our derivations. Finally, it is clear from the figure that the OP decreases when the transmit power increases.

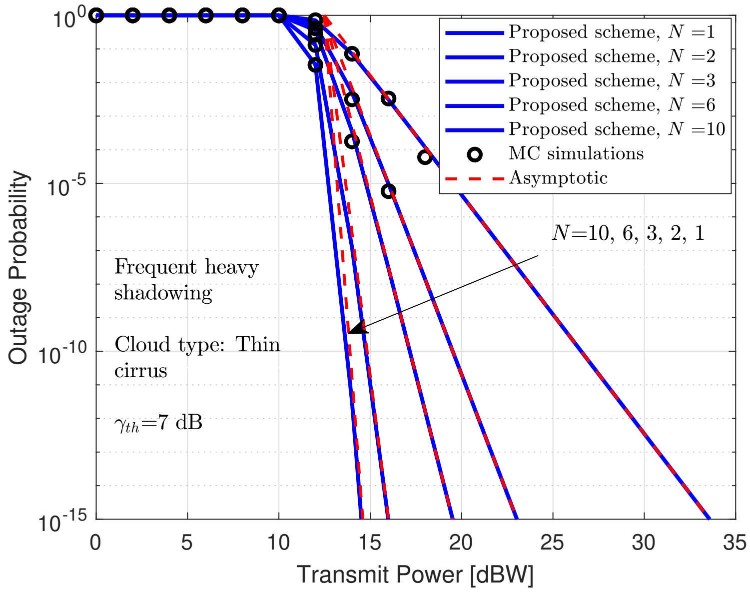

Figure 3.3 : Impact of the HAPS selection scheme on the proposed model in terms of OP.

Figure 3.3 depicts the OP performance for several HAPS nodes in clear weather conditions. As we can see from the figure, increasing N improves the overall performance. At an outage of 10^{-5}, we can observe a gain of 5 dB between the curves of $N = 10$ and $N = 1$. Thus, the proposed HAPS selection scheme significantly improves dual-hop HAPS-aided communication. Furthermore, the theoretical results are validated with the MC simulations for a different number of HAPS systems. In addition, the figure shows that the asymptotic OP curves almost match the exact OP curves for the high SNR region, which validates the obtained derivations.

3.4.2 Impact of aperture averaging

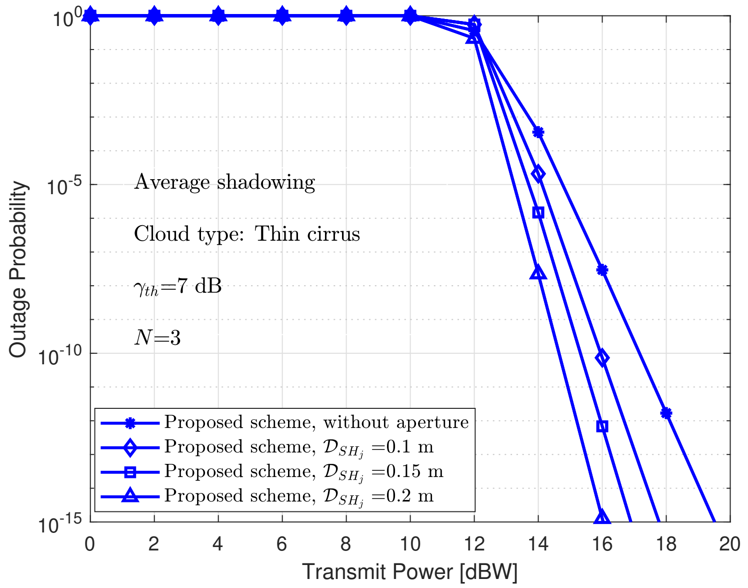

Figure 3.4 : OP performance for various aperture sizes.

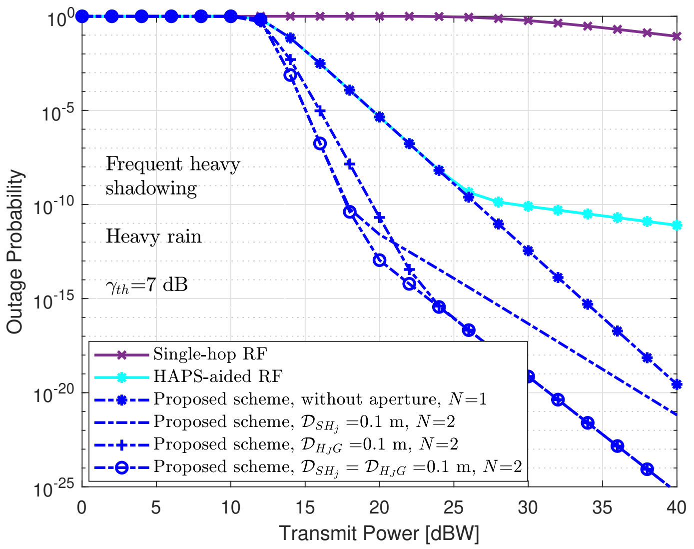

Figure 3.5 : OP performance for various aperture sizes under heavy rain weather.

In this subsection, we analyze the effect of aperture averaging technique on the proposed model in terms of OP.

In Figure 3.4, we compared the performance of the proposed setup for different aperture sizes for S to $\mathscr{H}_j$ communication under clear weather conditions for $N = 3$ HAPS nodes. As the figure indicates, the use of greater aperture sizes increases the gain in terms of transmit power and improves the overall performance by reducing the effect of turbulence-induced fading. This is because, with an increase in the aperture size, more energy is collected by the receiver beam increases and thus offers more power gain. Similarly, Figure 3.5 compares the outage performance of the proposed model for different aperture sizes in the presence of heavy rain weather. As we can see from the figure, the single-hop RF system is highly degraded by heavy rain conditions and a significant improvement is observed with the use of the HAPS node. Also, it is noticed that hybrid RF/FSO without aperture averaging and with $N = 1$ shows better performance than HAPS-aided RF. Thus, the use of the FSO backup link helps in enhancing the outage performance in the presence of heavy rain. For our proposed model, we compared the use of the aperture averaging technique when it is used only at $\mathscr{H}_J$, G, or both of them at the same time. It is inferred from the figure that considering aperture for S to $\mathscr{H}_j$ communication improves the outage performance only at low transmit power, whereas, assuming the aperture averaging for $\mathscr{H}_J$ to G communication shows better performance at high transmit power. Finally, as expected, using the aperture averaging technique at both hops highly increases the performance gain.

3.4.3 Impact of weather conditions

In Figure 3.6, we observe the outage performance of the proposed scheme for different rain levels for $N = 3$, while considering the aperture averaging technique. As expected, increasing the rain rate, deteriorates the overall performance as the attenuation level increases. Also, we can see that decreasing the severity of fading for the RF link, improves the outage performance for heavy rain. Moreover, the figure shows better performance when using the aperture averaging technique at both hops for moderate rain state. Finally, the simulation results show that RF communication is highly affected by rain and that the hybrid communication relies on the FSO link under rainy conditions.

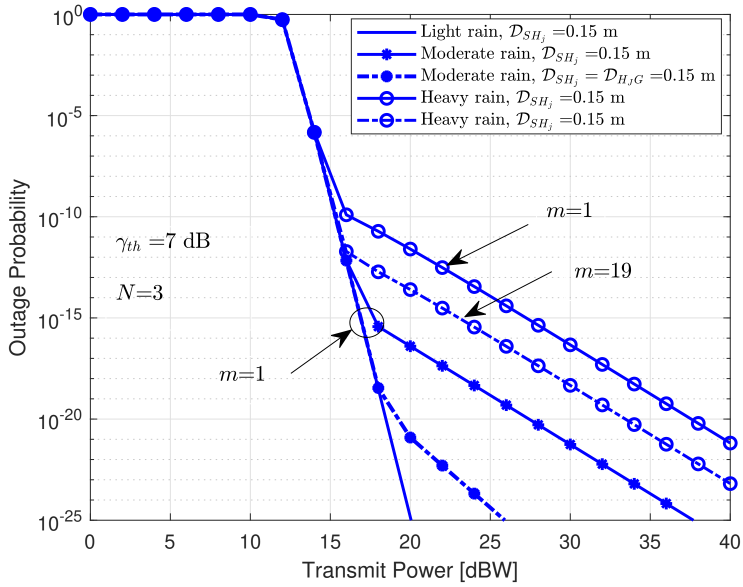

Figure 3.6 : OP performance under rainy weather conditions.

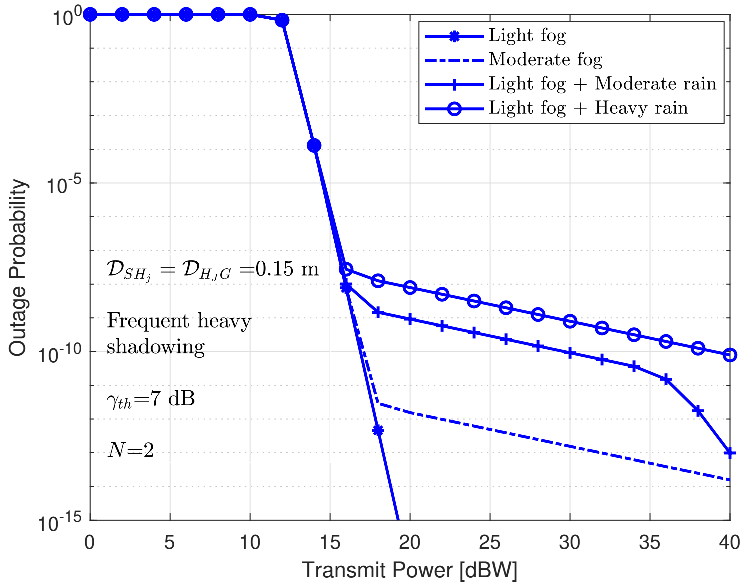

Figure 3.7 : OP performance under rainy and foggy weather conditions.

Figure 3.7 shows the impact of foggy and rainy weather on the performance of the system for $N = 2$ and considering an aperture size of $\mathscr{D}_{S\mathscr{H}_j} = \mathscr{D}_{\mathscr{H}_jG} = 0.15$ m. We first consider light fog, which can be present up to 100 m above ground level. Then, increasing the thickness of the fog layer from light to moderate deteriorates the performance of the FSO communication as shown in the figure and the RF link becomes dominant for hybrid communications. Furthermore, in the presence of light fog with all rain levels, the overall performance is degraded as both links are affected, however, the use of the aperture averaging at both hops helps to mitigate these effects.

3.4.4 Impact of pointing errors

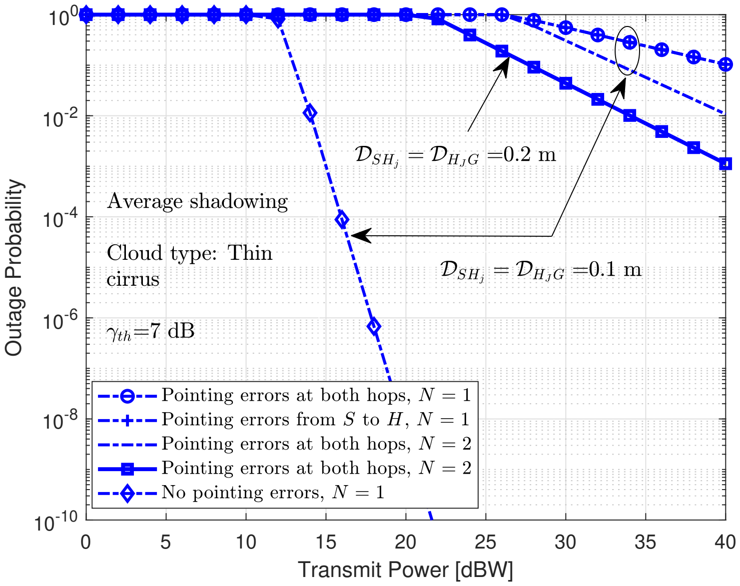

Figure 3.8 : The impact of pointing errors on the proposed model in terms of OP.

In Figure 3.8, we study the impact of zero boresight pointing errors on the proposed model. It is observed from the figure that severe deterioration occurs in the outage performance due to the pointing errors phenomenon. In addition, the simulation results reveal that no improvement is noticed in the presence of pointing errors only for S to $\mathscr{H}_j$ communication and this is due to the fact that the link from S to $\mathscr{H}_j$ suffers from serious deterioration. Thus, it can be noted that the overall performance is degraded because of the misalignment between the transmitter and receiver. However, we can see that increasing the aperture size and employing HAPS selection can help us to alleviate this deterioration.

3.4.5 Impact of wind speed

We also investigate the outage performance for different wind speed levels at the GS for $N = 1$ and for $\mathscr{D}_{S\mathscr{H}_j} = 0.1$ m. For low, moderate, and strong wind speed, $u_{\mathscr{H}_jG}$ is set to $u_{\mathscr{H}_jG} = 10$ m/s, $u_{\mathscr{H}_jG} = 21$ m/s, and $u_{\mathscr{H}_jG} = 30$ m/s, respectively for the FSO link between HAPS and GS. As we see in Figure 3.9, increasing the wind velocity deteriorates the overall outage performance. This is due to the fact that increasing

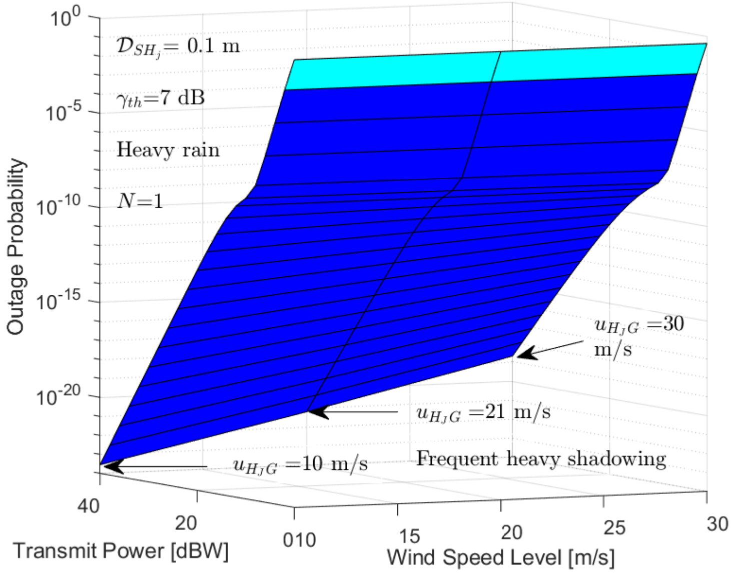

Figure 3.9 : OP performance for different wind speed levels.

the wind speed level leads to a displacement of the beamsx and as the wind speed is directly related to the scintillation index, it causes greater atmospheric turbulence. Furthermore, at a lower wind speed $u_{\mathscr{H}_J G} = 10$ m/s, we can see a significant power gain compared to $u_{\mathscr{H}_J G} = 30$ m/s.

3.4.6 Design guidelines

To summarize, we propose guidelines for the design of HAPS-assisted SatCom downlink systems.

- The proposed hybrid RF/FSO model shows better performance than single-hop FSO and RF, single-hop hybrid RF/FSO, HAPS-aided RF, and HAPS-aided FSO in terms of OP in clear weather conditions.
- The use of HAPS improves SatCom's performance as the link from satellite to HAPS is less affected by atmospheric turbulence and attenuation.
- The simulations have shown that the FSO channel is slightly affected by rainy weather, whereas the RF link is highly affected, although it remains available. Moreover, in the presence of foggy weather, FSO communication deteriorates.
- Aperture averaging should be considered as it can mitigate the effect of turbulence-induced fading and improve performance, especially for higher aperture

diameter values. Also, it was inferred from the simulation results that using aperture averaging at the HAPS node improves the OP at low transmit power, whereas using aperture averaging at the GS station shows enhanced performance at high transmit power.

- The misalignment between the transmitter and the receiver caused by pointing errors substantially degrades the overall outage performance.
- By increasing the aperture averaging size, a significant performance improvement in terms of power gain can be obtained.
- The zenith angle is directly related to the performance of downlink SatCom. In fact, for lower zenith angle values, we observe lower atmospheric attenuation and this can enhance the overall performance.
- The HAPS selection based on the satellite-HAPS channel quality improves the overall performance.

3.5 Summary and Discussion

In this chapter, we proposed a new HAPS-assisted downlink SatCom model with hybrid RF/FSO communication for unicast communication. More precisely, in the first phase of transmission, the best HAPS node was selected among multiple HAPS nodes, and then in the second phase, we focused on the simultaneous transmission on both RF and FSO links. For the proposed model, the OP expressions were derived, along with OP analysis at high SNR, and MC simulations were provided to validate the accuracy of our analytical results. Furthermore, we considered different weather conditions and investigated the impact of pointing errors, temperature, aperture averaging technique, and wind speed. The simulations indicated that zero-boresight pointing errors lead to severe performance impairments and that aperture averaging can mitigate the effects of turbulence-induced fading and misalignment caused by pointing errors. Moreover, the HAPS selection based on the satellite-HAPS channel was shown to enhance the overall performance. Finally, guidelines were provided for the design of a HAPS-aided SatCom system.

In the following chapter, we are interested in investigating the physical performance of mixed RF-FSO communication for multicast services in future networks.

4. HAPS-ASSISTED HYBRID RF-FSO MULTICAST COMMUNICATIONS: ERROR AND OUTAGE ANALYSIS

In the previous chapters, we studied the outage performance of hybrid RF/FSO in future NTN systems by proposing two different system models for unicast services. Different from the prior works and the current literature, in this chapter, we study the physical performance of RF and FSO channels for multicast communication. Specifically, we address the mixed RF-FSO communication for multicast services in NTN systems in order to improve the spectral efficiency by serving a large number of users at the same time. In this context, we propose two different scenarios, namely HAPS-aided mixed RF/FSO/RF and satellite-aided mixed RF/FSO/FSO/RF communications.

As mentioned previously, this work has been presented in the following journal paper:

O. Ben Yahia, E. Erdogan, G. Karabulut Kurt, “HAPS-assisted Hybrid RF-FSO Multicast Communications: Error and Outage Analysis”, IEEE Transactions on Aerospace and Electronic Systems (early access), pp. 1-13, 2022.

The rest of the chapter is organized as follows: In Section 4.1 the signals and system model are presented. The performance analysis of the system is provided in Section 4.2. Numerical results are provided and analyzed in Section 4.3. Finally, the conclusion is drawn in Section 4.4.

4.1 Signals and System Model

In this section, we illustrate the proposed system model of downlink communication for multicast protocol [67]. As shown in Figure 4.1, we consider two use-cases: s_1 named HAPS-aided mixed RF/FSO/RF communication and s_2 entitled satellite-aided mixed RF/FSO/FSO/RF communication for multicast clustering. In both cases, we assume the presence of a ground transmitter G that intends to send its information to a set of N ground destinations $D = \{D_1, D_2, ..., D_N\}$ registered under the same multicast address and distributed randomly at hundreds of kilometers far from each

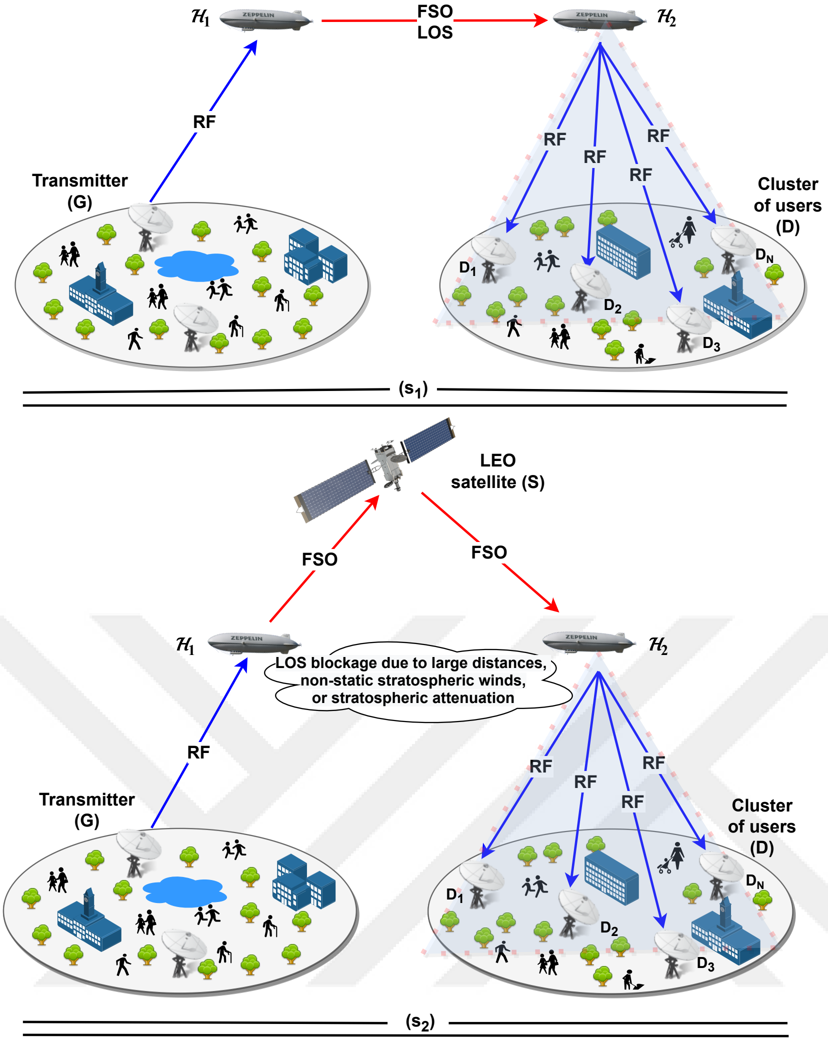

Figure 4.1 : Illustration of the proposed system models.

other and connected between them. More precisely, in the first use-case (s_1), the transmission is completed through two HAPS nodes $\mathscr{H}_1$ and $\mathscr{H}_2$ by using optical communication as perfect LOS is established between them. In the second use-case (s_2), the LOS connectivity can not be formed between $\mathscr{H}_1$ and $\mathscr{H}_2$ due to the large distance, non-static stratospheric winds, or stratospheric attenuation. Thereby, an LEO satellite-aided optical cooperation is created over three network layers. In particular, G transmits its message to the multicast group in four-time slots over $\mathscr{H}_1$, the LEO satellite S, and $\mathscr{H}_2$, all working based on DF relaying protocol. DF relaying mode is chosen as it eliminates noise at the relay and the relay can perform perfect detection. In addition, owing to the ease of implementation, DF is frequently used by the researchers.

The OP in a conventional multicast network (CVM) is defined in terms of the user with the lowest signal-to-noise ratio (minSNR). While the minSNR policy ensures that all users in a group have the same data rate, it has been shown to be inefficient, especially when a minimum rate or assured quality of service and error-free decoding are required. Specifically, the minSNR technique in CVM clearly allows all users in the group to receive the transmitted data; nevertheless, because it is unable to use multi-user channel diversities to increase network performance, it quickly leads to system saturation [68]. So far, there has not been an easy way to use the minSNR strategy in CVM to increase system performance without adding complexity to the optimization process. As a result, we suggest two-phase communication-based cooperative multicast transmission to maximize the system's diversity [69]. We also assume that all ground receivers are connected via a terrestrial network. Based on the feedback channel state information (CSI) from the users to $\mathscr{H}_2$, the HAPS node $\mathscr{H}_2$ sends the signal to the user with the best channel characteristics. Finally, the selected user will multicast the data to the users which have worse channel characteristics using the terrestrial network. In both scenarios, G to $\mathscr{H}_1$ uplink and $\mathscr{H}_2$ to D downlink communications are conducted through RF links that experience the shadowed-Rician fading, which is very convenient for modeling SatCom links. The FSO links on the other hand follow the EW fading. EW fading has been found to be the best fit for various aperture sizes for different weather conditions, particularly when aperture averaging is considered to reduce the effects of turbulence and improve the overall performance [19]. In addition, we assume that for all FSO links IM/DD is employed owing to its low cost and simplicity. Moreover, we assume that $\mathscr{H}_2$ is deploying a multi-beam antenna, which makes it able to project multiple spot beams within its potential footprint. Finally, in the proposed architectures, all links are independent and identically distributed.

4.1.1 HAPS-aided mixed RF/FSO/RF communication

4.1.1.1 Ground-to-HAPS communication

In the first hop, we assume that RF communication is used due to the destructive effects of aerosols, gases, and atmospheric conditions that highly affect the performance of FSO communication. Thereby, in the first stage of communication, the received signal at $\mathscr{H}_1$ can be given as

$$y_{\mathscr{H}_1} = \sqrt{P_G \mathscr{F}_{\mathscr{H}_1}} h_{G,\mathscr{H}_1} x_G + n_{\mathscr{H}_1}, \tag{4.1}$$

where P_G denotes the transmit power of G, $\mathscr{F}_{\mathscr{H}_1}$ indicates the path loss, $h_{G,\mathscr{H}_1}$ is the channel coefficient between G and $\mathscr{H}_1$, x_G represents the transmitted symbol with $\mathbb{E}\left\{|x_G|^2\right\} = 1$, with $\mathbb{E}\{\cdot\}$ is the statistical expectation operator, and $n_{\mathscr{H}_1}$ is the zero-mean complex Gaussian noise at $\mathscr{H}_1$ with noise power spectral density (PSD) N_0. Based on (4.1), the instantaneous SNR at $\mathscr{H}_1$ can be written as

$$\gamma_{G,\mathscr{H}_1} = \frac{P_G \mathscr{F}_{\mathscr{H}_1}}{N_0} |h_{G,\mathscr{H}_1}|^2 = \overline{\gamma}_{G,\mathscr{H}_1} |h_{G,\mathscr{H}_1}|^2, \tag{4.2}$$

where $\overline{\gamma}_{G,\mathscr{H}_1} = \frac{P_G \mathscr{F}_{\mathscr{H}_1}}{N_0}$ is the average SNR of the RF link. Furthermore, the path loss of the RF communication can be given as $\mathscr{F}_{\mathscr{H}_1}[dB] = G_T + G_R - L_F - L_R - L_A$ [33], where G_T, G_R denote the transmit and the receiver antenna gains respectively, L_F indicates the free space path loss given as $L_F = 92.45 + 20\log f_r + 20\log L_{G,\mathscr{H}_1}$, f_r represents the frequency in GHz, $L_{G,\mathscr{H}_1}$ represents the propagation distance from G to $\mathscr{H}_1$, L_R indicates the attenuation due to rain in dB/km, and L_A is the gaseous atmosphere loss.

In this work, as we consider shadowed-Rician distribution, the PDF of the instantaneous SNR $\gamma_{G,\mathscr{H}_1}$ can be written as [59]

$$f_{\gamma_{G,\mathscr{H}_1}}(\gamma) = \sum_{j=0}^{m_{\mathscr{H}_1}-1} \frac{\vartheta_{\mathscr{H}_1}(1-m_{\mathscr{H}_1})_j.(-\delta_{\mathscr{H}_1})^j}{\overline{\gamma}_{G,\mathscr{H}_1}^{j+1}.(j!)^2} \gamma^j \exp(-\psi_{\mathscr{H}_1}\gamma), \tag{4.3}$$

where $m_{\mathscr{H}_1}$ denoting the Nakagami-m fading severity parameter of the corresponding channel, $\vartheta_{G,\mathscr{H}_1} = \frac{1}{2b_{\mathscr{H}_1}}(\frac{2b_{\mathscr{H}_1} m_{\mathscr{H}_1}}{2b_{\mathscr{H}_1} m_{\mathscr{H}_1} + \Omega_{\mathscr{H}_1}})^{m_{\mathscr{H}_1}}$ with $2b_{\mathscr{H}_1}$ is the average power of the non-LOS (NLOS) component and $\Omega_{\mathscr{H}_1}$ represents the average power of LOS component. $\psi_{\mathscr{H}_1} = \frac{\varsigma_{\mathscr{H}_1} - \delta_{G,\mathscr{H}_1}}{\overline{\gamma}_{G,\mathscr{H}_1}}$, $\varsigma_{\mathscr{H}_1} = \frac{1}{2b_{\mathscr{H}_1}}$, $\delta_{\mathscr{H}_1} = \frac{\Omega_{\mathscr{H}_1}}{2b_{\mathscr{H}_1}(2b_{\mathscr{H}_1} m_{\mathscr{H}_1} + \Omega_{\mathscr{H}_1})}$, and $(\cdot)_j$ is the Pochhammer symbol. In this regard, the CDF of $\gamma_{G,\mathscr{H}_1}$ is given by

$$F_{\gamma_{G,\mathscr{H}_1}}(\gamma) = 1 - \sum_{l=0}^{m_{\mathscr{H}_1}-1} \sum_{q=0}^{l} \frac{\vartheta_{\mathscr{H}_1}(1-m_{\mathscr{H}})_l.(-\delta_{\mathscr{H}_1})^l}{q!(\psi_{\mathscr{H}_1})^{l-q+1}(\overline{\gamma}_{G,\mathscr{H}_1})^{l+1} l!} (\gamma)^q \exp(-\psi_{\mathscr{H}_1}\gamma). \tag{4.4}$$

4.1.1.2 Inter-HAPS communication

Herein, we use FSO communication as LOS conditions can be perfectly satisfied as the HAPS systems are quasi-stationary. Therefore, tracking and pointing issues can be ignored for this communication model, consistent with the assumptions in the current literature [31,33,60]. In the second phase of communication, the received signal at $\mathscr{H}_2$ can be given as [10]

$$y_{\mathscr{H}_2} = \sqrt{\zeta P_{\mathscr{H}_1}} I_{\mathscr{H}_1,\mathscr{H}_2} x_{\mathscr{H}_1} + n_{\mathscr{H}_2}, \tag{4.5}$$

where ζ indicates the electrical-to-optical conversion coefficient, $P_{\mathscr{H}_1}$ is the average transmitted optical power of $\mathscr{H}_1$, $x_{\mathscr{H}_1}$ is the transmitted signal of $\mathscr{H}_1$, and $I_{\mathscr{H}_1,\mathscr{H}_2} > 0$ represents the received fading gain (irradiance) between the laser of $\mathscr{H}_1$ and the photodetector of $\mathscr{H}_2$ through the optical link. Finally, $n_{\mathscr{H}_2}$ is the is the zero-mean complex Gaussian noise at $\mathscr{H}_2$ with noise PSD N_0. Thus, the instantaneous SNR at $\mathscr{H}_2$ can be written as

$$\gamma_{\mathscr{H}_1,\mathscr{H}_2} = \frac{\zeta P_{\mathscr{H}_1} I^2_{\mathscr{H}_1,\mathscr{H}_2}}{N_0} = \overline{\gamma}_{\mathscr{H}_1,\mathscr{H}_2} I^2_{\mathscr{H}_1,\mathscr{H}_2}, \tag{4.6}$$

where $\overline{\gamma}_{\mathscr{H}_1,\mathscr{H}_2}$ indicates the average SNR. In FSO communication, the channel gain is considered as a composite optical channel as $I_{\mathscr{H}_1,\mathscr{H}_2} = I^a_{\mathscr{H}_1,\mathscr{H}_2} I^t_{\mathscr{H}_1,\mathscr{H}_2}$, where $I^a_{\mathscr{H}_1,\mathscr{H}_2}$ defines the stratospheric attenuation and $I^t_{\mathscr{H}_1,\mathscr{H}_2}$ models the stratospheric turbulence using the EW fading distribution. Thus, the PDF of $I^t_{\mathscr{H}_1,\mathscr{H}_2}$ can be given as

$$\begin{aligned} f_{I^t_{\mathscr{H}_1,\mathscr{H}_2}}(I) = {} & \frac{\alpha_{\mathscr{H}_1,\mathscr{H}_2} \beta_{\mathscr{H}_1,\mathscr{H}_2}}{\eta_{\mathscr{H}_1,\mathscr{H}_2}} \left(\frac{I}{\eta_{\mathscr{H}_1,\mathscr{H}_2}} \right)^{\beta_{\mathscr{H}_1,\mathscr{H}_2}-1} \exp\left[-\left(\frac{I}{\eta_{\mathscr{H}_1,\mathscr{H}_2}} \right)^{\beta_{\mathscr{H}_1,\mathscr{H}_2}} \right] \\ & \times \left(1 - \exp\left[-\left(\frac{I}{\eta_{\mathscr{H}_1,\mathscr{H}_2}} \right)^{\beta_{\mathscr{H}_1,\mathscr{H}_2}} \right] \right)^{\alpha_{\mathscr{H}_1,\mathscr{H}_2}-1}, \end{aligned} \tag{4.7}$$

where $\eta_{\mathscr{H}_1,\mathscr{H}_2}$ is the scale parameter, and $\alpha_{\mathscr{H}_1,\mathscr{H}_2}$, $\beta_{\mathscr{H}_1,\mathscr{H}_2}$ denote the shape parameters which are directly related to the scintillation index. These parameters can be expressed as [60, Eq. (5)]. Furthermore, the scintillation index for the horizontal communication can be written as [13, Sect. (5)]

$$\sigma^2_{I_{\mathscr{H}_1,\mathscr{H}_2}} = 1.23 C_n^2 K^{7/6} L^{11/7}_{\mathscr{H}_1,\mathscr{H}_2}. \tag{4.8}$$

In the above equation, C_n^2 indicates the refractive index structure parameter [13, Sect. (5)], $K = \frac{2\pi}{\lambda}$ is the optical wave number, λ is the optical wavelength, and $L_{\mathscr{H}_1,\mathscr{H}_2}$ represents the propagation distance between $\mathscr{H}_1$ and $\mathscr{H}_2$. According to [70], the communication between two HAPS systems at an altitude of 20 km, is feasible up to 600 km. Herein, it is worth mentioning that the LOS distance might be slightly different from the distance when projecting the HAPS systems on the Earth, due to the curvature nature of the Earth. For inter-HAPS communication, we consider the effect of stratospheric attenuation [7]. The stratospheric attenuation can be modeled based on the Beer-Lambert law as $I^{a}_{\mathscr{H}_1,\mathscr{H}_2} = \exp(-\phi L_{\mathscr{H}_1,\mathscr{H}_2})$, where ϕ denotes the stratospheric attenuation coefficient [7].

4.1.1.3 HAPS-to-ground communication

In the $\mathscr{H}_2$ to D multicast communication, the optical signal received at $\mathscr{H}_2$ is first decoded then converted into digital RF signal and forwarded to D. Therefore, the received signal at the i-th receiver D_i providing the best channel characteristics can be expressed as

$$y_{D_i} = \sqrt{P_{\mathscr{H}_2}\mathscr{F}_{D_i}}h_{\mathscr{H}_2,D_i}x_{\mathscr{H}_2} + n_{D_i}, \tag{4.9}$$

where $P_{\mathscr{H}_2}$ represents the transmit power of $\mathscr{H}_2$, $\mathscr{F}_{D_i}$ indicates the path loss, $h_{\mathscr{H}_2,D_i}$ defines the channel information, $x_{\mathscr{H}_2}$ is the transmitted signal from $\mathscr{H}_2$, and n_{D_i} is the Gaussian noise with N_0 noise PSD. Accordingly, the instantaneous SNR at the multicast destination can be written as

$$\gamma_{\mathscr{H}_2,D} = \max(\gamma_{\mathscr{H}_2,D_1}, \gamma_{\mathscr{H}_2,D_2}, \ldots, \gamma_{\mathscr{H}_2,D_N}). \tag{4.10}$$

Thus the CDF of $\gamma_{\mathscr{H}_2,D}$ becomes

$$F_{\gamma_{\mathscr{H}_2,D}}(\gamma) = \prod_{i=1}^{N}\left(1 - \sum_{p=0}^{m_{D_i}-1}\sum_{k=0}^{p}\frac{\vartheta_{D_i}(1-m_{D_i})_p.(-\delta_{D_i})^p}{k!(\psi_{D_i})^{p-k+1}(\overline{\gamma}_{\mathscr{H}_2,D_i})^{p+1}p!}(\gamma)^k\exp(-\psi_{D_i}\gamma)\right), \tag{4.11}$$

Finally, the end-to-end instantaneous SNR for s_1 can be obtained as

$$\gamma_0^{s_1} = \min\left\{\gamma_{G,\mathscr{H}_1};\gamma_{\mathscr{H}_1,\mathscr{H}_2};\gamma_{\mathscr{H}_2,D}\right\}. \tag{4.12}$$

4.1.2 Satellite-aided mixed RF/FSO/FSO/RF communication

In this subsection, we present the satellite-aided mixed RF/FSO/FSO/RF communication. The G to $\mathscr{H}_1$ and $\mathscr{H}_2$ to D communications were presented in the above section. Thereby, we omit these sections to prevent duplication.

4.1.2.1 HAPS-to-satellite communication

In the $\mathscr{H}_1$ to S communication, the received signal can be expressed very similar to (4.5) as $y_S = \sqrt{\zeta P_{\mathscr{H}_1}} I_{\mathscr{H}_1,S} x_{\mathscr{H}_1} + n_S$, where $I_{\mathscr{H}_1,S}$ indicates the turbulence induced fading at S. The received SNR at S can be written similar to (4.6) after changing subscripts $\mathscr{H}_1, \mathscr{H}_2$ with $\mathscr{H}_1, S$ as $\gamma_{\mathscr{H}_1,S} = \frac{\zeta P_{\mathscr{H}_1} I^2_{\mathscr{H}_1,S}}{N_0}$ where the average SNR can be expressed as $\overline{\gamma}_{\mathscr{H}_1,S} = \frac{\zeta P_{\mathscr{H}_1}}{N_0}$. Therefore, the CDF of $\gamma_{\mathscr{H}_1,S}$ can be written as

$$F_{\gamma_{\mathscr{H}_1,S}}(\gamma) = \sum_{\rho=0}^{\infty} \begin{pmatrix} \alpha_{\mathscr{H}_1,S} \\ \rho \end{pmatrix} (-1)^{\rho} \exp\left[-\rho\left(\frac{\gamma}{\eta^2_{\mathscr{H}_1,S}\overline{\gamma}_{\mathscr{H}_1,S}}\right)^{\frac{\beta_{\mathscr{H}_1,S}}{2}}\right], \tag{4.13}$$

where $\alpha_{\mathscr{H}_1,S}$, $\beta_{\mathscr{H}_1,S}$, and $\eta_{\mathscr{H}_1,S}$ are the shape parameters and the scale parameter between $\mathscr{H}_1$ and S respectively as defined in [60, Eq. (5)][1]. In uplink communication, beam wander-induced pointing error effects should be taken into consideration. Thereby, the scintillation index for the uplink communication can be written as [13, Sect. (12)]

$$\begin{aligned}\sigma^2_{I_{\mathscr{H}_1,S}} &= 5.95(H_S - H_{\mathscr{H}_1})^2 \sec^2(\xi_{\mathscr{H}_1,S})\left(\frac{2W_0}{r_0}\right)^{\frac{5}{3}}\left(\frac{\alpha_{pe}}{W}\right)^2 \\ &+ \exp\left[\frac{0.49\sigma^2_{Bu}}{(1+(1.11+\Theta)\sigma^{\frac{12}{5}}_{Bu})^{\frac{7}{6}}} + \frac{0.51\sigma^2_{Bu}}{(1+0.69\sigma^{\frac{12}{5}}_{Bu})^{\frac{5}{6}}}\right] - 1.\end{aligned} \tag{4.14}$$

In (4.14), H_S denotes the altitude of S, $H_{\mathscr{H}_1}$ is the altitude of $\mathscr{H}_1$ above the ground level, $\xi_{\mathscr{H}_1,S}$ is the zenith angle between the $\mathscr{H}_1$ and S, W_0 indicates the beam radius at $\mathscr{H}_1$, and r_0 is the Fried's parameter. Furthermore, W indicates the beam size at the receiver, α_{pe} describes the beam wander-induced pointing error, and σ^2_{Bu} presents the Rytov variance for uplink communication. The expressions to calculate $\sigma^2_{I_{\mathscr{H}_1,S}}$ are detailed in the Appendix.

4.1.2.2 Satellite-to-HAPS communication

The received signal at $\mathscr{H}_2$ from the S can be similarly expressed as in (4.5) by just replacing the subscripts as $y_{\mathscr{H}_2} = \sqrt{\zeta P_S} I_{S,\mathscr{H}_2} x_S + n_{\mathscr{H}_2}$, whereas $I_{S,\mathscr{H}_2} = I^a_{S,\mathscr{H}_2} I^t_{S,\mathscr{H}_2} I^p_{S,\mathscr{H}_2}$ with $I^p_{S,\mathscr{H}_2}$ defines the pointing error component. Thereafter, the instantaneous SNR can be written as given in (4.6) by changing the subscripts $\mathscr{H}_1, \mathscr{H}_2$ with $S, \mathscr{H}_2$. $\alpha_{S,\mathscr{H}_2}$, $\beta_{S,\mathscr{H}_2}$, $\eta_{S,\mathscr{H}_2}$ can be derived using the same equations given in the previous section,

---

[1] The infinite summations in (4.13) require only 5 terms to converge with a convergence error of 2×10^{-6}.

and the scintillation index for S to $\mathcal{H}_2$ can be written as [13, Sect. (12)]. Furthermore, pointing error is considered as one of the major impairments of FSO communication as it involves the displacement of the communicating nodes. In the presence of non-zero boresight pointing errors, the PDF of $I^p_{S,\mathcal{H}_2}$ can be expressed as [52]

$$f_{I^p_{S,\mathcal{H}_2}}(I^p) = \frac{g^2 \exp\left(\frac{-s^2}{2\sigma_s^2}\right)}{A_0^{g^2}} (I^p)^{g^2-1} I_0\left(\frac{s}{\sigma_s^2}\sqrt{\frac{-w_{eq}^2 \ln\frac{I^p}{A_0}}{2}}\right), \tag{4.15}$$

where $g = w_{eq}/2\sigma_s$ represents the ratio between the equivalent beamwidth w_{eq} and the jitter standard deviation σ_s, which indicates the severity of the pointing error effects. Furthermore, $s = 0$ since we are considering zero boresight error, $A_0 = [\mathrm{erf}(v)]^2$ denotes the gathered optical power for zero difference between the optical spot center and the detector center, where $v = \sqrt{\pi/2a}/w_z$ is the ratio of the aperture radius a and the beamwidth w_z at distance z with $w_z = \theta z$ with θ is the transmit divergence angle [52]. Finally, $I_0(x)$ defines the modified Bessel function of the first kind with order zero. In the presence of pointing error, the CDF of $\gamma_{S,\mathcal{H}_2}$ becomes [51]

$$F_{\gamma_{S,\mathcal{H}_2}}(\gamma) = \frac{\alpha_{S,\mathcal{H}_2} g^2}{\beta_{S,\mathcal{H}_2}} \left(\frac{1}{\eta_{S,\mathcal{H}_2} A_0}\sqrt{\frac{\gamma}{\bar{\gamma}_{S,\mathcal{H}_2}}}\right)^{g^2} \sum_{i=0}^{\infty} T_2(i) G^{2,1}_{2,3}\left(T_3(i) \middle| \begin{matrix} 1-T_1, 1 \\ 0, 1-T_1, -T_1 \end{matrix}\right). \tag{4.16}$$

In (4.16), $T_1 = g^2/\beta_{S\mathcal{H}_2}$, $T_2(i) = (-1)^i \Gamma(\alpha_{S\mathcal{H}_2})/[i!\Gamma(\alpha_{S\mathcal{H}_2} - i)(1+i)^{1-T_1}]$, and $T_3(i) = (1+i)\left(\frac{1}{\eta_{S\mathcal{H}_2} A_0}\sqrt{\frac{\gamma}{\bar{\gamma}_{S\mathcal{H}_2}}}\right)^{\beta_{S\mathcal{H}_2}}$.[2] In the satellite to HAPS communication, we apply the aperture averaging technique as it can reduce signal fluctuations. Therefore, the aperture size-dependent scintillation index can be expressed as [19, Eq. (40)]. For s_2, the end-to-end instantaneous SNR at the destination D can then be obtained as

$$\gamma_0^{s_2} = \min\left\{\gamma_{G,\mathcal{H}_1}; \gamma_{\mathcal{H}_1,S}; \gamma_{S,\mathcal{H}_2}; \gamma_{\mathcal{H}_2,D}\right\}, \tag{4.17}$$

where $\gamma_{\mathcal{H}_2,D}$ is the instantaneous SNR at the destination which can be written very similar to (4.2).

---

[2] The infinite summation in (4.16) converges very fast after 5 iterations with 10^{-6} convergence error.

$$
\begin{aligned}
P^{s_1}_{out}(\gamma_{th}) = 1 - \Bigg[& \sum_{l=0}^{m_{\mathscr{H}_1}-1} \sum_{q=0}^{l} \frac{\vartheta_{\mathscr{H}_1}(1-m_{\mathscr{H}_1})_l.(-\delta_{\mathscr{H}_1})^l}{q!(\psi_{\mathscr{H}_1})^{l-q+1}(\overline{\gamma}_{G,\mathscr{H}_1})^{l+1}l!}(\gamma_{th})^q \exp(-\psi_{\mathscr{H}_1}(\gamma_{th}) \\
& \times \left(1 - \sum_{\rho=0}^{\infty} \begin{pmatrix} \alpha_{\mathscr{H}_1,\mathscr{H}_2} \\ \rho \end{pmatrix} (-1)^{\rho} \exp\left[-\rho \left(\frac{\gamma_{th}}{(\eta_{\mathscr{H}_1,\mathscr{H}_2} I^a_{\mathscr{H}_1,\mathscr{H}_2})^2 \overline{\gamma}_{\mathscr{H}_1,\mathscr{H}_2}}\right)^{\frac{\beta_{\mathscr{H}_1,\mathscr{H}_2}}{2}}\right]\right) \\
& \times \left(1 - \prod_{i=1}^{N}\left(1 - \sum_{p=0}^{m_{D_i}-1} \sum_{k=0}^{p} \frac{\vartheta_{D_i}(1-m_{D_i})_p.(-\delta_{D_i})^p}{k!(\psi_{D_i})^{p-k+1}(\overline{\gamma}_{\mathscr{H}_2,D_i})^{p+1}p!} \times (\gamma_{th})^k \exp(-\psi_{D_i}\gamma_{th})\right)\right)\Bigg],
\end{aligned}
\tag{4.21}
$$

4.2 Performance Analysis

4.2.1 Outage probability

As mentioned before, the OP can be written as

$$
P_{out} = \Pr[\gamma_0 \leq \gamma_{th}]. \tag{4.18}
$$

More precisely, the OP can be derived from the CDF of the end-to-end SNR γ_0 as $P_{out} = F_{\gamma_0}(\gamma_{th})$. Furthermore, in the case of multi-hop communication, the OP is the probability that the transmitted message is not decoded correctly by at least one of the users at the end of the communication. For s_1, the equivalent CDF of the system SNR γ_0 can be given as

$$
F^{s_1}_{\gamma_0}(\gamma) = 1 - \Big[\big(1 - F_{\gamma_{G,\mathscr{H}_1}}(\gamma)\big)\big(1 - F_{\gamma_{\mathscr{H}_1,\mathscr{H}_2}}(\gamma)\big)\big(1 - F_{\gamma_{\mathscr{H}_2,D}}(\gamma)\big)\Big], \tag{4.19}
$$

where $F_{\gamma_{\mathscr{H}_1,\mathscr{H}_2}}(\gamma)$ indicates the CDF of $\gamma_{\mathscr{H}_1,\mathscr{H}_2}$. For s_2, the CDF of the end-to-end SNR can be written as

$$
F^{s_2}_{\gamma_0}(\gamma) = 1 - \Big[\big(1 - F_{\gamma_{G,\mathscr{H}_1}}(\gamma)\big)\big(1 - F_{\gamma_{\mathscr{H}_1,S}}(\gamma)\big)\big(1 - F_{\gamma_{S,\mathscr{H}_2}}(\gamma)\big)\big(1 - F_{\gamma_{\mathscr{H}_2,D}}(\gamma)\big)\Big], \tag{4.20}
$$

and the final expressions of the OP for both scenarios are given as (4.21) and (4.22).

4.2.2 High SNR analysis

We now focus on the high SNR evaluation and obtain diversity orders for the proposed models as the obtained exact closed-form expressions provide limited physical insights. As mentioned before, in the high SNR regime, the OP is given as

$$
P^{\infty}_{out}(\gamma_{th}) = (\mathscr{G}_c\overline{\gamma})^{\mathscr{G}_d}, \tag{4.23}
$$

$$\begin{aligned} P_{out}^{s_2}(\gamma_{th}) = 1 - \Bigg[& \sum_{l=0}^{m_{\mathscr{H}_1-1}} \sum_{q=0}^{l} \frac{\vartheta_{\mathscr{H}_1}(1-m_{\mathscr{H}_1})_l.(-\delta_{\mathscr{H}_1})^l}{q!(\psi_{\mathscr{H}_1})^{l-q+1}(\overline{\gamma}_{G,\mathscr{H}_1})^{l+1}l!}(\gamma_{th})^q \exp(-\psi_{\mathscr{H}_1}\gamma_{th}) \times \Bigg(1 \\ & - \sum_{\rho=0}^{\infty} \binom{\alpha_{\mathscr{H}_1,S}}{\rho} (-1)^{\rho} \exp\left[-\rho \left(\frac{\gamma_{th}}{\eta^2_{\mathscr{H}_1,S}\overline{\gamma}_{\mathscr{H}_1,S}} \right)^{\frac{\beta_{\mathscr{H}_1,S}}{2}} \right] \Bigg) \Bigg(1 - \sum_{\rho_1=0}^{\infty} \binom{\alpha_{S,\mathscr{H}_2}}{\rho_1} \\ & \times (-1)^{\rho_1} \exp\left[-\rho_1 \left(\frac{\gamma_{th}}{(\eta_{S,\mathscr{H}_2} I^a_{S,\mathscr{H}_2})^2 \overline{\gamma}_{S,\mathscr{H}_2}} \right)^{\frac{\beta_{S,\mathscr{H}_2}}{2}} \right] \Bigg) \\ & \times \Bigg(1 - \prod_{i=1}^{N} \Bigg(1 - \sum_{p=0}^{m_{D_i}-1} \sum_{k=0}^{p} \frac{\vartheta_{D_i}(1-m_{D_i})_p.}{k!(\psi_{D_i})^{p-k+1}p!} \frac{(-\delta_{D_i})^p}{(\overline{\gamma}_{\mathscr{H}_2,D_i})^{p+1}} (\gamma_{th})^k \exp(-\psi_{D_i}\gamma_{th}) \Bigg) \Bigg) \Bigg]. \end{aligned} \tag{4.22}$$

---

where $\mathscr{G}_c$ presents the coding gain and $\mathscr{G}_d$ indicates the diversity order. The diversity order can be calculated as $\mathscr{G}_d = -\lim\limits_{\overline{\gamma}\to\infty} \frac{\log(P^{\infty}_{out})}{\log(\overline{\gamma})}$.

For s_1, if the average SNRs of RF links ($\overline{\gamma}_{G,\mathscr{H}_1}$, $\overline{\gamma}_{\mathscr{H}_2,D}$) and the average SNR of the FSO link ($\overline{\gamma}_{\mathscr{H}_1,\mathscr{H}_2}$) go to infinity, therefore, after a few manipulations and by removing the high order terms, the asymptotic OP can be written as

$$P_{out}^{s_1,\infty}(\gamma_{th}) = \frac{\vartheta_{\mathscr{H}_1}\gamma_{th}}{\overline{\gamma}_{G,\mathscr{H}_1}} + \prod_{i=1}^{N} \frac{\vartheta_{D_i}\gamma_{th}}{\overline{\gamma}_{\mathscr{H}_2,D_i}} + \left(\frac{\gamma_{th}}{(\eta_{\mathscr{H}_1,\mathscr{H}_2} I^a_{\mathscr{H}_1,\mathscr{H}_2})^2 \overline{\gamma}_{\mathscr{H}_1,\mathscr{H}_2}} \right)^{\frac{\alpha_{\mathscr{H}_1,\mathscr{H}_2}\beta_{\mathscr{H}_1,\mathscr{H}_2}}{2}}. \tag{4.24}$$

and the diversity order can obtained as

$$\mathscr{G}_d = \min\left(1, \frac{\alpha_{\mathscr{H}_1,\mathscr{H}_2}\beta_{\mathscr{H}_1,\mathscr{H}_2}}{2}, N\right). \tag{4.25}$$

Similarly, for s_2, if the average SNRs of RF links ($\overline{\gamma}_{G,\mathscr{H}_1}$, $\overline{\gamma}_{\mathscr{H}_2,D}$) and the average SNR of the FSO links ($\overline{\gamma}_{\mathscr{H}_1,S}$, $\overline{\gamma}_{S,\mathscr{H}_2}$) go to infinity, the OP can be obtained as

$$\begin{aligned} P_{out}^{s_2,\infty}(\gamma_{th}) = & \frac{\vartheta_{\mathscr{H}_1}\gamma_{th}}{\overline{\gamma}_{G,\mathscr{H}_1}} + \prod_{i=1}^{N} \frac{\vartheta_{D_i}\gamma_{th}}{\overline{\gamma}_{\mathscr{H}_2,D_i}} + \left(\frac{\gamma_{th}}{(\eta_{\mathscr{H}_1,S} I^a_{\mathscr{H}_1,S})^2 \overline{\gamma}_{\mathscr{H}_1,S}} \right)^{\frac{\alpha_{\mathscr{H}_1,S}\beta_{\mathscr{H}_1,S}}{2}} \\ & + \left(\frac{\gamma_{th}}{(\eta_{S,\mathscr{H}_2} I^a_{S,\mathscr{H}_2})^2 \overline{\gamma}_{S,\mathscr{H}_2}} \right)^{\frac{\alpha_{S,\mathscr{H}_2},\beta_{S,\mathscr{H}_2}}{2}}. \end{aligned} \tag{4.26}$$

Thereafter, the diversity order for s_2 can written as

$$\mathscr{G}_d = \min\left(1, \frac{\alpha_{\mathscr{H}_1,S}\beta_{\mathscr{H}_1,S}}{2}, \frac{\alpha_{S,\mathscr{H}_2}\beta_{S,\mathscr{H}_2}}{2}, N\right). \tag{4.27}$$

It can be noted that the diversity order depends on the turbulence parameters of the FSO link and the number of antennas of the RF links.

4.2.3 Error probability analysis

In this subsection, novel expressions for BER are derived for both scenarios. For different modulation schemes, the BER can be written as

$$P_e = \frac{v^u}{2\Gamma(u)} \int_0^\infty \gamma^{u-1} e^{(-v\gamma)} F_{\gamma_0}(\gamma) d\gamma, \tag{4.28}$$

where u, v present the different binary modulation schemes as given in Table 4.1.

Table 4.1 : BER parameters for various modulation techniques.

Binary Modulation	u	v
Coherent binary frequency shift keying (CBFSK)	0.5	0.5
Coherent binary phase shift keying (CBPSK)	0.5	1
Non-coherent binary frequency shift keying (NBFSK)	1	0.5
Differential binary phase shift keying (DBPSK)	1	1

4.2.3.1 HAPS-aided Mixed RF/FSO/RF communication

By substituting (4.19) in (4.28) with few manipulations and by using infinite series expansion[3], the BER can be obtained for s_1 as

$$P_e^{s_1} = I_1 - I_2 + I_3, \tag{4.29}$$

The integral of I_1 can be easily obtained as

$$I_1 = \frac{1}{2}. \tag{4.30}$$

I_2 and I_3 can be derived by first using the following equality $\exp(-bx) = G_{0,1}^{1,0}\left(bx \middle| \begin{matrix} - \\ 0 \end{matrix}\right)$ [71, eqn. (11)]. Thereafter, by invoking [53, eqn. (07.34.21.0013.01)], I_2 and I_3 can be obtained in (4.31) and (4.32) as given at the top of the next page. Finally, by substituting (4.30), (4.31), and (4.32) into (4.29), the closed form expression of the BER can be obtained.

---

[3] Please note that using infinite series expansion leads to a mismatch between analytical and simulation curves as can be seen in Figures 4.7 and 4.8.

$$
\begin{aligned}
I_2 = {} & \frac{v^u}{\Gamma(u)} \sum_{l=0}^{m_{\mathscr{H}_1-1}} \sum_{q=0}^{l} \frac{\vartheta_{\mathscr{H}_1}(1-m_{\mathscr{H}_1})_l.(-\delta_{\mathscr{H}_1})^l}{q!(\psi_{\mathscr{H}_1})^{l-q+1}(\overline{\gamma}_{G,\mathscr{H}_1})^{l+1}l!} \sum_{p=0}^{m_{D_1}-1} \sum_{k=0}^{p} \frac{\vartheta_{D_1}(1-m_{D_1})_p.(-\delta_{D_1})^p}{k!(\psi_{D_1})^{p-k+1}(\overline{\gamma}_{\mathscr{H}_2,D_1})^{p+1}p!} \\
& \times \sum_{\rho=1}^{\infty} \binom{\alpha_{\mathscr{H}_1,\mathscr{H}_2}}{\rho} (-1)^{\rho+1} \frac{2^{\frac{1}{2}} \beta_{\mathscr{H}_1,\mathscr{H}_2}^{(u+q+k)-\frac{1}{2}}}{(2\pi)^{\frac{\beta_{\mathscr{H}_1,\mathscr{H}_2}-1}{2}+\frac{1}{2}}} (v+\psi_{\mathscr{H}_1}+\psi_{D_1})^{-(u+q+k)} \\
& \times G^{2,\beta_{\mathscr{H}_1,\mathscr{H}_2}}_{\beta_{\mathscr{H}_1,\mathscr{H}_2},2} \left[\frac{\left(\rho\left(\frac{1}{(\eta_{\mathscr{H}_1,\mathscr{H}_2} I^a_{\mathscr{H}_1,\mathscr{H}_2})^2 \overline{\gamma}_{\mathscr{H}_1,\mathscr{H}_2}}\right)^{\frac{\beta_{\mathscr{H}_1,\mathscr{H}_2}}{2}}\right)^2 2^{-2}}{(v+\psi_{\mathscr{H}_1}+\psi_{D_1})^{\beta_{\mathscr{H}_1,\mathscr{H}_2}} \beta_{\mathscr{H}_1,\mathscr{H}_2}^{-\beta_{\mathscr{H}_1,\mathscr{H}_2}}} \middle| \begin{matrix} \frac{1-(u+q+k)}{\beta_{\mathscr{H}_1,\mathscr{H}_2}}, \ldots, \frac{\beta_{\mathscr{H}_1,\mathscr{H}_2}-(u+q+k)}{\beta_{\mathscr{H}_1,\mathscr{H}_2}} \\ 0, \frac{1}{2} \end{matrix} \right].
\end{aligned}
\tag{4.31}
$$

$$
\begin{aligned}
I_3 = {} & \frac{v^u}{2\Gamma(u)} \sum_{l=0}^{m_{\mathscr{H}_1-1}} \sum_{q=0}^{l} \frac{\vartheta_{\mathscr{H}_1}(1-m_{\mathscr{H}_1})_l.(-\delta_{\mathscr{H}_1})^l}{q!(\psi_{\mathscr{H}_1})^{l-q+1}(\overline{\gamma}_{G,\mathscr{H}_1})^{l+1}l!} \\
& \times \prod_{i=1}^{2} \left(\sum_{p=0}^{m_{D_i}-1} \sum_{k=0}^{p} \frac{\vartheta_{D_i}(1-m_{D_i})_p.(-\delta_{D_i})^p}{k!(\psi_{D_i})^{p-k+1}(\overline{\gamma}_{\mathscr{H}_2,D_i})^{p+1}k!} \right) \\
& \times \sum_{\rho=1}^{\infty} \binom{\alpha_{\mathscr{H}_1,\mathscr{H}_2}}{\rho} (-1)^{\rho+1} (v+\psi_{\mathscr{H}_1}+\psi_{D_1}+\psi_{D_2})^{-(u+q+2k)} \\
& \times G^{2,\beta_{\mathscr{H}_1,\mathscr{H}_2}}_{\beta_{\mathscr{H}_1,\mathscr{H}_2},2} \left[\frac{\left(\rho\left(\frac{1}{(\eta_{\mathscr{H}_1,\mathscr{H}_2} I^a_{\mathscr{H}_1,\mathscr{H}_2})^2 \overline{\gamma}_{\mathscr{H}_1,\mathscr{H}_2}}\right)^{\frac{\beta_{\mathscr{H}_1,\mathscr{H}_2}}{2}}\right)^2 2^{-2}}{(v+\psi_{\mathscr{H}_1}+\psi_{D_1}+\psi_{D_2})^{\beta_{\mathscr{H}_1,\mathscr{H}_2}} \beta_{\mathscr{H}_1,\mathscr{H}_2}^{-\beta_{\mathscr{H}_1,\mathscr{H}_2}}} \middle| \begin{matrix} \frac{1-(u+q+2k)}{\beta_{\mathscr{H}_1,\mathscr{H}_2}}, \ldots, \frac{\beta_{\mathscr{H}_1,\mathscr{H}_2}-(u+q+2k)}{\beta_{\mathscr{H}_1,\mathscr{H}_2}} \\ 0, \frac{1}{2} \end{matrix} \right].
\end{aligned}
\tag{4.32}
$$

4.2.3.2 Satellite-aided mixed RF/FSO/FSO/RF communication

For s_2, the expression of BER can be obtained by substituting (4.20) in (4.28) as

$$
P_e^{s_2} = L_1 - L_2 + L_3. \tag{4.33}
$$

In (4.33), $L_1 = \frac{1}{2}$ and the expressions of L_2 and L_3 are given at the top of the next page. Therefore, by substituting (4.34) and (4.35) in (4.33), the closed-form expression of BER for s_2 can be obtained.

$$
\begin{aligned}
L_2 = {} & \frac{v^u}{\Gamma(u)} \sum_{l=0}^{m_{\mathscr{H}_1}-1} \sum_{q=0}^{l} \frac{\vartheta_{\mathscr{H}_1}(1-m_{\mathscr{H}_1})_l.(-\delta_{\mathscr{H}_1})^l}{q!(\psi_{\mathscr{H}_1})^{l-q+1}(\overline{\gamma}_{G,\mathscr{H}_1})^{l+1} l!} \\
& \times \sum_{p=0}^{m_{D_1}-1} \sum_{k=0}^{p} \frac{\vartheta_{D_i}(1-m_{D_1})_p.(-\delta_{D_1})^p}{k!(\psi_{D_1})^{p-k+1}(\overline{\gamma}_{\mathscr{H}_2,D_1})^{p+1} p!} \\
& \times \sum_{\rho=1}^{\infty} \sum_{\rho_1=1}^{\infty} \binom{\alpha_{\mathscr{H}_1,S}}{\rho} \binom{\alpha_{S,\mathscr{H}_2}}{\rho_1} (-1)^{\rho+\rho_1+2} \frac{2^{\frac{1}{2}} \beta^{(u+q+k)-\frac{1}{2}}}{(2\pi)^{\frac{\beta-1}{2}+\frac{1}{2}}} \\
& \times (v+\psi_{\mathscr{H}_1}+\psi_{D_1})^{-(u+q+k)} \\
& \times G_{\beta,2}^{2,\beta} \left[\frac{\left(\rho \left(\frac{1}{(\eta_{\mathscr{H}_1,S} I^a_{\mathscr{H}_1,S})^2 \overline{\gamma}_{\mathscr{H}_1,S}} \right)^{\frac{\beta}{2}} + \rho_1 \left(\frac{1}{(\eta_{S,\mathscr{H}_2} I^a_{S,\mathscr{H}_2})^2 \overline{\gamma}_{S,\mathscr{H}_2}} \right)^{\frac{\beta}{2}} \right)^2 2^{-2}}{(v+\psi_{\mathscr{H}_1}+\psi_{D_1})^{\beta} \beta^{-\beta}} \middle| \begin{matrix} \frac{1-(u+q+k)}{\beta}, \dots, \frac{\beta-(u+q+k)}{\beta} \\ 0, \frac{1}{2} \end{matrix} \right].
\end{aligned}
\tag{4.34}
$$

$$
\begin{aligned}
L_3 = {} & \frac{v^u}{2\Gamma(u)} \sum_{l=0}^{m_{\mathscr{H}_1}-1} \sum_{q=0}^{l} \frac{\vartheta_{\mathscr{H}_1}(1-m_{\mathscr{H}_1})_l.(-\delta_{\mathscr{H}_1})^l}{q!(\psi_{\mathscr{H}_1})^{l-q+1}(\overline{\gamma}_{G,\mathscr{H}_1})^{l+1} l!} \\
& \times \prod_{i=1}^{2} \left(\sum_{p=0}^{m_{D_i}-1} \sum_{k=0}^{p} \frac{\vartheta_{D_i}(1-m_{D_i})_p.(-\delta_{D_i})^p}{k!(\psi_{D_i})^{p-k+1}(\overline{\gamma}_{\mathscr{H}_2,D_i})^{p+1} k!} \right) \\
& \times \sum_{\rho=1}^{\infty} \sum_{\rho_1=1}^{\infty} \binom{\alpha_{\mathscr{H}_1,S}}{\rho} \binom{\alpha_{S,\mathscr{H}_2}}{\rho_1} (-1)^{\rho+\rho_1+2} \frac{2^{\frac{1}{2}} \beta^{(u+q+2k)-\frac{1}{2}}}{(2\pi)^{\frac{\beta-1}{2}+\frac{1}{2}}} \\
& \times (v+\psi_{\mathscr{H}_1}+\psi_{D_1}+\psi_{D_2})^{-(u+q+2k)} \\
& \times G_{\beta,2}^{2,\beta} \left[\frac{\left(\rho \left(\frac{1}{(\eta_{\mathscr{H}_1,S} I^a_{\mathscr{H}_1,S})^2 \overline{\gamma}_{\mathscr{H}_1,S}} \right)^{\frac{\beta}{2}} + \rho_1 \left(\frac{1}{(\eta_{S,\mathscr{H}_2} I^a_{S,\mathscr{H}_2})^2 \overline{\gamma}_{S,\mathscr{H}_2}} \right)^{\frac{\beta}{2}} \right)^2 2^{-2}}{(v+\psi_{\mathscr{H}_1}+\psi_{D_1}+\psi_{D_2})^{\beta} \beta^{-\beta}} \middle| \begin{matrix} \frac{1-(u+q+2k)}{\beta}, \dots, \frac{\beta-(u+q+2k)}{\beta} \\ 0, \frac{1}{2} \end{matrix} \right].
\end{aligned}
\tag{4.35}
$$

4.2.4 Ergodic capacity

Ergodic capacity (C_e) is defined as the maximum achievable capacity of the overall system. Mathematically speaking, it can be written as

$$C_e = \frac{\log_2(e)}{n} \int_0^\infty \frac{1}{1+\gamma} \overline{F}_{\gamma_0}(\gamma) d\gamma, \tag{4.36}$$

where n shows the total transmission time which is 3 for s_1 and 4 for s_2 and $\overline{F}_{\gamma_0}(\gamma) = 1 - F_{\gamma_0}(\gamma)$. To the best of the authors' knowledge, the expression of ergodic capacity in closed-form for both scenarios cannot be derived. Therefore, by using the following approximation, the ergodic capacity can be tightly upper bounded

$$C_e = \frac{1}{n}\mathbb{E}[\log_2(1+\gamma_0)] \approx C_e^{up} = \frac{1}{n}\log_2(1+\mathbb{E}[\gamma_0]). \tag{4.37}$$

For s_1, with the aid of (4.12), C_e^{up,s_1} can be expressed as

$$C_e^{up,s_1} = \frac{1}{3}\log_2\left(1+\min\left(\mathbb{E}[\gamma_{G,\mathscr{H}_1}], \mathbb{E}[\gamma_{\mathscr{H}_1,\mathscr{H}_2}], \mathbb{E}[\gamma_{\mathscr{H}_2,D}]\right)\right). \tag{4.38}$$

In (4.38), $\mathbb{E}[\gamma_{G,\mathscr{H}_1}]$ can be obtained as

$$\mathbb{E}[\gamma_{G,\mathscr{H}_1}] = \int_0^\infty (1 - F_{\gamma_{G,\mathscr{H}_1}}(\gamma)) d\gamma = \sum_{l=0}^{m_{\mathscr{H}_1}-1} \sum_{q=0}^{l} \frac{\vartheta_{\mathscr{H}_1}(1-m_{\mathscr{H}_1})_l . (-\delta_{\mathscr{H}_1})^l}{q!(\psi_{\mathscr{H}_1})^{l-q+1}(\overline{\gamma}_{G,\mathscr{H}_1})^{l+1} l!} \Gamma[1+q] \psi_{\mathscr{H}_1}^{-(q+1)}, \tag{4.39}$$

whereas, $\mathbb{E}[\gamma_{\mathscr{H}_1,\mathscr{H}_2}]$ can be obtained as

$$\mathbb{E}[\gamma_{\mathscr{H}_1,\mathscr{H}_2}] = \int_0^\infty (1 - F_{\gamma_{\mathscr{H}_1,\mathscr{H}_2}}(\gamma)) d\gamma = \sum_{\rho=1}^{\infty} \binom{\alpha_{\mathscr{H}_1,\mathscr{H}_2}}{\rho} (-1)^{\rho+1} \rho^{\frac{2}{\beta_{\mathscr{H}_1,\mathscr{H}_2}}} \Gamma\left[1+\frac{2}{\beta_{\mathscr{H}_1,\mathscr{H}_2}}\right] \times \left(\frac{1}{(\eta_{\mathscr{H}_1,\mathscr{H}_2} I^a_{\mathscr{H}_1,\mathscr{H}_2})^2 \overline{\gamma}_{\mathscr{H}_1,\mathscr{H}_2}}\right)^{-1}. \tag{4.40}$$

The expression of $\mathbb{E}[\gamma_{\mathscr{H}_2,D}]$ can be given as

$$\mathbb{E}[\gamma_{\mathscr{H}_2,D}] = \max\left[\mathbf{E}[\gamma_{\mathscr{H}_2,D_1}], \ldots, \mathbf{E}[\gamma_{\mathscr{H}_2,D_N}]\right]. \tag{4.41}$$

By substituting (4.39), (4.40), and (4.41) into (4.38), the expression for C_e^{up,s_1} can be obtained. Similarly, C_e^{up,s_2} for s_2 can be easily obtained by following the same steps, where C_e^{up,s_2}can be given as

$$C_e^{up,s_2} = \frac{1}{4}\log_2\left(1+\min\left(\mathbb{E}[\gamma_{G,\mathscr{H}_1}], \mathbb{E}[\gamma_{\mathscr{H}_1,S}], \mathbb{E}[\gamma_{S,\mathscr{H}_2}], \mathbb{E}[\gamma_{\mathscr{H}_2,D}]\right)\right). \tag{4.42}$$

4.2.5 Energy efficiency

Energy efficiency (EE, in bits/Hz/Joule) is defined as the ratio of the spectral efficiency (C_e, in bits/s/Hz) to the total power consumption (P_t, in Watt). The EE can be expressed as [72]

$$EE = \frac{C_e}{P_t}. \tag{4.43}$$

For the first scenario s_1, we assume equal power consumption. Therefore, total power consumption can be denoted as $P_t^{s_1} = \frac{1}{3}(P_G + P_{\mathscr{H}_1} + P_{\mathscr{H}_2})$. Note that the coefficient $\frac{1}{3}$ accounts for the fact that the entire communication take place ins three phases. C_e is obtained as in (4.38). Therefore, by substituting (4.39), (4.40), and (4.41) into (4.38), the expression for spectral efficiency C_e can be obtained so as the expression of EE in (4.43). Similarly, the EE for s_2 can be easily obtained where the total power is given as $P_t^{s_2} = \frac{1}{4}(P_G + P_{\mathscr{H}_1} + P_S + P_{\mathscr{H}_2})$.

4.3 Numerical Results

In this section, we investigate the performance of our proposed setup based on the theoretical derivations developed in the previous sections. We first verify the derived expressions with MC simulations. For RF communication, we consider different shadowing severity levels as presented in [59]. For the first use-case s_1, we assume $C_n^2 = 10^{-18}$ m$^{-2/3}$ and different propagation distances between the two HAPS systems. For the second use-case s_2, the LEO satellite is located at 500 km of altitude, both HAPS systems are at altitude of 18 km. Furthermore, the beam radius at $\mathscr{H}_1$ is set to $W_0 = 2$ cm, $C_0 = 10^{-18}$ m$^{-2/3}$, $\xi_{\mathscr{H}_1,S} = \xi_{S,\mathscr{H}_2} = 70^\circ$, and $u_S = u_{\mathscr{H}_2} = 65$ m/s. For stratospheric attenuation, we consider the case of molecular absorption at the HAPS node, which is $\phi = 10^{-5}$. For all figures, the outage threshold is set to $\gamma_{out} = 7$ dB.

Figure 4.2 illustrates the OP as a function of average SNR per hop for a different number of multicast users when the source experiences the average shadowing and the destination experiences the frequent heavy shadowing level. As we can see from the figure, the theoretical results are in good agreement with the MC simulations. In addition, it is obvious that increasing the propagation distance between the HAPS systems deteriorates the overall performance as the scintillation index $\sigma^2_{I_{\mathscr{H}_1,\mathscr{H}_2}}$ increases with the distance from 0.6925 to 1.7667, which means that the turbulence

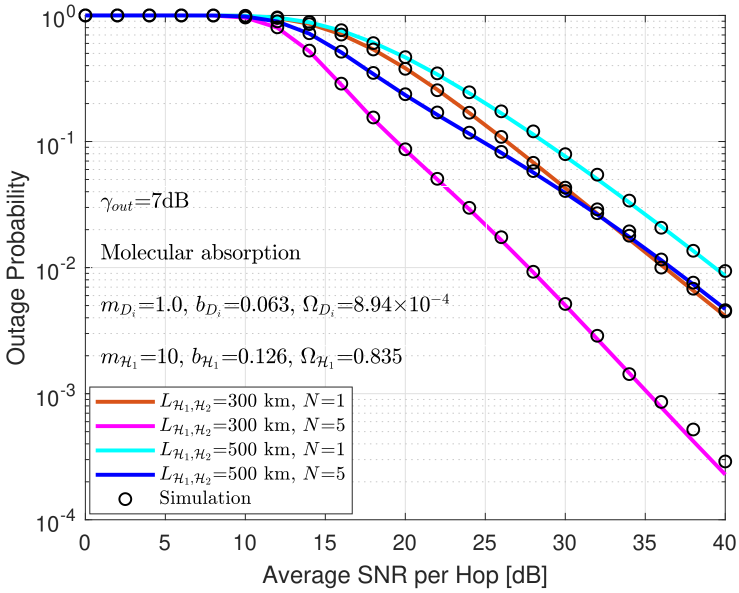

Figure 4.2 : OP performance of s_1 for different number of users and $L_{\mathscr{H}_1,\mathscr{H}_2}$.

induced-fading can severely affect the communication quality. Furthermore, as expected, serving more users at the same time enhances the outage performance.

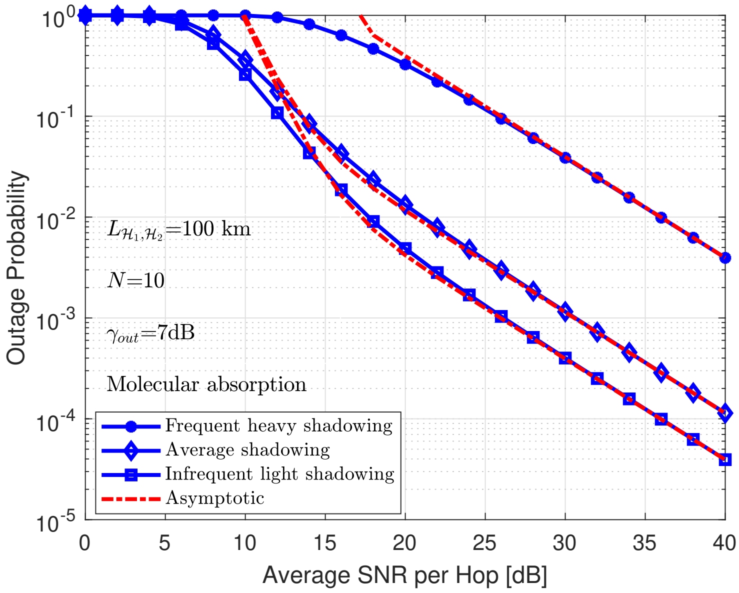

Figure 4.3 : OP performance of s_1 for various shadowing levels.

In Figure 4.3, we evaluate the OP performance of the HAPS-aided scenario for different shadowing levels. Precisely, we consider a propagation distance of 100 km between the HAPS systems and a cluster of 10 ground users. Moreover, we assume that the transmitter and the receivers experience the same shadowing level. It is clear from the figure that decreasing the shadowing level improves the overall outage performance. Finally, we can see from the figure that the asymptotic OP curves almost match the exact OP curves for the high SNR region, which validates the obtained expressions.

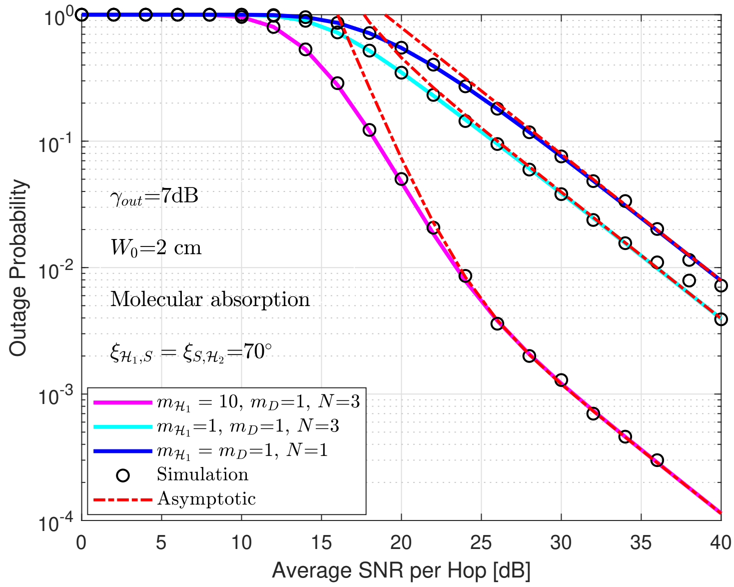

Figure 4.4 : OP performance of s_2 for different shadowing levels and various number of users.

Figure 4.4 evaluates the OP of the second scenario s_2. For the HAPS to satellite ($\mathscr{H}_1$, S) and satellite to HAPS communication (S, $\mathscr{H}_2$), we consider the same zenith angle and same wind speed. The simulation results showed that the scintillation index is the same for uplink and downlink communications even when considering the presence of beam wander-induced pointing error this is due to the fact that the HAPS node is located above the clouds' level and it is less sensitive to channel distortion. Furthermore, from this figure, we can observe that the results agree well with MC simulations validating our theoretical expressions. Similarly, the exact OP results tend to the asymptotic OP results at a high SNR regime, which verifies the correctness of our derivations. Also, we can see that the OP is significantly enhanced by increasing the number of downlink receivers. Finally, we observe that increasing the Nakagami-m severity parameter boosts the OP performance.

In Figure 4.5, we examine the outage performance of s_2 by considering the impact of pointing errors in the downlink FSO communication for different aperture sizes. The beam divergence angle is set to $\theta = 225$ urad [73] and the jitter standard deviation

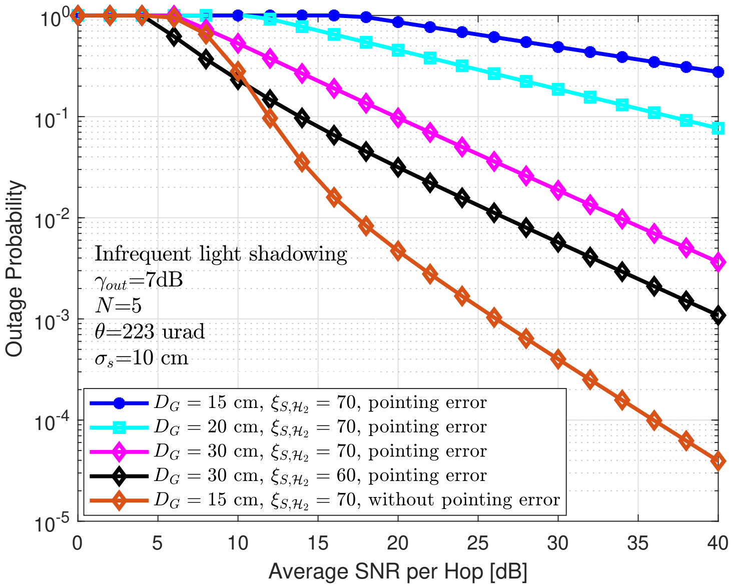

Figure 4.5 : OP performance of s_2 for various D_G in the presence of pointing error at $\mathscr{H}_2$.

is taken as $\sigma_s = 10$ cm. As expected, the presence of pointing errors deteriorates the communication and this is due to the misalignment between the satellite and the HAPS $\mathscr{H}_2$. As illustrated in the figure, increasing the aperture size improves the overall performance as it increases the amount of gathered information. Furthermore, choosing lower values of the zenith angle can yield better performance of the proposed scheme.

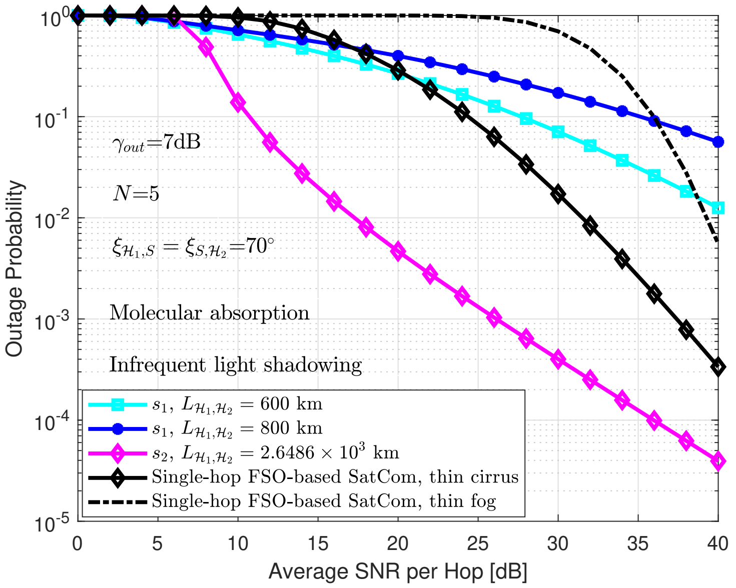

Figure 4.6 : OP comparison for different models.

Figure 4.6 compares the OP performance of the proposed scenarios and the OP of single-hop FSO-based SatCom. For the first scenario, we consider two different propagation distances between $\mathscr{H}_1$ and $\mathscr{H}_2$. For the second scenario, we assume $\xi_{\mathscr{H}_1,S} = \xi_{S,\mathscr{H}_2} = 70^\circ$ and $u_S = u_{\mathscr{H}_2} = 65$ m/s, which results in 2.6486×10^3 km of separation between the two HAPS systems. For the single-hop FSO-based SatCom system, we assume a ground station that seeks to send the same information to a set of ground destinations through an LEO satellite located at 500 km altitude using optical communication. The FSO channels follow the EW fading. We also consider thin cirrus clouds and thin fog conditions for the ground receivers. The zenith angle is set to $\xi = 70^\circ$ and $v =$2.8 m/s for wind speed. For all scenarios, we consider five multicast users and that all RF channels experience infrequent light shadowing. It is inferred from the figure that for larger distances between the communicating users, the second scenario is more practical as it performs better even in windy weather and high zenith angles. As expected, at higher propagation distances, the overall performance of s_1 decreases. On one hand, we observe that the outage performance of single-hop FSO-based SatCom outperforms s_1 for thin cirrus condition. On the other hand, as expected, for foggy weather, s_1 could provide better performance than single-hop FSO-based SatCom as FSO communication is highly deteriorated by fog conditions. Finally, s_2 performs better than single-hop FSO-based SatCom as the use of HAPS as a relay node in SatCom enhances the communication even though we consider harsh wind speed level.

Figures 4.7 and 4.8 depict the BER vs. average SNR for both scenarios while considering CBPSK modulation as it provides better performance. For s_1, we consider the frequent heavy shadowing effect for all RF links and 200 km that separate $\mathscr{H}_1$ and $\mathscr{H}_2$ for $N =1$ and $N =3$. For s_2, we assume $N =2$ and different shadowing levels. The zenith angle is set to $\xi_{\mathscr{H}_1,S} = \xi_{S,\mathscr{H}_2} = 70^\circ$. For the single-hop FSO-based SatCom, we assume a zenith angle of $\xi = 80^\circ$ due to the large distance, wind speed level as v=11.176 m/s [19], thin cirrus conditions, and the presence of Mie scattering [19]. As can be seen in Figure 4.7, increasing N yields an enhanced performance. In Figure 4.8, as expected the system yields better performance when considering the average shadowing effect. In addition, under these assumptions, our proposed models perform better than single-hop FSO-based SatCom, especially at low SNR. Furthermore, as

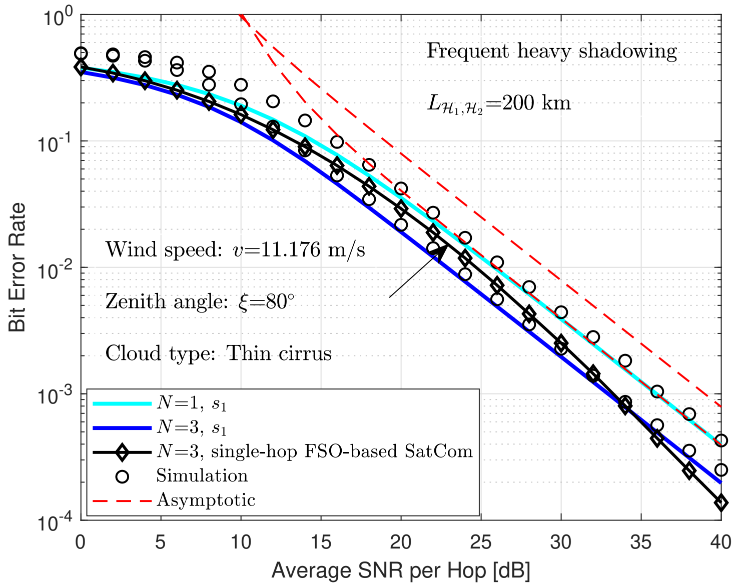

Figure 4.7 : Bit error rate vs. average SNR for s_1.

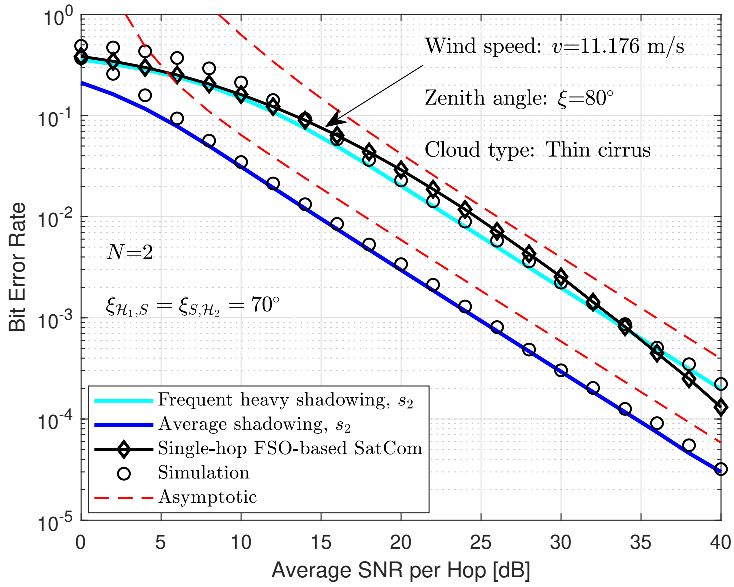

Figure 4.8 : Bit error rate vs. average SNR for s_2.

observed, the simulation results confirm the theoretical derivations. Finally, the asymptotic curves, represented by dashed lines, converge to the exact performance curves in the high SNR region.

Figures 4.9 and 4.10 show the ergodic capacity performance for s_1 and s_2 using the upper-bound ergodic capacity and MC simulations for the exact ergodic capacity. As can be seen in the figures, for heavy shadowing, the approximate findings are in good agreement with the exact results. However, for average shadowing, the exact

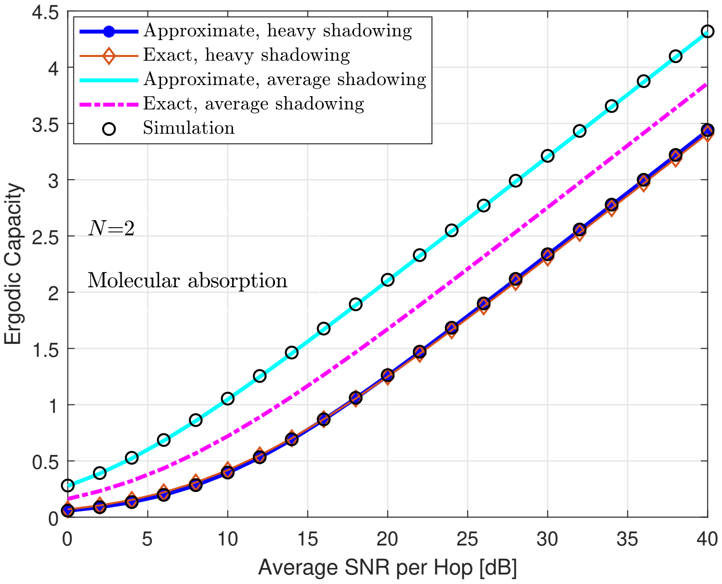

Figure 4.9 : Ergodic capacity performance vs. average SNR for s_1.

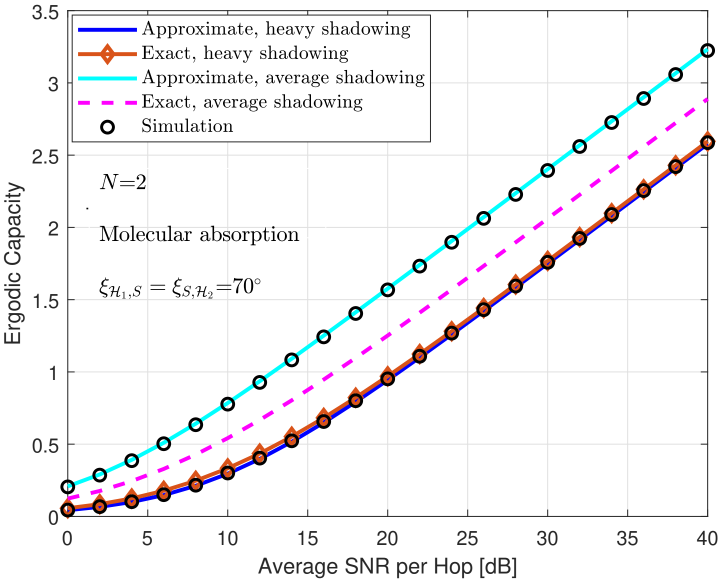

Figure 4.10 : Ergodic capacity performance vs. average SNR for s_2.

results are upper-bounded with the approximate curves. Furthermore, as expected, the ergodic capacity in average shadowing outperforms the results of heavy shadowing. Additionally, the upper-bound curves agree well with MC simulations confirming the accuracy of the theoretical analysis. It is also inferred from the figures that s_1 achieves better capacity than s_2.

Figure 4.11 illustrates the EE of both scenarios s_1 and s_2, while assuming the same conditions of shadowing. As can be seen, the EE increases at first and then deteriorates

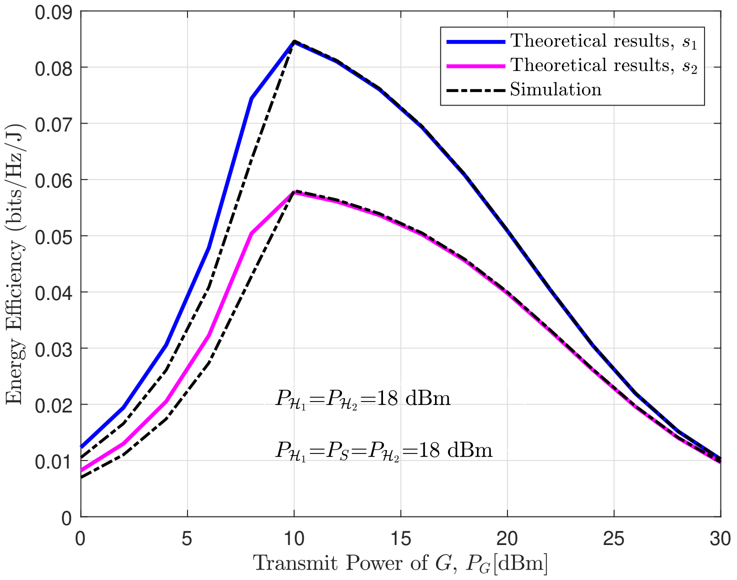

Figure 4.11 : Energy efficiency performance vs. P_G [dBm] for s_1 and s_2.

as P_G increases in both scenarios. Moreover, the results have shown that s_1 could achieve higher EE than s_2.

Finally, some design guidelines can be summarized as follows:

- We observe from the results that the effect of beam wander-induced pointing error from HAPS to satellite is almost negligible. Thus, deploying a HAPS node as a relay between the ground station and the LEO satellite significantly improves the uplink performance.
- The results have shown that multicast services can increase the diversity gain and achieves a better outage performance.
- The simulations have shown that the use of an LEO satellite can be a promising solution for inter-HAPS communication when HAPS systems are deployed far from each other.
- The results have shown that the presence of pointing errors in downlink FSO communication deteriorates the overall performance. However, decreasing the zenith angle or increasing the aperture size of the receiver lens can mitigate the impact of pointing errors as they decrease the impact of stratospheric turbulence.
- As observed s_2 could achieve better OP, whereas, s_1 achieves higher EE. Thus, there is a trade-off between EE and the OP of the proposed scenarios.

- On the one hand, using an LEO satellite as a relay node provides better performance in terms of OP. On the other hand, using HAPS nodes as a relay node is more suitable for non-delay tolerant and real-time applications also provides better coverage.

4.4 Summary and Discussion

In this work, we proposed two different use-cases for multicast applications namely HAPS-aided mixed RF/FSO/RF and satellite-aided mixed RF/FSO/FSO/RF schemes. For the proposed setups, OP expressions are derived in closed-form by considering shadowed-Rician fading for RF links and EW fading for FSO communication. The derived expressions are validated with MC simulations. For the proposed models, we investigated the impact of beam wander, pointing errors, zenith angle, aperture averaging technique for FSO communications, and the impact of shadowing level for RF communication. From the results, we observed that the use of HAPS as an intermediate node in uplink SatCom alleviates the impact of beam wander-induced pointing error. In addition, the results showed that for larger distances, the satellite-aided mixed RF/FSO/FSO/RF scenario performed better in terms of OP. The aperture averaging technique can be adopted to minimize the effect of atmospheric turbulence and improve communication in the presence of misalignment. Finally, the results have shown that the satellite-aided mixed RF/FSO/FSO/RF scenario achieves better OP and is able to serve more distant users. However, the HAPS-aided mixed RF/FSO/RF scenario achieves better EE.

After studying the characteristics of RF and FSO channels for future NTN systems from a communication perspective, in the next chapters, we are interested in investigating the PLS performance of both channels in NTNs by proposing different system models.

5. ON THE USE OF HAPS TO INCREASE SECRECY PERFORMANCE IN SATELLITE NETWORKS

In the previous chapters, we mainly focused on studying the behavior of RF and FSO communications in NTN systems during the propagation through the atmosphere. In this regard, the performance evaluation for different scenarios with different conditions was obtained from a communication perspective for unicast and multicast services. Different from the previous perspective, we now focus on investigating the physical performance for both channels RF and FSO in SatCom systems from a security perspective. More specifically, in this chapter, we investigate the secrecy performance of RF eavesdropping for a HAPS-aided SatCom system. The HAPS node is used as an intermediate relay to transmit the LEO satellite's signal to the GS. In this architecture, FSO communication is adopted between HAPS and satellite, whereas RF communication is used between HAPS and GS as the LOS communication cannot be established.

As mentioned in chapter 1, the study presented in this chapter has been published in the following paper:

O. Ben Yahia, E. Erdogan, and G. Karabulut Kurt, "On the use of HAPS to increase secrecy performance in satellite networks", in IEEE International Conference on Communications Workshops (ICC Workshops), 2021, pp. 1–6.

This chapter is organized as follows: In Section 5.1, the proposed system model and corresponding channel models are briefly introduced. The SOP and PPSC analyses are provided in Section 5.2. The analytical expressions are evaluated and discussed in Section 5.3 along with the proposed design guidelines. Finally, Section 5.4 concludes the chapter.

5.1 Signals and System Model

In this study [74], we investigate a HAPS-aided FSO-RF SatCom system as shown in Figure 5.1. In this scenario, an LEO satellite S seeks to communicate with a

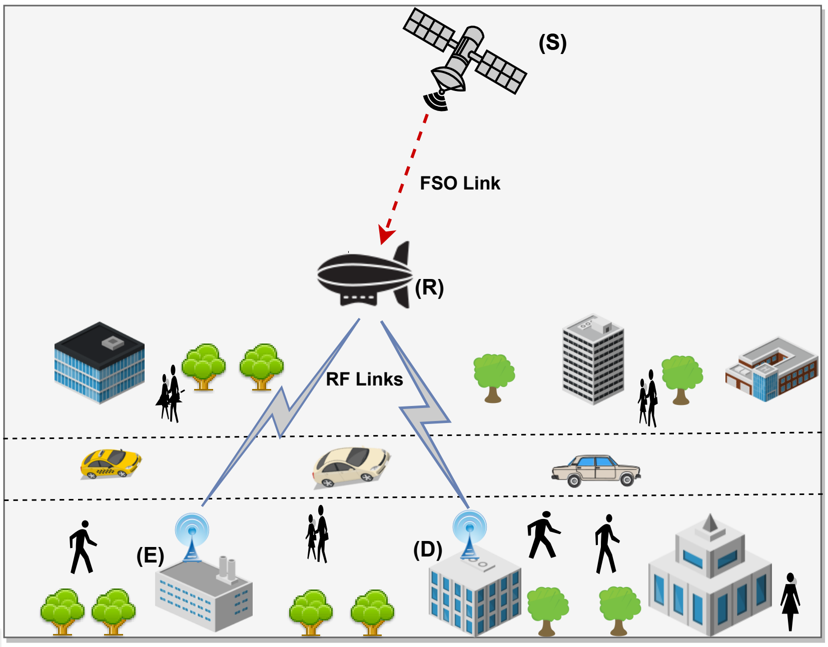

Figure 5.1 : Illustration of the HAPS-aided FSO-RF SatCom system model.

terrestrial destination D through a HAPS node R in the presence of a terrestrial passive eavesdropper E that attempts to detect the confidential message sent by S. The communication link between S and R is through an FSO link that follows the Gamma-Gamma distribution, whereas the RF links are modeled as shadowed-Rician fading. In the second phase of the communication, the received signal can be expressed as

$$y_z = h_z x + n, z \in \{RD, RE\}, \tag{5.1}$$

where x denotes the transmit signal vector, n is the AWGN, and h_z is the channel response, which can be expressed as [75]

$$h_z = F_z g_z, \tag{5.2}$$

where g_z denotes the channel coefficient and F_z is the scaling parameter including free space loss (FSL) and antenna pattern [75]. Considering DF relaying scheme, the overall SNR of our system can be expressed as

$$\gamma_0 = \min(\gamma_{SR}^{FSO}, \gamma_{RD}^{RF}), \tag{5.3}$$

where $\gamma_{SR}^{FSO} = \frac{P_s}{N_0} I_{SR}^2$ and $\gamma_{RD}^{RF} = \frac{P_R}{N_0} |h_{RD}|^2$.

5.1.1 Channel models

Since the RF links experience the shadowed-Rician fading, the PDF and the CDF of the received SNR are given as [59]

$$f_{\gamma_z}^{RF}(\gamma) = \sum_{k=0}^{m_z-1} \frac{\alpha_z(1-m_z)_k.(-\delta_z)^k\gamma^k}{\overline{\gamma}_z^{k+1}.(k!)^2} \exp(-\lambda_z\gamma), \tag{5.4}$$

$$F_{\gamma_z}^{RF}(\gamma) = 1 - \sum_{k=0}^{m_z-1} \sum_{i=0}^{k} \frac{\alpha_z(1-m_z)_k.(-\delta_z)^k\gamma^i}{i!\lambda_z^{k-i+1}\overline{\gamma}_z^{k+1}.k!} \exp(-\lambda_z\gamma), \tag{5.5}$$

where $\lambda_z = \frac{\beta_z-\delta_z}{\overline{\gamma}_z}$, $\overline{\gamma}_z$ is the average SNR for the channel h_z. $\alpha_z = \frac{1}{2b_z}(\frac{2b_zm_z}{2b_zm_z+\Omega_z})^{m_z}$, $\beta_z = \frac{1}{2b_z}$, $\delta_z = \frac{\Omega_z}{2b_z(2b_zm_z+\Omega_z}$ with m_z indicating the Nakagami-m parameter of the corresponding link, and Ω_z, $2b_z$ are the average power of the LOS component and multipath component.

For the FSO link, we consider a clear alignment between the S and R apertures. Thereby, the PDF and CDF of the instantaneous SNR at the R node (γ_{SR}^{FSO}) can be given as [59]

$$f_{\gamma_{SR}}^{FSO}(\gamma) = \frac{\xi^2}{r\Gamma(\alpha)\Gamma(\beta)\gamma} G_{1,3}^{3,0}\left(h\alpha\beta(\frac{\gamma}{\mu_r})^{\frac{1}{r}} \middle| \begin{matrix} \xi^{2+1} \\ \xi^2, \alpha, \beta \end{matrix}\right), \tag{5.6}$$

$$F_{\gamma_{SR}}^{FSO}(\gamma) = \frac{\xi^2 r^{\alpha+\beta-2}}{2\pi^{r-1}\Gamma(\alpha)\Gamma(\beta)} G_{r+1,3r+1}^{3r,1}\left(\frac{(h\alpha\beta)^r}{\mu_r r^{2r}}\gamma \middle| \begin{matrix} 1, k_1 \\ k_2, 0 \end{matrix}\right), \tag{5.7}$$

where the parameter r indicates the used type of detection at the HAPS node (i.e., $r = 1$ for HD and $r = 2$ denotes the IM/DD), the coefficient ξ implies the pointing error displacement at the receiver, α and β specify the severity of fading and scintillation produced by the atmospheric turbulence conditions, $h = \frac{\xi^2}{\xi^{2+1}}$, and μ_r presents the average SNR of the corresponding FSO link within the specific type of detection. Furthermore, $k_1 = \Delta(r, \xi^2+1)$, $k_2 = \Delta(r, \xi^2), \Delta(r, \alpha), \Delta(r, \beta)$ where the notation $\Delta(k, a)$ denotes $\Delta(k, a) = \frac{a}{k}, \frac{a+1}{k} ..., \frac{a+k-1}{k}$ including k values. For simplicity, we assume the following notations hereinafter: $B = \frac{\xi^2 r^{\alpha+\beta-2}}{2\pi^{r-1}\Gamma(\alpha)\Gamma(\beta)}$, $D = \frac{(h\alpha\beta)^r}{\mu_r r^{2r}}$. According to [13, Sect. (12)], the severity of fading and the severity of scintillation parameters are defined as

$$\alpha = \left\{\exp\left[\frac{0.49\sigma_R^2}{(1+1.11\sigma_R^{12/5})^{7/6}}\right] - 1\right\}^{-1}, \tag{5.8}$$

$$\beta = \left\{ \exp\left[\frac{0.51\sigma_R^2}{(1+0.69\sigma_R^{12/5})^{5/6}} \right] - 1 \right\}^{-1}, \tag{5.9}$$

where σ_R is the Rytov variance given as [13, Sect. (12)]

$$\sigma_R^2 = 2.25K^{7/6} sec^{11/6}(\zeta) \int_{h_0}^{H} C_n^2(h)(h-h_0)^{5/6} dh, \tag{5.10}$$

where $K = \frac{2\pi}{\lambda}$ is the wave number, λ is the wavelength, ζ represents the zenith angle, and $C_n^2(h)$ is the refractive-index structure parameter expressed as [35]

$$\begin{aligned} C_n^2 &= 0.00594(w/27)^2(10^{-5}h)^{10}\exp(-h/1000) + 2.7 \\ &\times 10^{-16}\exp(-h/1500) + A\exp(-h/100), \end{aligned} \tag{5.11}$$

where A is a nominal value of $C_n^2(0)$ at the ground in m$^{-2/3}$, w is the RMS wind spread [m/s], h is the altitude, H is the altitude of S, and h_0 presents the height of R node above ground level.

5.2 Secrecy Performance Analysis

In this section, we derive the closed-form SOP and PPSC expressions for the proposed setup.

5.2.1 Secrecy outage probability

In information theoretic security, E can be a malicious user which has an intention of listening the transmission. In that case, S has to provide $C_s > R_s$. Thereby, SOP which is considered as an important metric in PLS, can be defined as the probability that the achievable secrecy capacity C_s falls below a predefined threshold rate R_s, where C_s can be given by

$$C_s = \begin{cases} \frac{1}{2}\log_2(1+\gamma_0) - \frac{1}{2}\log_2(1+\gamma_E)\ , \gamma_0 > \gamma_E \\ \\ 0\ , \text{otherwise}, \end{cases} \tag{5.12}$$

and the SOP can be expressed as [76]

$$\begin{aligned} P_{\text{SO}} &= Pr\left[C_s < R_s\right], \\ &= \int_0^{\infty} F_{\gamma_0}\left(\gamma\gamma_{th} + \gamma_{th} - 1\right) f_{\gamma_E}\left(\gamma\right) d\gamma, \\ &\simeq \int_0^{\infty} F_{\gamma_0}\left(\gamma\gamma_{th}\right) f_{\gamma_E}\left(\gamma\right) d\gamma, \end{aligned} \tag{5.13}$$

where $\gamma_{th} = 2^{2R_s}$.

In the HAPS-aided FSO-RF communication scenario, the end-to-end SNR can be written as

$$\begin{aligned} F_{\gamma_0}(\gamma) &= 1 - \Pr[\gamma_{SR}^{FSO} > \gamma]\Pr[\gamma_{RD}^{RF} > \gamma] \\ &= 1 - \left(1 - F_{\gamma_{SR}^{FSO}}(\gamma)\right)\left(1 - F_{\gamma_{RD}^{RF}}(\gamma)\right), \end{aligned} \tag{5.14}$$

and $F_{\gamma_0}(\gamma)$ can be obtained by substituting (5.5) and (5.7) into (5.14) as

$$\begin{aligned} F_{\gamma_0}(\gamma) = 1 - &\left(1 - BG_{r+1,3r+1}^{3r,1}\left(D\gamma \middle| \begin{matrix} 1, k_1 \\ k_2, 0 \end{matrix}\right)\right) \\ &\times \sum_{k=0}^{m_{RD}-1} \sum_{i=0}^{k} \frac{\alpha_{RD}(1-m_{RD})_k.(-\delta_{RD})^k \gamma^i}{i!\lambda_{RD}^{k-i+1}\bar{\gamma}_{RD}^{k+1}.k!} \exp(-\lambda_{RD}\gamma). \end{aligned} \tag{5.15}$$

and the PDF of γ_E can be obtained directly from (5.4). Thereafter, by substituting (5.4) and (5.15) into (5.13), the SOP can be expressed as

$$\begin{aligned} P_{\text{SO}} = \int_0^\infty &\left(1 - \left(1 - BG_{r+1,3r+1}^{3r,1}\left(D\gamma_{th}\gamma \middle| \begin{matrix} 1, k_1 \\ k_2, 0 \end{matrix}\right)\right)\right. \\ &\left.\times \sum_{p=0}^{m_{RD}-1} \sum_{t=0}^{p} \frac{\alpha_{RD}(1-m_{RD})_p.(-\delta_{RD})^p}{t!\lambda_{RD}^{p-t+1}\bar{\gamma}_{RD}^{p+1}.p!} \exp(-\lambda_{RD}\gamma\gamma_{th})\right) \\ &\times (\gamma\gamma_{th})^t \sum_{q=0}^{m_{RE}-1} \frac{\alpha_{RE}(1-m_{RE})_q.(-\delta_{RE})^q}{\bar{\gamma}_{RE}^{P+1}.(q!)^2} \gamma^q \exp(-\lambda_{RE}\gamma) d\gamma. \end{aligned} \tag{5.16}$$

The closed-form solution of the above-mentioned equation can be solved by using the equation [53, eqn. 07.34.21.0011.01] and with the aid of $\exp(-bx) = G_{0,1}^{1,0}\left(bx \middle| \begin{matrix} - \\ 0 \end{matrix}\right)$ as

$$\begin{aligned} P_{\text{SO}} = 1 - &\sum_{p=0}^{m_{RD}-1} \sum_{t=0}^{p} \frac{\alpha_{RD}(1-m_{RD})_p.(-\delta_{RD})^p}{t!\lambda_{RD}^{p-t+1}\bar{\gamma}_{RD}^{p+1}.p!} \\ &\times \sum_{q=0}^{m_{RE}-1} \frac{\alpha_{RE}(1-m_{RE})_q.(-\delta_{RE})^q}{\bar{\gamma}_{RE}^{q+1}.(q!)^2} \gamma_{th}^t \\ &\times \left[(\lambda_{SD}\gamma_{th})^{-(q+t+1)} G_{1,1}^{1,1}\left(\frac{\lambda_{SE}}{\lambda_{SD}\gamma_{th}} \middle| \begin{matrix} -(q+t) \\ 0 \end{matrix}\right)\right. \\ &- G_{r+2,3r+1}^{3r,2}\left(\frac{D\gamma_{th}}{(\lambda_{RE}+\lambda_{RD}\gamma_{th})} \middle| \begin{matrix} 1, -(q+t), k_1 \\ k_2, 0 \end{matrix}\right) \\ &\left.\times B(\lambda_{RE}+\lambda_{RD}\gamma_{th})^{-(q+t+1)}\right]. \end{aligned} \tag{5.17}$$

5.2.2 Probability of positive secrecy capacity analysis

Let us consider E as a licensed user in the system which intends to capture the signal sent by the transmitter. Thus, S has the information of E and to guarantee information theoretic security, the condition $C_s > 0$ needs to be satisfied. Mathematically speaking, PPSC can be expressed as

$$\begin{aligned} P_{PPSC} &= \Pr[C_s > 0] \\ &= \Pr\Big[\frac{1}{2}\log_2(1+\gamma_0) > \frac{1}{2}\log_2(1+\gamma_E)\Big], \end{aligned} \tag{5.18}$$

and after some manipulations, it can be given as [77]

$$P_{PPSC} = 1 - \int_0^{\infty} F_{\gamma_0}(\gamma) f_{\gamma_E}(\gamma) d\gamma. \tag{5.19}$$

Thereafter, by substituting (5.4) and (5.15) into (5.19) the final expression of PPSC can be obtained very similar to (5.17) as

$$\begin{aligned} P_{PPSC} = &\sum_{p=0}^{m_{RD}-1} \sum_{t=0}^{p} \frac{\alpha_{RD}(1-m_{RD})_p \cdot (-\delta_{RD})^p}{t! \lambda_{RD}^{p-t+1} \overline{\gamma}_{RD}^{p+1} \cdot p!} \\ &\times \sum_{q=0}^{m_{RE}-1} \frac{\alpha_{RE}(1-m_{RE})_q \cdot (-\delta_{RE})^q}{\overline{\gamma}_{RE}^{q+1} \cdot (q!)^2} \gamma_{th}^{t} \\ &\times \Bigg[(\lambda_{SD}\gamma_{th})^{-(q+t+1)} \times G_{1,1}^{1,1}\left(\frac{\lambda_{SE}}{\lambda_{SD}\gamma_{th}} \middle| \begin{matrix} -(q+t) \\ 0 \end{matrix} \right) \\ &- G_{r+2,3r+1}^{3r,2}\left(\frac{D\gamma_{th}}{(\lambda_{RE}+\lambda_{RD}\gamma_{th})} \middle| \begin{matrix} 1, -(q+t), k_1 \\ k_2, 0 \end{matrix} \right) \\ &\times B(\lambda_{RE}+\lambda_{RD}\gamma_{th})^{-(q+t+1)} \Bigg]. \end{aligned} \tag{5.20}$$

5.3 Numerical Results

In this section, we quantify the secrecy performance of the proposed model under various conditions and verify our results with MC simulations. We consider that LEO satellite is circularly orbiting at 500 km whereas, the HAPS node is at an altitude of 14 km. Furthermore, we consider different shadowing levels for the RF links as given in [59]. For the FSO link, we investigate the performance for HD detection ($r = 1$) with $\lambda = 1550$ nm, and the nominal value A is $A = 1.7 \times 10^{-14}\text{m}^{-2/3}$. Moreover, we assume windy weather condition with $w = 65$ m/s and zenith angle is set to $\zeta = 75^{\circ}$. Thereby, the corresponding α and β parameters are obtained as $\alpha = 8.9033$ and $\beta = 7.3955$.

Table 5.1 : Simulation parameters.

FSO link	
Parameter	Value
Satellite height (H)	500 km
HAPS altitude (h_0)	14 km
Zenith angle (ζ)	75°
Wind speed (w)	65 m/s
Elevation above sea level (h_E)	0.8 km
Nominal value (C_0)	1.7×10^{-14}
Severity of fading (α)	8.9033
Severity of scintillation (β)	7.3955
Threshold (R_s)	0.01 nats/s/Hz

For all figures, we consider that the threshold rate is $R_s = 0.01$ nats/s/Hz. Table 5.1 presents the simulation parameters for the FSO link.

5.3.1 Verification of theoretical expressions

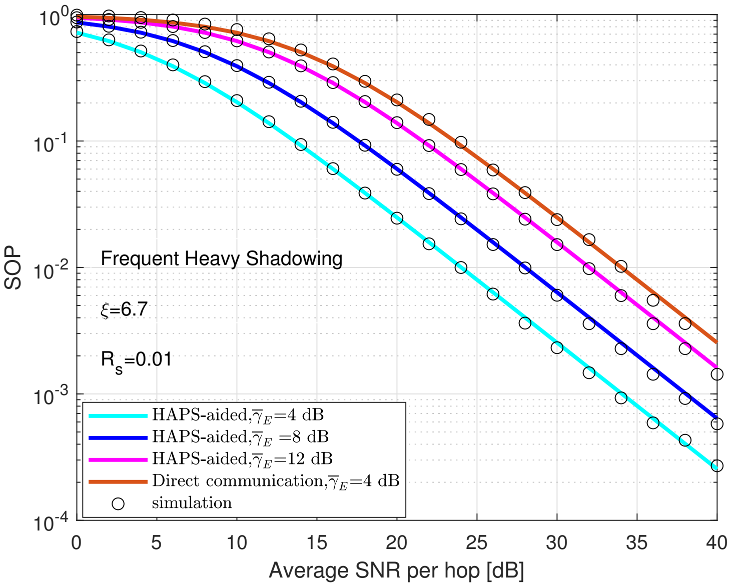

Figure 5.2 : SOP performance of the proposed model for different $\overline{\gamma}_E$.

As we can see, Figure 5.2 illustrates the SOP as a function of the average SNR per-hop $\overline{\gamma}$ under different eavesdropper SNRs for frequent heavy shadowing. The theoretical curves, which are illustrated with solid lines are verified with the simulations which are shown with circles. Furthermore, we can observe the good agreement with the simulations which confirms our derivations. It is obvious from this figure that larger $\overline{\gamma}_E$ values imply lower SOP performance. Furthermore, it is clear from the figure that the proposed scenario outperforms the scenario of using a direct RF link due to path loss caused by the large distance between the satellite and the GS.

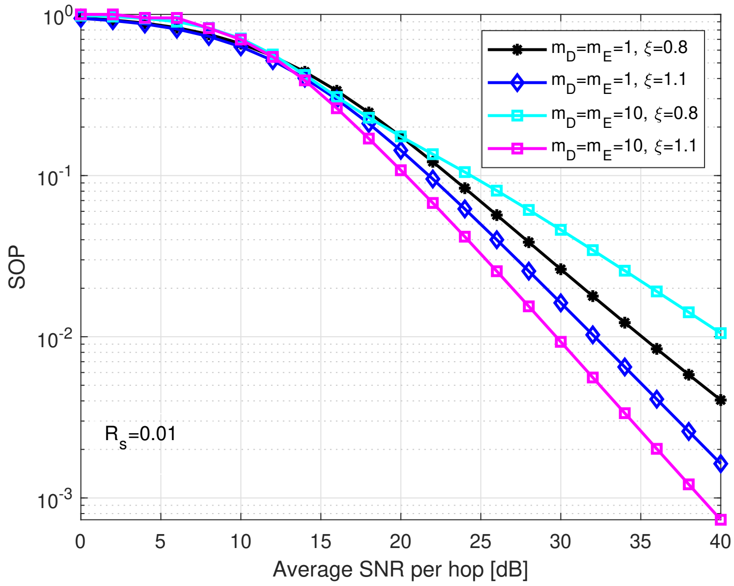

Figure 5.3 : Impact of pointing error on the SOP performance.

In Figure 5.3, we investigate the pointing error effect for frequent heavy shadowing and average shadowing. As we can see from the figure, in the case of $\xi = 1.1$ that indicates a lower level of pointing, the SOP under average shadowing outperforms the SOP under frequent heavy shadowing. However, when $\xi = 0.8$ the overall performance of the SOP under average shadowing deteriorates. In fact, as the link between the satellite and HAPS is highly affected due to the misalignment caused by a high level of pointing error, it dominates the communication even though the channel between HAPS to ground is improved.

In Figure 5.4, we evaluate the SOP when the main destination is under different shadowing levels, whereas the eavesdropper is under frequent heavy shadowing. As expected, when the channel of the intended receiver is less shadowed than the channel of the illegitimate receiver, the overall performance of the SOP enhances.

Figure 5.5 shows the PPSC performance of the RF eavesdropper attack for different γ_E values when both channels of D and E are under frequent heavy shadowing, for $\xi = 6.7$. As observed from the figure, the PPSC increases as γ_E decreases. This shows the high impact of γ_E to guarantee secure communication.

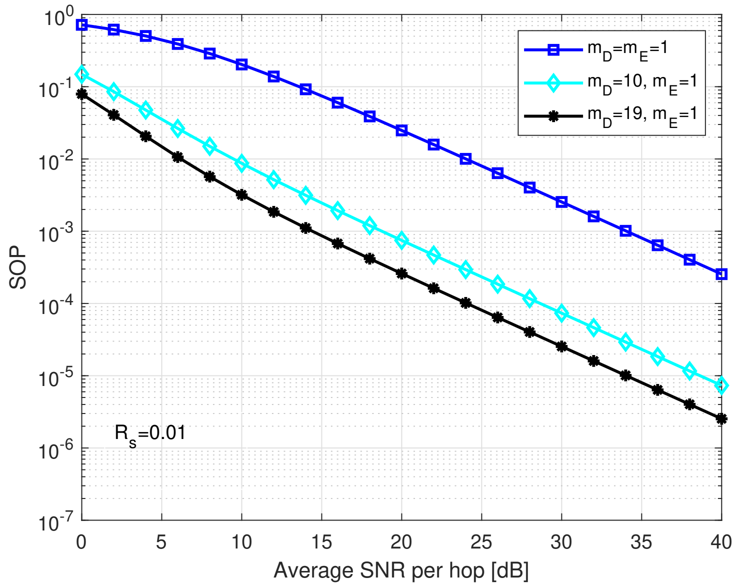

Figure 5.4 : SOP performance under different shadowing levels for D and E.

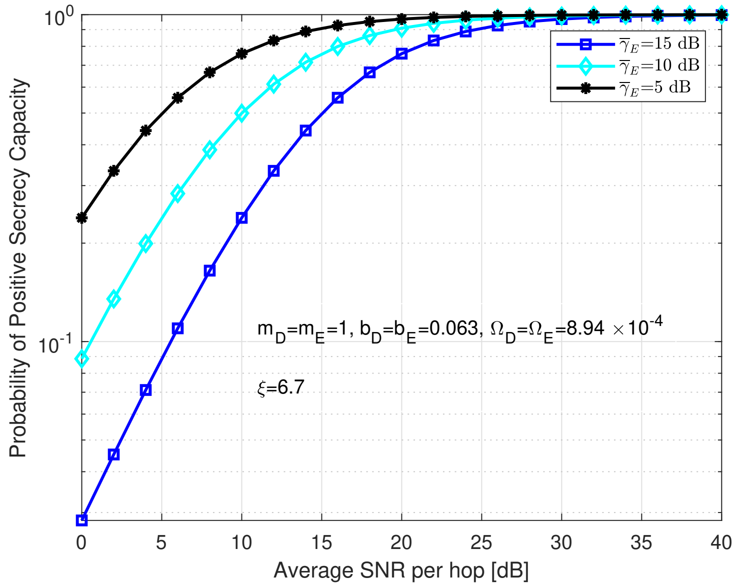

Figure 5.5 : PPSC performance for different $\overline{\gamma}_E$.

5.3.2 Design guidelines

Finally, we outline some important points to design secure downlink SatCom systems.

- For the design of the RF link, severe shadowing conditions can deteriorate the overall secrecy performance of HAPS-aided FSO-RF SatCom.
- Considering that the HAPS node is located at the stratosphere, the FSO channel from the satellite to the HAPS can not be affected heavily from the adverse weather

conditions. Thereby, HAPS can guarantee the secure communication even in the presence of harsh winds and the overall SOP performance can be enhanced.

- The simulations have shown that higher values of pointing error enhance the overall performance. Thus, ξ can be considered as an important parameter in the design of the FSO communication as it is related with the misalignment of the communicating parts.
- The average SNR of the eavesdropper can be considered as a crucial parameter in the scenario to secure the HAPS-aided SatCom.

5.4 Summary and Discussion

In this chapter, a framework to counter RF eavesdropping has been proposed by considering a HAPS-aided FSO-RF SatCom. Specifically, we derived the closed-form of SOP and PPSC expressions for the proposed system model. The results, which were validated with simulations, proved that the RF link conditions have a larger impact on the performance of the investigated system. Furthermore, shadowing parameters, and pointing errors can be critical to guarantee the secure SatCom. As expected, when the channel of the illegitimate user is more shadowed, the secrecy performance is enhanced.

In the next chapters, we investigate the secrecy performance of FSO eavesdropping in NTN systems.

6. PHYSICAL LAYER SECURITY FOR OPTICAL NON-TERRESTRIAL NETWORKS

In the previous chapter, we studied the secrecy performance of RF eavesdropping for dual-hop SatCom system using a HAPS node as a relay, where the eavesdropper is located on the ground. From a different perspective, to investigate the PLS performance in NTN systems, in this chapter, we propose a new PLS framework for optical space/air networks. More precisely, we consider two practical eavesdropping scenarios: FSO eavesdropping in space and FSO eavesdropping in the air. In the former, we assume that a HAPS node is trying to capture the confidential information from an LEO satellite, whereas in the latter, a UAV eavesdropper is trying to intercept the confidential information of a HAPS node.

The study presented in this chapter has been published in the following paper:

O. Ben Yahia, E. Erdogan, G. Karabulut Kurt, I. Altunbas, and H. Yanikomeroglu, "Physical layer security framework for optical non-terrestrial networks (invited paper)", in International Conference on Telecommunications (ICT), 2021, pp. 162–166.

The remainder of this chapter is organized as follows. We first introduce the signals and system model in Section 6.1. The expressions of secrecy performance are given in Section 6.2. In Section 6.3, our proposed models are investigated through numerical results and discussion. Finally, we conclude this chapter in Section 6.4.

6.1 Signals and System Model

As shown in Figure 6.1, we consider two use-cases of FSO eavesdropping through downlink communication for aerial networks [78]. In both cases, we assume a single-antenna transmitter (S) communicating with a flying destination node (D) in the presence of a malicious user (E). In the first scenario, we assume an LEO satellite communicating with the legitimate quasi-stationary HAPS node positioned in the stratosphere while a HAPS eavesdropper is trying to capture the transmitted signal.

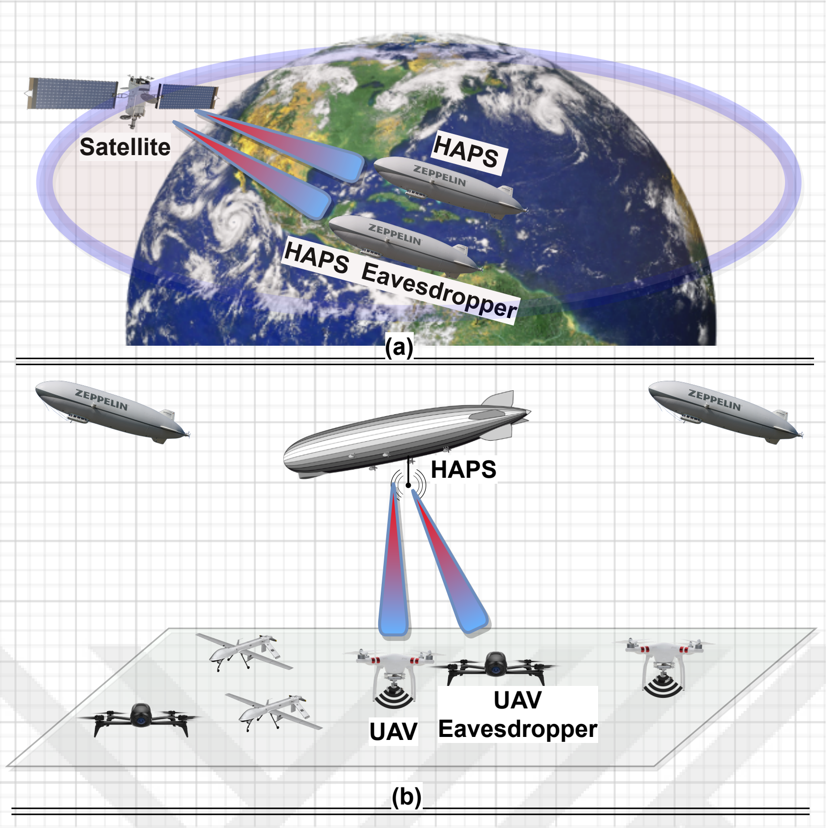

Figure 6.1 : (a) Eavesdropping in space, (b) Eavesdropping on the ground level.

In the second scenario, we assume a HAPS node sending secret information to a UAV system located near the ground while a UAV eavesdropper is trying to intercept the confidential information. In both scenarios, the communication is conducted through FSO links which are modeled with EW fading, which is suitable for different aperture sizes D_G.

For both models, the received signal at node j, $j \in \{D,E\}$ can be given by $y_j = \sqrt{P_j} I_j f_j s + n_j$, where s indicates the transmitted symbol with unit energy. P_j represents the transmit power, n_j is the zero-mean AWGN with N_0 one-sided noise PSD, I_j denotes the received irradiance of the channel, which results from the atmospheric turbulence. Accordingly, the instantaneous received SNR at node j can be given as

$$\gamma_j = \frac{P_j}{N_0} f_j^2 I_j^2 = \overline{\gamma}_j I_j^2, \tag{6.1}$$

where f_j is the attenuation depending on the altitude of the flying platform and $\overline{\gamma}_j$ is the average SNR at node j and $E[I_j^2] = 1$.

Considering the EW distribution for the links between S and the receivers, the PDF of the FSO link can be expressed as

$$f_{I_j}(I) = \frac{\alpha_j \beta_j}{\eta_j}\left(\frac{I}{\eta_j}\right)^{\beta_j-1} \exp\left[-\left(\frac{I}{\eta_j}\right)^{\beta_j}\right] \times \left(1-\exp\left[-\left(\frac{I}{\eta_j}\right)^{\beta_j}\right]\right)^{\alpha_j-1}, \tag{6.2}$$

and the CDF of SNR is given by [17]

$$F_{\gamma_j}(\gamma) = \sum_{\rho=0}^{\infty} \binom{\alpha_j}{\rho} (-1)^{\rho} \exp\left[-\rho\left(\frac{\gamma}{\eta_j^2 \bar{\gamma}_j}\right)^{\frac{\beta_j}{2}}\right], \tag{6.3}$$

where η_j indicates the scale parameter, α_j, β_j present the shape parameters which can be obtained by using the scintillation index ($\sigma_{I_j}^2$) [13, Sect. (12)] and the Rytov variance, which is given as

$$\sigma_{R_j}^2 = 2.25 k^{7/6} \sec^{11/6}(\xi_j) \int_{h_j^0}^{H} C_n^2(h)(h-h_j^0)^{5/6} dh, \tag{6.4}$$

where $k = \frac{2\pi}{\lambda}$ is the wave number dependent on the optical wavelength λ, ξ_j presents the zenith angle, H is the altitude of S, h_j^0 indicates the height of the flying platform above the ground level, and $C_n^2(h)$ is the refractive-index parameter which depends on altitude h and wind speed w.

6.1.1 Stratospheric attenuation

Stratospheric attenuation is one of the most dominant drawbacks which adversely affect the HAPS. Following the Beer-Lambert law, the stratospheric attenuation (f_j^{S}) can be expressed as

$$f_j^{\mathrm{S}} = \exp(-\sigma_j^{\mathrm{S}} L_j), \tag{6.5}$$

where σ_j^{S} indicates the stratospheric attenuation coefficient over the distance L_j in km.

6.1.2 Atmospheric attenuation

In the downlink optical communication, the quality of the communication can be affected and thus degraded due to adverse weather conditions and the particles including dust, gases, and aerosols that are available in the atmosphere. Furthermore, two different types of scattering can affect UAVs near ground level: geometrical scattering and Mie scattering, as detailed below.

6.1.2.1 Atmospheric attenuation due to geometrical scattering

According to Kim's model, the attenuation coefficient can be written as [19, eqn. (6)]

$$\sigma_j^{\mathrm{G}} = \frac{3.91}{V_j}\left(\frac{\lambda}{550}\right)^{-\rho_j}, \tag{6.6}$$

where ρ_j is the particle size-related exponent and V_j is defined as the visibility parameter in km depending on the liquid water content and the cloud number concentration. Therefore, the attenuation f_j^G can be obtained using the as $f_j^G = \exp(-\sigma_j^{\mathrm{G}} L_j)$.

6.1.2.2 Atmospheric attenuation due to Mie scattering

As mentioned before, the attenuation due to Mie scattering can be written as [19, eqn. (5)]

$$f_j^{\mathrm{M}} = \exp\left(-\frac{\tau}{\sin(\Theta_j)}\right), \tag{6.7}$$

where $\Theta_j = (\frac{\pi}{2} - \xi_j)$ is the elevation angle of the ground receiver and τ is the extinction ratio given in [19].

6.2 Secrecy Performance Analysis

In this section, we investigate the secrecy performance of the proposed non-terrestrial networks. More specifically, the expressions of SOP and PPSC for FSO eavesdropping are derived over EW fading channels.

6.2.1 Secrecy outage probability

As mentioned before, the SOP expression can be written as

$$\begin{aligned} P_{\mathrm{SO}} &= \Pr\left[C_s < R_s\right], \\ &= \Pr[\log_2(1+\gamma_D) - \log_2(1+\gamma_E) < R_s] \\ &= \int_0^\infty F_{\gamma_D}\left(\gamma\gamma_{th} + \gamma_{th} - 1\right) f_{\gamma_E}\left(\gamma\right) d\gamma, \\ &\simeq \int_0^\infty F_{\gamma_D}\left(\gamma\gamma_{th}\right) f_{\gamma_E}\left(\gamma\right) d\gamma, \end{aligned} \tag{6.8}$$

$$
\begin{aligned}
P_{\mathrm{SO}} &= \int_0^\infty \frac{\alpha_E\beta_E\gamma^{\frac{\beta_E}{2}-1}}{2(\eta^2\overline{\gamma}_E)^{\frac{\beta_E}{2}}} \sum_{\rho=0}^{\infty}\sum_{k=0}^{\infty}\binom{\alpha_D}{\rho}\binom{\alpha_E-1}{k}(-1)^{k+\rho}\exp\left[-\rho\left(\frac{\gamma\gamma_{th}}{\eta_D^2\overline{\gamma}_D}\right)^{\frac{\beta_D}{2}}\right] \\
&\times\exp\left[-(k+1)\Big(\frac{\gamma}{\eta_E^2\overline{\gamma}_E}\Big)^{\frac{\beta_E}{2}}\right]d\gamma \\
&= \frac{\alpha\beta}{2(\eta^2\overline{\gamma}_E)^{\frac{\beta}{2}}}\sum_{\rho=0}^{\infty}\sum_{k=0}^{\infty}\binom{\alpha}{\rho}\binom{\alpha-1}{k}(-1)^{k+\rho}\int_0^\infty \gamma^{\frac{\beta}{2}-1} \\
&\times\exp\left[-\left(\rho\left(\frac{\gamma_{th}}{\eta^2\overline{\gamma}_D}\right)^{\frac{\beta}{2}}+(k+1)\left(\frac{1}{\eta^2\overline{\gamma}_E}\right)^{\frac{\beta}{2}}\right)\gamma^{\frac{\beta}{2}}\right]d\gamma. \qquad (6.10)
\end{aligned}
$$

---

where $\gamma_{th} = 2^{2Rs}$ and γ_E is the instantaneous SNR of the eavesdropper. The PDF of γ_E can be derived from (6.3) with respect to γ as

$$
\begin{aligned}
f_{\gamma_E}(\gamma) = {} & \frac{\alpha_E\beta_E\gamma^{\frac{\beta_E}{2}-1}}{2(\eta_E^2\overline{\gamma}_E)^{\frac{\beta_E}{2}}}\sum_{k=0}^{\infty}\binom{\alpha_E-1}{k}(-1)^k \\
&\times\exp\left[-(k+1)\Big(\frac{\gamma}{\eta_E^2\overline{\gamma}_E}\Big)^{\frac{\beta_E}{2}}\right]. \qquad (6.9)
\end{aligned}
$$

Considering FSO eavesdropping, the illegitimate user needs to be located very close to the main receiver's photo-aperture to gather the information that is reflected due to atmospheric pressure, wind, temperature changes, or misalignment errors. Hence, we assume that the eavesdropper can encounter the same turbulence and atmospheric conditions as the intended receiver. Thereby, the EW fading severity parameters can set as $\beta_D = \beta_E = \beta$, $\eta_D = \eta_E = \eta$, and $\alpha_D = \alpha_E = \alpha$. Then, by substituting (6.3) and (6.9) into (6.8), the SOP expression can be obtained as given in (6.10). Thereafter, by using [58, 3.478.1] and after a few manipulations, the final expression can be obtained as

$$
\begin{aligned}
P_{\mathrm{SO}} = {} & \frac{\alpha}{(\eta^2\overline{\gamma}_E)^{\frac{\beta}{2}}}\sum_{\rho=0}^{\infty}\binom{\alpha}{\rho}(-1)^\rho\sum_{k=0}^{\infty}\binom{\alpha-1}{k}(-1)^k \\
&\times\left((k+1)\left(\frac{1}{\eta^2\overline{\gamma}_E}\right)+\rho\left(\frac{\gamma_{th}}{\eta^2\overline{\gamma}_D}\right)\right)^{-\frac{\beta}{2}}. \qquad (6.11)
\end{aligned}
$$

6.2.2 Probability of positive secrecy capacity analysis

Mathematically, the PPSC can be expressed as

$$P_{PPSC} = \Pr\Big[\log_2(1+\gamma_D) - \log_2(1+\gamma_E) > 0\Big], \tag{6.12}$$

and after some manipulations, it can be written as [42]

$$P_{PPSC} = 1 - \int_0^{\infty} F_{\gamma_D}(\gamma) f_{\gamma_E}(\gamma) d\gamma. \tag{6.13}$$

Then, by substituting (6.3) and (6.9) into (6.13) the final expression of PPSC can be obtained as

$$\begin{aligned} P_{PPSC} = 1 - &\frac{\alpha}{(\eta^2 \overline{\gamma}_E)^{\frac{\beta}{2}}} \sum_{\rho=0}^{\infty} \binom{\alpha}{\rho} (-1)^{\rho} \sum_{k=0}^{\infty} \binom{\alpha-1}{k} \\ &\times (-1)^k \left((k+1) \left(\frac{1}{\eta^2 \overline{\gamma}_E} \right) + \rho \left(\frac{\gamma_{th}}{\eta^2 \overline{\gamma}_D} \right) \right)^{-\frac{\beta}{2}}. \end{aligned} \tag{6.14}$$

6.3 Numerical Results and Discussions

In this section, we first validate the theoretical expressions with MC simulations for HAPS eavesdropping and UAV eavesdropping in terms of SOP and PPSC. Then, we investigate the impact of the system parameters on the secrecy performance of the proposed system models through numerical results. In the HAPS eavesdropping scenario, we consider an LEO satellite located at 500 km above the ground level, and the HAPS receiver and eavesdropper are located at 18 km of altitude. In UAV eavesdropping, HAPS altitude is chosen as 20 km, whereas the UAV receiver and eavesdropper are located at 200 m above ground level, affected by Mie scattering and thin cirrus cloud formation. Furthermore, the wind speed is set to $w = 65$ m/s, $\lambda = 1550$ nm, $C_0 = 1.7 \times 10^{-14}$, and the threshold rate is selected as $R_s = 0.01$ nats/s/Hz. Table 6.1 provides a summary of simulation parameters.

In Figure 6.2, we examine the impact of the zenith angle on the secrecy performance of both scenarios. It can be observed that the theoretical results are in good agreement with the MC simulations validating our theoretical analysis. Furthermore, comparing both models, it is clear that the secrecy performance of the HAPS eavesdropping outperforms UAV eavesdropping as the HAPS layer experiences lower attenuation, which results in enhanced secrecy performance. Moreover, we can observe that

Table 6.1 : Simulation parameters.

Satellite-HAPS	
Parameter	Value
Zenith angle (ξ)	70°, 80°
Satellite height (H)	500 km
HAPS altitude (h^0)	18 km
Wind speed (w)	65 m/s
Stratospheric attenuation (σ^S)	10^{-5}
Aperture size (D_G)	0 cm, 20 cm, 40 cm
HAPS-UAV	
HAPS altitude (H)	20 km
UAV altitude (h^0)	200 m
Zenith angle (ξ)	70°, 80°
Wind speed (w)	21 m/s, 30 m/s, 40 m/s
Cloud Type	Thin Cirrus

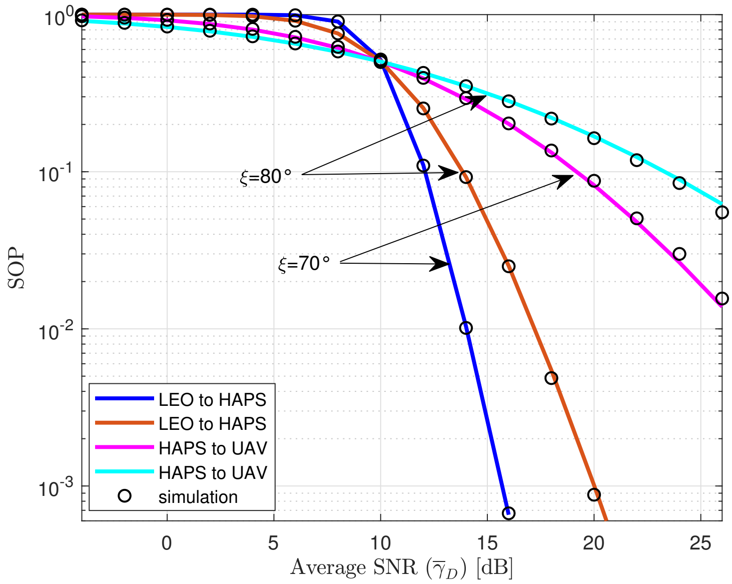

Figure 6.2 : SOP performance of the proposed models for different zenith angles.

higher values of the zenith angle deteriorate the overall secrecy performance for both scenarios.

Figure 6.3 provides the SOP performance for the case of HAPS eavesdropping by considering different aperture sizes for the legitimate receiver. As illustrated in this figure, increasing the main receiver's aperture diameter enhances the secrecy performance as widening the aperture increases the collected information by the receiver. Furthermore, the aperture diameter has a direct impact on the scintillation index and thus helps us to mitigate the adverse effects of atmospheric turbulence.

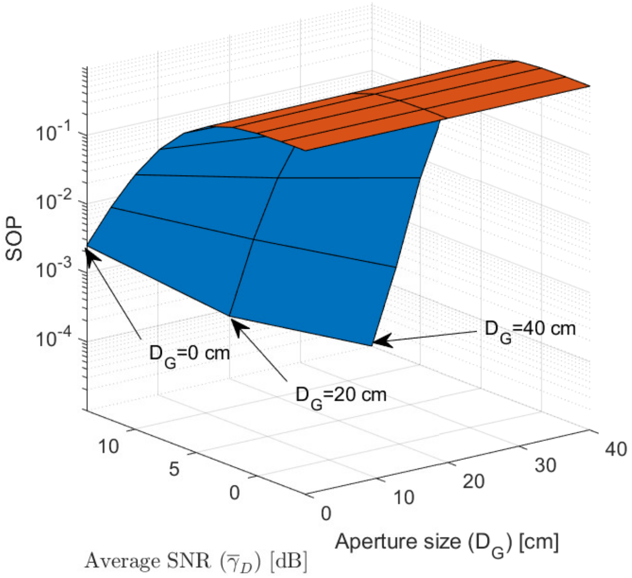

Figure 6.3 : SOP performance of HAPS eavesdropping vs. $\overline{\gamma}_D$ for different D_G.

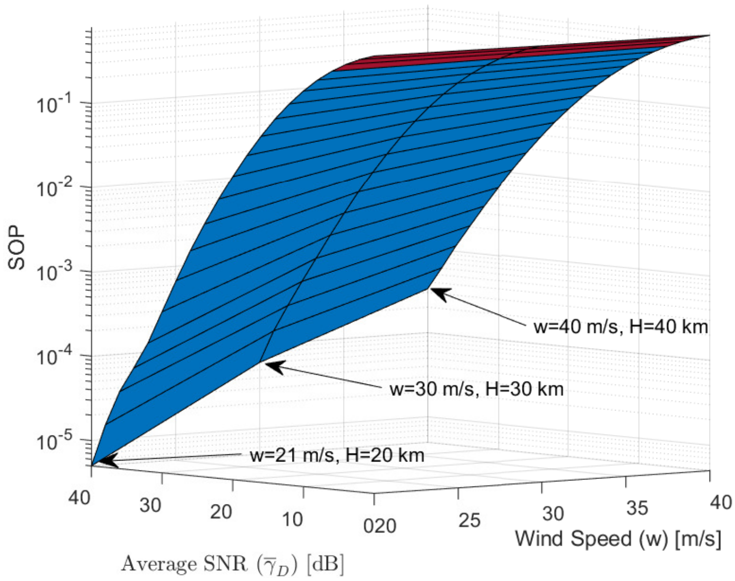

Figure 6.4 : SOP performance of the UAV eavesdropping vs. $\overline{\gamma}_D$ for different wind speeds and HAPS altitudes.

In Figure 6.4, we variate the HAPS altitude along with the wind speed level for the UAV eavesdropping. The simulation results have shown that increasing the source height has no impact on the system performance. Furthermore, when we increase the HAPS altitude, we will consider the presence of stratospheric attenuation but the latter imposes a slight degradation on the system as it is so small when compared to ground attenuation. Also, it is clear that the SOP performance can be significantly improved when the wind speed level decreases.

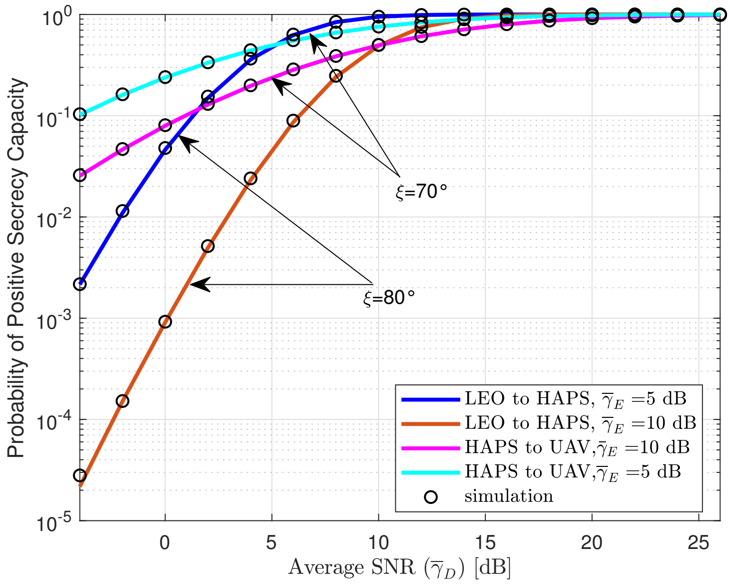

Figure 6.5 : PPSC performance the proposed models vs. $\overline{\gamma}_D$ under different $\overline{\gamma}_E$.

In Figure 6.5, we investigate the PPSC performance of the proposed models considering different $\overline{\gamma}_E$ values. In this figure, the zenith angle is set to $\xi = 80^\circ$ for HAPS eavesdropping and $\xi = 70^\circ$ for the UAV eavesdropping. It is clear from the figure that, the PPSC performance enhances as $\overline{\gamma}_E$ decreases, which shows us the high impact of $\overline{\gamma}_E$ on the secrecy performance. Furthermore, we can see the good correspondence with the MC simulations showing the effectiveness of our performance analysis.

6.3.1 Design guidelines

In this subsection, we outline the main conclusions of this study.

- According to the numerical results, the altitudes of HAPS and UAV with respect to the ground level have a direct impact on the atmospheric turbulence and attenuation in the downlink communication.

- We understand from the results that increasing the zenith angle or the wind speed deteriorates the overall secrecy performance as they aggravate the atmospheric turbulence.

- Adopting higher aperture sizes for the legitimate receiver enhances the secrecy performance as it helps to mitigate the atmospheric turbulence, and thus, improves the quality of the main channel compared to the eavesdropper channel.

6.4 Summary and Discussion

This chapter sheds light on the FSO eavesdropping on non-terrestrial downlink networks. By considering the cases of HAPS eavesdropping and UAV eavesdropping. For the proposed schemes, we obtained the closed-form expressions of PPSC and SOP. Moreover, we examined the practical effects of the proposed setups including stratospheric attenuation, geometrical scattering, and Mie scattering. In addition, we study the impact of aperture averaging, zenith angle, and wind speed levels to guarantee secure communication. The results have shown that the HAPS layer is more resistant to eavesdropping attacks.

In the next chapter, we will investigate the PLS performance of optical satellite eavesdropping, where a spacecraft attacker eavesdrops on an LEO satellite.

7. OPTICAL SATELLITE EAVESDROPPING

In the previous chapter, we studied the PLS performance of FSO eavesdropping in NTN systems by proposing two different system models. First, we considered a HAPS attacker that aims to intercept the communication between an LEO satellite and a HAPS node. Thereafter, we assumed a UAV eavesdropper that eavesdrops on communication between a HAPS node and a UAV. In this chapter, we continue with investigating the PLS in NTN systems. In this context, we introduce eavesdropping on LEO satellites. Specifically, we assume two practical eavesdropping scenarios for satellite-to-HAPS (DL) and HAPS-to-satellite (UL) optical communications, where the attacker spacecraft is located very close to the LEO satellite, within the convergence area of its optical beam, can eavesdrop on the transmitted signal or the received signal.

As mentioned before, the study presented in this chapter has been published in the following paper:

O. Ben Yahia, E. Erdogan, G. Karabulut Kurt, I. Altunbas, and H. Yanikomeroglu, "Optical Satellite Eavesdropping", IEEE Transactions on Vehicular Technology (early access), pp. 1–6, 2022.

The chapter is organized as follows: Channels and system model are presented in Section 7.1. In Section 7.2, the expressions for secrecy performance are provided. Numerical results are outlined in Section 7.3 followed with related discussion. Finally, Section 7.4 concludes the chapter.

7.1 Channels and System Model

In this work [79], we propose a novel scenario of eavesdropping attacks in space. As shown in Figure 7.1, we assume an LEO satellite S that communicates with a HAPS $\mathscr{H}$ node in the presence of a sophisticated eavesdropping spacecraft E located very close to S. We first consider S to $\mathscr{H}$ downlink communication, where E is within the convergence area of the optical beam of S so that it can eavesdrop on the transmitted

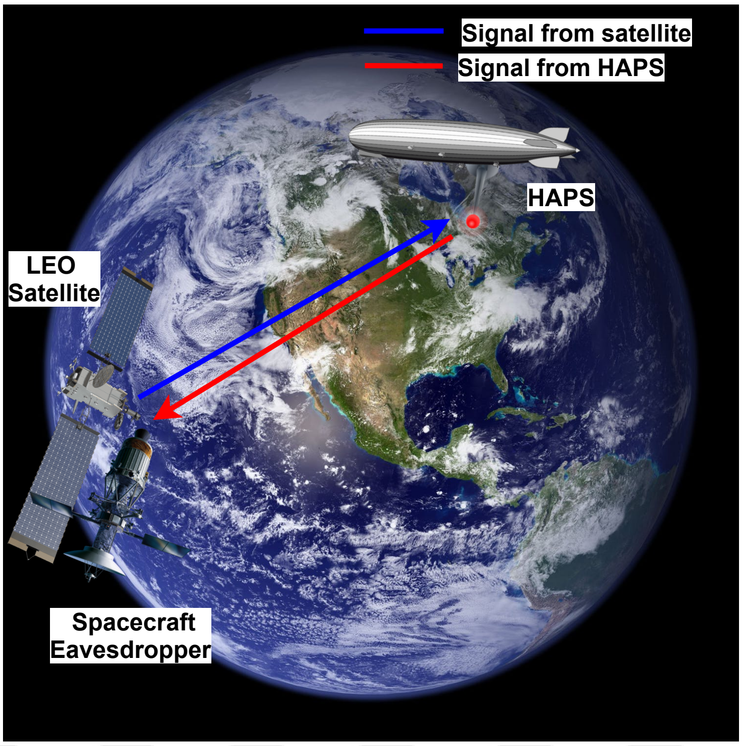

Figure 7.1 : Illustration of the satellite eavesdropping.

beam. Secondly, we consider $\mathscr{H}$ to S uplink communication, where E tries to capture the $\mathscr{H}$'s information. Due to the HAPS node's quasi-stationary position, tracking and accuracy issues, and the Doppler shift can be tolerated for the communication between S and $\mathscr{H}$. In both scenarios, E can capture only a small fraction r_e of the transmitted signal, whereas the intended receiver collects more power resulting in a fraction r_b, where $r_e + r_b \leq 1$. Note that the parameters r_b and r_e depend on the aperture size of each device along with the beam divergence angle. In the analysis, we assume that the locations of satellite, HAPS, and eavesdropper spacecraft can be used to extract the channel's physical model, which is representative of the CSI [13].

For S to $\mathscr{H}$ communication scenario, the received signal at $\mathscr{H}$ can be given as $y_{\mathscr{H}} = \sqrt{r_b P_S} I_{\mathscr{H}} x_S + n_{\mathscr{H}}$ and for $\mathscr{H}$ to S communication, the received signal at S can be written similarly as $y_S = \sqrt{r_b P_{\mathscr{H}}} I_S x_{\mathscr{H}} + n_S$. For both scenarios, the received signals at E sent by node j, $j \in \{S, \mathscr{H}\}$ can be written as $y_E = \sqrt{r_e P_j} I_E x_j + n_E$. P_S, $P_{\mathscr{H}}$ denote the transmit power of S and $\mathscr{H}$ respectively, $I_{\mathscr{H}}$, I_S, I_E indicate the received irradiance at $\mathscr{H}$, S, and E respectively. x_S, $x_{\mathscr{H}}$ are the transmitted symbols with unit energy, and $n_{\mathscr{H}}$, n_S indicate the AWGN with one-sided noise power spectral density N_0. Thus, the instantaneous signal-to-noise ratio (SNR) at $\mathscr{H}$ can be given as

$$\gamma_{\mathscr{H}} = \frac{r_b P_S}{N_0} I_{\mathscr{H}}^2 = \overline{\gamma}_{\mathscr{H}} I_{\mathscr{H}}^2, \tag{7.1}$$

where $\overline{\gamma}_{\mathscr{H}} = \frac{r_b P_S}{N_0}$ defines the average SNR at $\mathscr{H}$ with $\mathbb{E}[I_{\mathscr{H}}^2] = 1$, and the instantaneous SNR at S and E can be expressed similarly after changing the subscripts as $\gamma_{\mathscr{S}} = \frac{r_b P_{\mathscr{H}}}{N_0} I_S^2 = \overline{\gamma}_S I_S^2$ and $\gamma_E = \frac{r_e P_j}{N_0} I_E^2 = \overline{\gamma}_E I_E^2$ with $\mathbb{E}[I_E^2] = \mathbb{E}[I_S^2] = 1$. We assume that the turbulence-induced fading follows EW distribution. EW fading has been shown to be the best fit for various aperture diameters for weak-to-strong turbulence levels, especially when aperture averaging is used to mitigate the impacts of turbulence and increase overall performance [19]. Hence, the probability density function (PDF) of the irradiance I for node k where $k \in \{S, \mathscr{H}, E\}$ is expressed as in [19, eqn. 11]. Furthermore, the CDF of γ_k can be expressed as [80, eqn. 9]

$$F_{\gamma_k}(\gamma) = \sum_{\rho=0}^{\infty} \binom{\alpha_k}{\rho} (-1)^{\rho} \exp\left[-\rho \left(\frac{\gamma}{\eta_k^2 \overline{\gamma}_k}\right)^{\frac{\beta_k}{2}}\right], \tag{7.2}$$

where α_k, β_k, and η_k indicate the shape parameters and the scale parameter, respectively, which depend on the scintillation index [19]. For the downlink communication, the scintillation index $\sigma_{I_{DL}}^2$ at $\mathscr{H}$ can be written as

$$\sigma_{I_{DL}}^2 = \exp\left[\frac{0.49\sigma_R^2}{(1+1.11\sigma_R^{\frac{12}{5}})^{\frac{7}{6}}} + \frac{0.51\sigma_R^2}{(1+0.69\sigma_R^{\frac{12}{5}})^{\frac{5}{6}}}\right] - 1, \tag{7.3}$$

where σ_R^2 denotes the Rytov variance given in [13, Sect. (12)] and it depends on the zenith angle $\xi_{\mathscr{H}}$ and the wind speed $w_{\mathscr{H}}$. In uplink communication, beam wander induced-pointing error has to be taken into consideration [67]. Therefore, the scintillation index $\sigma_{I_{UL}}^2$ can be written as

$$\begin{aligned} \sigma_{I_{UL}}^2 = {} & 5.95(H_p - h_0)^2 \sec^2(\xi_p) \left(\frac{2W_0}{r_0}\right)^{\frac{5}{3}} \left(\frac{\alpha_{pe}}{W_p}\right)^2 \\ & + \exp\left[\frac{0.49\sigma_{Bu}^2}{(1+(1.11+\Theta)\sigma_{Bu}^{\frac{12}{5}})^{\frac{7}{6}}} + \frac{0.51\sigma_{Bu}^2}{(1+0.69\sigma_{Bu}^{\frac{12}{5}})^{\frac{5}{6}}}\right] - 1, \end{aligned} \tag{7.4}$$

where H_p is the height of S and E, h_0 presents the HAPS altitude, and ξ_p indicates the zenith angle for uplink communication. W_0 is the beam radius at $\mathscr{H}$, the Fried's parameter r_0 depends on the wind speed w_p, α_{pe} indicates the beam wander-induced pointing errors variance, W_p is the beam size at S and E, and σ_{Bu}^2 is the Rytov variance in uplink communication [67].

7.2 Secrecy Analysis

In this section, we analyze the secrecy performance of the proposed model. More specifically, the closed-form expressions of ASC, SOP, and ST are derived for both scenarios. According to the information-theoretic definition, the secrecy capacity C_s is the maximum achievable secrecy rate that can be expressed as follows:

$$C_s = \begin{cases} \log_2(1+\gamma_j) - \log_2(1+\gamma_E) \, , \gamma_j > \gamma_E \\ \\ 0 \, , \text{otherwise}, \end{cases} \tag{7.5}$$

where γ_j denotes the instantaneous SNR of the main receiver.

7.2.1 Average secrecy capacity

In the context of PLS, ASC is an important metric for evaluating the secrecy performance of active eavesdropping.

7.2.1.1 Eavesdropping in downlink communication

In S to $\mathscr{H}$ downlink communication, we assume that E is positioned very close to S. Therefore, the turbulence-induced fading can be neglected to provide a realistic model [44]. Thus, ASC for downlink eavesdropping can be obtained by averaging the C_s as

$$\overline{C}_s = \frac{1}{\ln(2)} \mathbb{E}\Big[\ln(1+\gamma_{\mathscr{H}}) - \ln(1+\gamma_E)\Big]. \tag{7.6}$$

By using Jensen's inequality, for high SNR values, the ASC becomes

$$\begin{aligned} \overline{C}_s &\cong \frac{1}{\ln(2)} \Big[\ln\Big(1+\mathbb{E}[\gamma_{\mathscr{H}}]\Big) - \ln\Big(1+\mathbb{E}[\gamma_E]\Big)\Big] \\ &\cong \frac{1}{\ln(2)} \Big[\ln\Big(1+\frac{r_b P_S}{N_0}\Big) - \ln\Big(1+\frac{r_e P_S}{N_0}\Big)\Big]. \end{aligned} \tag{7.7}$$

7.2.1.2 Eavesdropping in uplink communication

In uplink communication, we take the turbulence-induced fading into consideration. Thereby, $\overline{C}_s$ can be expressed as [81]

$$\overline{C}_s = \frac{1}{\ln(2)} \int_0^\infty \frac{F_{\gamma_E}(\gamma)}{1+\gamma} \Big[1 - F_{\gamma_j}(\gamma)\Big] d\gamma. \tag{7.8}$$

$$
\begin{aligned}
\overline{C}_s &= \frac{1}{\ln 2} \sum_{\rho=0}^{\infty} \binom{\alpha}{\rho} (-1)^{\rho} \frac{2}{\beta} \eta^2 \overline{\gamma}_E \left(\frac{1}{\rho}\right)^{\frac{2}{\beta}} \int_0^{\infty} X^{\frac{2}{\beta}-1} G_{1,1}^{1,1}\left(\eta^2 \overline{\gamma}_E \left(\frac{X}{\rho}\right)^{\frac{2}{\beta}} \middle| \begin{matrix} 0 \\ 0 \end{matrix} \right) \\
&\times G_{0,1}^{1,0}\left(X \middle| \begin{matrix} - \\ 0 \end{matrix} \right) dX - \frac{1}{\ln 2} \sum_{\rho=0}^{\infty} \sum_{t=0}^{\infty} (-1)^{\rho+t} \binom{\alpha}{\rho} \binom{\alpha}{t} \frac{2}{\beta} \left(\frac{1}{\rho A + tB}\right)^{\frac{2}{\beta}} \\
&\times \int_0^{\infty} Y^{\frac{2}{\beta}-1} G_{1,1}^{1,1}\left(\left(\frac{Y}{\rho A + tB}\right)^{\frac{2}{\beta}} \middle| \begin{matrix} 0 \\ 0 \end{matrix} \right) \times G_{0,1}^{1,0}\left(Y \middle| \begin{matrix} - \\ 0 \end{matrix} \right) dY \\
&= \frac{1}{\ln 2} \frac{2 \times 2^{\frac{2}{\beta}-\frac{1}{2}}}{(2\pi)^{\beta-\frac{1}{2}}} \eta^2 \overline{\gamma}_S \sum_{t=1}^{\infty} \binom{\alpha}{t} (-1)^{t+1} \left(\frac{1}{t}\right)^{\frac{2}{\beta}} \\
&\times G_{\beta+2,\beta}^{\beta,\beta+2}\left(4 \times \left(\frac{\eta^2 \overline{\gamma}_S}{t^{\frac{2}{\beta}}}\right)^{\beta} \middle| \begin{matrix} \Delta(\beta,0), \frac{1-(2/\beta)}{2}, \frac{2-(2/\beta)}{2} \\ \Delta(\beta,0) \end{matrix} \right) \\
&- \frac{1}{\ln 2} \frac{2 \times 2^{\frac{2}{\beta}-\frac{1}{2}}}{(2\pi)^{\beta-\frac{1}{2}}} \times \sum_{\rho=1}^{\infty} \sum_{t=1}^{\infty} \binom{\alpha}{\rho} \binom{\alpha}{t} (-1)^{\rho+t+2} \left(\frac{1}{\rho A + tB}\right)^{\frac{2}{\beta}} \\
&\times G_{\beta+2,\beta}^{\beta,\beta+2}\left(4 \times \left(\frac{1}{\rho A + tB}\right)^{2} \middle| \begin{matrix} \Delta(\beta,0), \frac{1-(2/\beta)}{2}, \frac{2-(2/\beta)}{2} \\ \Delta(\beta,0) \end{matrix} \right). \qquad (7.10)
\end{aligned}
$$

By substituting $F_{\gamma_E}(\gamma)$ and $F_{\gamma_j}(\gamma)$ in (7.8), the ASC for uplink communication becomes

$$
\begin{aligned}
\overline{C}_s = & \sum_{\rho=0}^{\infty} \left(\begin{matrix} \alpha_E \\ \rho \end{matrix} \right) (-1)^{\rho} \int_0^{\infty} \frac{1}{1+\gamma} \exp\left[-\rho \left(\frac{\gamma}{\eta_E^2 \overline{\gamma}_E} \right)^{\frac{\beta_E}{2}} \right] d\gamma \\
& - \sum_{\rho=0}^{\infty} \sum_{t=0}^{\infty} (-1)^{\rho} (-1)^{t} \left(\begin{matrix} \alpha_E \\ \rho \end{matrix} \right) \left(\begin{matrix} \alpha_S \\ t \end{matrix} \right) \int_0^{\infty} \frac{1}{1+\gamma} \\
& \times \exp\left[-\left(\rho \left(\frac{\gamma}{\eta_E^2 \overline{\gamma}_E} \right)^{\frac{\beta_E}{2}} + t \left(\frac{\gamma}{\eta_S^2 \overline{\gamma}_S} \right)^{\frac{\beta_S}{2}} \right) \right] d\gamma. \qquad (7.9)
\end{aligned}
$$

In $\mathscr{H}$ to S communication, E should be located very close to the main receiver's photo aperture to gather some of the reflected signals due to atmospheric pressure or misalignment caused by the pointing errors. Thus, we assume that E encounters the same fading conditions as the intended receiver. Based on this assumption, we consider that $\beta_S = \beta_E = \beta$, $\alpha_S = \alpha_E = \alpha$, and $\eta_S = \eta_E = \eta$. Thereafter, using the following transformations $(1+x)^a = \frac{1}{\Gamma(-a)} G_{1,1}^{1,1}\left(x \middle| \begin{matrix} a+1 \\ 0 \end{matrix} \right)$, where $G_{p,q}^{m,n}\left(x \middle| \begin{matrix} a_1,\ldots,a_p \\ b_1,\ldots,b_q \end{matrix} \right)$ denotes the Meijer G-function, and $\exp(-bx) = G_{0,1}^{1,0}\left(bx \middle| \begin{matrix} - \\ 0 \end{matrix} \right)$ into (7.9), and by changing the variables as $X = \rho \left(\frac{\gamma}{\eta^2 \overline{\gamma}_E} \right)^{\frac{\beta}{2}}$, and with the aid of [53, eqn. 07.34.21.0013.01], the final expression of ASC can be formulated as in (7.10) given at the top of the next page.

In (7.10), the constants A and B show $A=\left(\frac{1}{\eta^2\overline{\gamma}_E}\right)^{\frac{\beta}{2}}$, $B=\left(\frac{1}{\eta^2\overline{\gamma}_S}\right)^{\frac{\beta}{2}}$, and $Y=\gamma^{\frac{\beta}{2}}\Bigg(\rho A+tB\Bigg)$.

7.2.2 Secrecy outage probability

7.2.2.1 Eavesdropping in downlink communication

As mentioned above, in downlink communication, E is located very close to S and the SOP expression can be written as

$$\begin{aligned} P_{\mathrm{SO}} &= \Pr[\gamma_{\mathscr{H}} \le 2^{R_s}+2^{R_s}\overline{\gamma}_E-1] \\ &= F_{\gamma_{\mathscr{H}}}(2^{R_s}+2^{R_s}\overline{\gamma}_E-1). \end{aligned} \tag{7.11}$$

Thereby, by using (7.11) P_{SO} can be obtained as

$$P_{\mathrm{SO}}=\sum_{\rho=0}^{\infty}\binom{\alpha_{\mathscr{H}}}{\rho}(-1)^{\rho}\exp\left[-\rho\left(\frac{2^{R_s}+2^{R_s}\overline{\gamma}_E-1}{\eta_{\mathscr{H}}^2\overline{\gamma}_{\mathscr{H}}}\right)^{\frac{\beta_{\mathscr{H}}}{2}}\right]. \tag{7.12}$$

7.2.2.2 Eavesdropping in uplink communication

For uplink communication, since we take into account turbulence-induced fading, the expression SOP can be written as [74]

$$\begin{aligned} P_{\mathrm{SO}} &= \int_0^{\infty} F_{\gamma_j}\left(\gamma\gamma_{th}+\gamma_{th}-1\right) f_{\gamma_E}\left(\gamma\right) d\gamma \\ &\simeq \int_0^{\infty} F_{\gamma_j}\left(\gamma\gamma_{th}\right) f_{\gamma_E}\left(\gamma\right) d\gamma. \end{aligned} \tag{7.13}$$

Thus, for uplink eavesdropping, the SOP is expressed on the basis of (7.13), where the PDF of γ_E can be derived from (7.2) with respect to γ as

$$\begin{aligned} f_{\gamma_E}(\gamma) = & \frac{\alpha_E\beta_E\gamma^{\frac{\beta_E}{2}-1}}{2(\eta_E^2\overline{\gamma}_E)^{\frac{\beta_E}{2}}}\sum_{q=0}^{\infty}\left(\begin{array}{c}\alpha_E-1\\ q\end{array}\right)(-1)^q \\ & \times\exp\left[-(q+1)\left(\frac{\gamma}{\eta_E^2\overline{\gamma}_E}\right)^{\frac{\beta_E}{2}}\right]. \end{aligned} \tag{7.14}$$

Then, by substituting (7.2) and (7.14) into (7.13), we obtain the equation given on the top of the next page as (7.15). Finally, after some mathematical derivations and by

$$
\begin{aligned}
P_{\mathrm{SO}} &= \int_0^\infty \frac{\alpha_E \beta_E \gamma^{\frac{\beta_E}{2}-1}}{2(\eta^2 \overline{\gamma}_E)^{\frac{\beta_E}{2}}} \sum_{\rho=0}^{\infty} \sum_{q=0}^{\infty} \binom{\alpha_S}{\rho} \binom{\alpha_E - 1}{q} (-1)^{q+\rho} \exp\left[-\rho \left(\frac{\gamma \gamma_{th}}{\eta_S^2 \overline{\gamma}_S}\right)^{\frac{\beta_S}{2}}\right] \\
&\quad \times \exp\left[-(q+1)\left(\frac{\gamma}{\eta_E^2 \overline{\gamma}_E}\right)^{\frac{\beta_E}{2}}\right] d\gamma \\
&= \frac{\alpha \beta}{2(\eta^2 \overline{\gamma}_E)^{\frac{\beta}{2}}} \sum_{\rho=0}^{\infty} \sum_{q=0}^{\infty} \binom{\alpha}{\rho} \binom{\alpha - 1}{q} (-1)^{q+\rho} \int_0^\infty \gamma^{\frac{\beta}{2}-1} \\
&\quad \times \exp\left[-\left(\rho \left(\frac{\gamma_{th}}{\eta^2 \overline{\gamma}_S}\right)^{\frac{\beta}{2}} + (q+1)\left(\frac{1}{\eta^2 \overline{\gamma}_E}\right)^{\frac{\beta}{2}}\right) \gamma^{\frac{\beta}{2}}\right] d\gamma. \qquad (7.15)
\end{aligned}
$$

using [58, 3.478.1], the final expression of SOP can be written as

$$
\begin{aligned}
P_{\mathrm{SO}} = \frac{\alpha}{(\eta^2 \overline{\gamma}_E)^{\frac{\beta}{2}}} \sum_{\rho=0}^{\infty} \binom{\alpha}{\rho} (-1)^{\rho} \sum_{q=0}^{\infty} \binom{\alpha - 1}{q} (-1)^{q} \\
\times \left(\rho \left(\frac{\gamma_{th}}{\eta^2 \overline{\gamma}_S}\right) + (q+1)\left(\frac{1}{\eta^2 \overline{\gamma}_E}\right)\right)^{-\frac{\beta}{2}}. \qquad (7.16)
\end{aligned}
$$

7.2.3 Secrecy throughput

Another metric to evaluate the secrecy performance of the proposed system is ST. This metric is exploited to characterize the overall efficiency of achieving reliable and secure transmission [82]. Mathematically, it can be written as

$$
ST = R_s(1 - P_{\mathrm{SO}}). \qquad (7.17)
$$

The expressions of ST for uplink and downlink communication can be easily obtained by substituting (7.12) and (7.16) in (7.17).

7.3 Numerical Results and Discussion

In this section, we evaluate the secrecy performance of satellite eavesdropping for the proposed models. For both scenarios, we consider the same parameters. The LEO satellite orbits at an altitude of 500 km, while the HAPS is located at 18 km. The zenith angles are set to $\xi_S = \xi_{\mathscr{H}} = 70^\circ$, the wind speed is given as $w_S = w_{\mathscr{H}} = 65$ m/s as we consider non-static stratospheric winds, and the secrecy rate is set as $R_s = 0.01$ bit/s/Hz for SOP simulations.

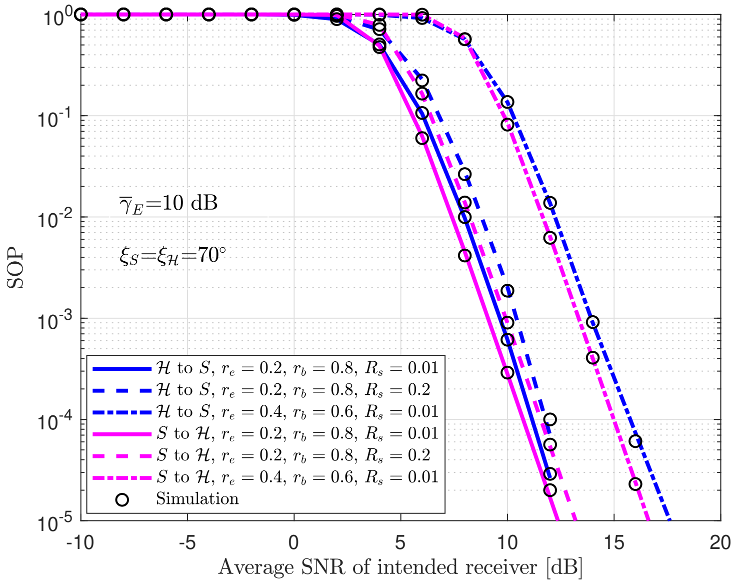

Figure 7.2 : SOP performance for different fractions of received power and different R_s.

In Figure 7.2, the SOP performance for both scenarios is plotted as a function of the SNR of the legitimate receiver. The eavesdropping average SNR is set to $\overline{\gamma}_E = 10$ dB. As we can see, the secrecy performance of the S to $\mathscr{H}$ communication is slightly better than that of $\mathscr{H}$ to S communication. This can be explained by the fact that when the illegitimate receiver approaches the receiver, it can collect more information as more beams can be reflected due to the greater distance. Moreover, for both scenarios, we can observe that the performance decreases as the fraction of the leaked power r_e received by the eavesdropper increases. Furthermore, as shown in the figure, increasing the secrecy rate R_s deteriorates the SOP performance. In addition, we can see the agreement of the theoretical expressions with the MC simulations.

In Figure 7.3, we see the ASC performance for both scenarios. As the figure shows, by increasing the average SNR of the eavesdropper $\overline{\gamma}_E$ or decreasing the amount of power captured by the legitimate receiver, the overall secrecy performance degrades. Furthermore, for the S to $\mathscr{H}$ communication, we assume that the eavesdropper has a stronger SNR, as it is located very close to the LEO satellite and does not experience turbulence-induced fading effects. Additionally, the analytical expressions match perfectly the MC simulations, as seen in the figure. Finally, we can observe that perfect secrecy is achieved when the average SNR of the intended receiver is higher than the SNR of the eavesdropper.

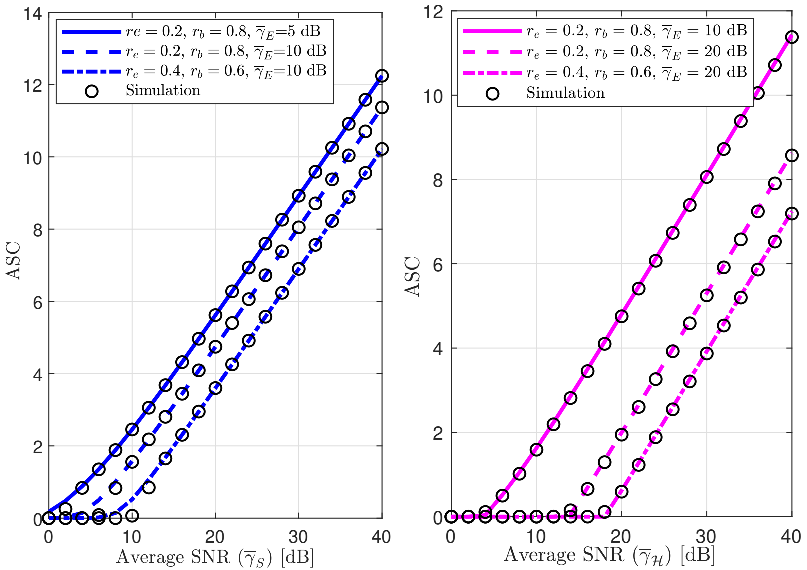

(a) $\mathcal{H}$ to S (b) S to $\mathcal{H}$

Figure 7.3 : ASC performance of both scenarios for different $\overline{\gamma}_E$ and different fractions of received power.

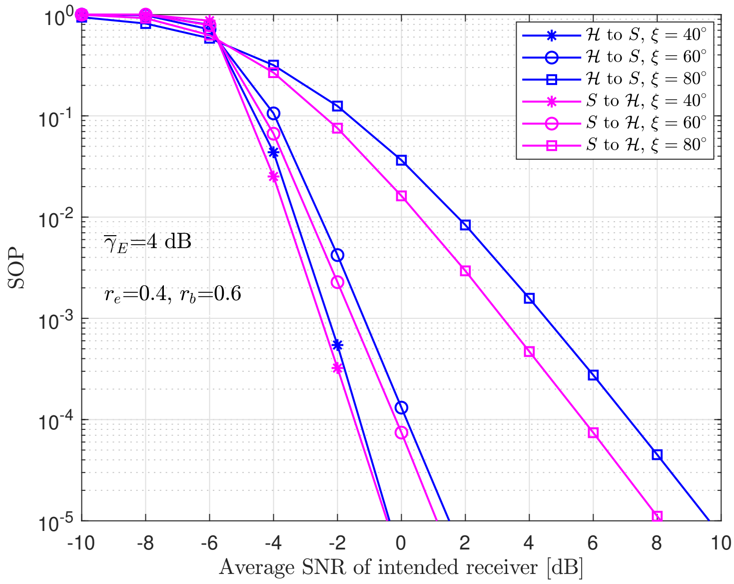

Figure 7.4 : SOP performance of the proposed models under different ξ.

Figure 7.4 shows the impact of the zenith angle on the proposed satellite eavesdropping scenarios. We set $\overline{\gamma}_E = 4$ dB and the fraction of power received by E as $r_e = 0.1$. As we can see, increasing the zenith angle decreases the amount of information that is captured by the legitimate receiver and leaked to the eavesdropper. Furthermore, the fluctuation in the signal is significant for a higher zenith angle. Thus, we conclude that there is a huge loss of performance. Moreover, as seen in the figure, for lower zenith angle, the SOP performance is almost the same for both scenarios, and the simulation results reveal that the scintillation indexes are equals. However, when increasing the zenith angle to 80°, we can see 2 dB difference between the two curves. Also, the impact of beam wander increases with increasing zenith angle.

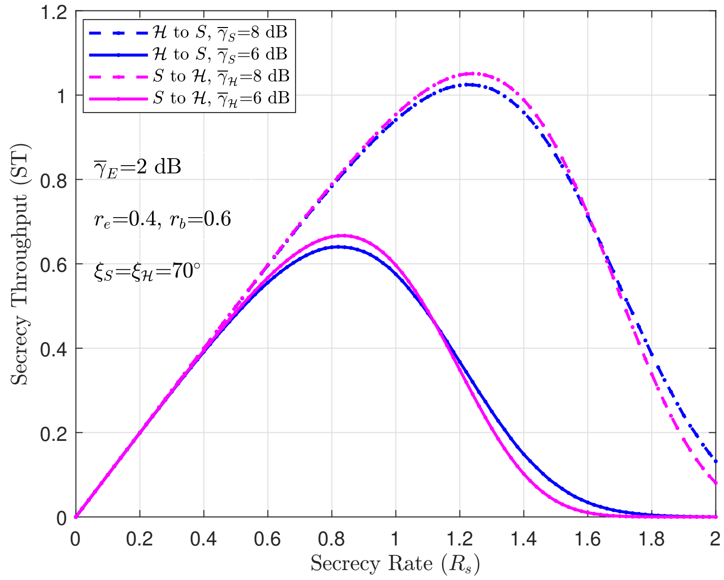

Figure 7.5 : ST performance of the proposed models vs. R_s.

Figure 7.5 evaluates the ST versus the target secrecy rate R_s for the proposed models for different average SNR levels of the intended receiver. In all cases, the average SNR of the spacecraft is set to 2 dB. As can be observed, the ST increases as R_s increases to a certain value and then decreases. This is due to the dependency of ST on R_s. The ST increases when the R_s is relatively low. However, when R_s exceeds a particular threshold value, the system cannot afford reliability and security. Furthermore, it is observed that the S to $\mathscr{H}$ downlink communication performs slightly better than $\mathscr{H}$ to S uplink scenario at lower R_s. However, after a particular value of R_s, the uplink scenario outperforms the downlink communication. Finally, as expected, increasing the average SNR of the intended receiver improves the ST performance.

Our main observations from the numerical results can be summarized as follows:

- Increasing the zenith angle between the HAPS node and the satellite decreases the overall performance.
- In the uplink scenario, the eavesdropper spacecraft can collect more information as more beams can be reflected due to the greater distance.

- The fluctuations in the signal caused by atmospheric conditions have a direct impact on the secrecy performance.
- The SNR of the eavesdropper and the amount of power leaked to the eavesdropper are critical parameters to provide secure communication.
- From ST point view, it is observed that the system reliability and secrecy are compromised after a certain value of secrecy rate R_s.

These observations can be used to provide relevant insights about the proposed scheme, allowing a system designer to gain an idea about the overall performance, especially, as we are considering random channel characteristics.

7.4 Summary and Discussion

This work has introduced the satellite eavesdropping approach, where a spacecraft eavesdrops on an LEO satellite. Specifically, we assumed an LEO satellite communicating with a HAPS node in the presence of an attacker spacecraft located very close to the LEO satellite. The unified expressions of SOP and ASC were derived in closed-form assuming EW fading. The expressions obtained were validated with MC simulations. In addition, the simulation results showed that satellite-to-HAPS downlink communication is more secure. It was also shown that increasing the leaked beam collected by the eavesdropping spacecraft deteriorated the secrecy performance. We observed that turbulence-induced fading highly affected the secrecy performance.

The main conclusions of the thesis and the future work directions are presented in the next chapter.

8. CONCLUSIONS

The contributions of this thesis are summarized in this chapter, along with discussions of the main findings. Insights for future NTN systems are also presented based on accomplished works and comprehensive literature research.

8.1 Summary and Contributions

This thesis comprises two main concepts, namely, investigating the physical layer of RF and FSO channels for NTNs from a communication perspective and evaluating, and characterizing the security performance considering random channel behavior without providing any insights on the eavesdropper's capability in successfully decoding the transmitted information.

The major part of the thesis is compromised of studying the behavior and the characteristics of both RF and FSO communications during the propagation through the atmosphere while considering different architectures for future networks. Hence, the thesis provides significant contributions to the literature by providing novel system models and novel expressions to evaluate the performance of the proposed models.

In the first part of the thesis, we have investigated the hybrid RF/FSO communication for two different downlink unicast scenarios motivated by the complementary behavior of both channels. In the former, we have considered single-hop communication, where an LEO satellite is communicating with a GS through hybrid RF/FSO communication. In the proposed approach, the LEO satellite can switch between FSO and RF links according to the weather status collected from the satellite's sensors and used for context awareness. In the latter, we have assumed that the direct communication between the LEO satellite and the GS may be unavailable due to barriers or huge attenuation between them. Therefore, we have proposed a dual-hop multi-HAPS communication. Based on the quality of the CSI feedback from the HAPS nodes, the LEO satellite selects the HAPS node providing the best channel characteristics. For both system models, we have investigated outage and asymptotic analysis for different weather conditions. It was shown that the proposed strategies perform better than the other existing models. Thereafter, we have studied the multicast services for HAPS-aided mixed RF/FSO/RF and satellite-aided mixed RF/FSO/FSO/RF communications. For the proposed strategies, we have provided error and outage analysis. It was observed that there is a trade-off between energy efficiency and OP.

In the second part, we have studied the security performance of NTN systems. First, we have discussed the RF eavesdropping on the ground for dual-hop HAPS-aided downlink SatCom. Thereafter, we studied the PLS for NTN systems by proposing three different practical scenarios of FSO eavesdropping. The simulation results have revealed that the secrecy performance is directly affected by the fluctuations in the signal due to atmospheric conditions.

To summarize, channel modeling and the radio propagation environment must be carefully designed to satisfy the envisioned quality of service and security needs of future wireless networks.

8.2 Future Works

In this section, we provide future work directions as an extension to the analysis discussed in this thesis.

From the communication perspective, our future works can be summarised as follows:

- As RF and FSO require different power levels, power allocation for hybrid RF/FSO weather-based strategy can be studied considering practical power levels.
- The performance of hybrid RF/FSO can be extended to multicast scenarios. In addition, the secrecy performance for hybrid RF/FSO communication in NTN systems can be carried out.
- Considering the system models presented in Chapter 4, optimal power allocation at the source and the HAPS can be studied to further improve the outage performance.
- The use of HAPS as an intermediary node allowing LEO satellite to communicate directly with mobile phones can be a promising approach for mobile communications by offering advantages in terms of link budget and coverage.

From the security point of view, the future works can be summarised as follows:

- Secrecy performance analysis for multicast services can be studied to understand the performance of the considered system from a security perspective.
- Propose some PLS techniques against eavesdroppers to improve the secrecy performance of NTN systems and favor the communication between legitimate users.
- Moreover, security can be enhanced by assuming a cross-layer framework while considering cryptographic techniques and PLS techniques at the same time.

REFERENCES

[1] **Rinaldi, F.**, **Maattanen, H.L.**, **Torsner, J.**, **Pizzi, S.**, **Andreev, S.**, **Iera, A.**, **Koucheryavy, Y. and Araniti, G.** (2020). Non-Terrestrial Networks in 5G & Beyond: A Survey, *IEEE Access*, *8*, 165178–165200.

[2] **3GPP** (Jan. 2020). Solutions for NR to support Non-Terrestrial Networks (NTN), document TR 38.821, Release 16, `[Online].Available:https://www.3gpp.org`.

[3] **Alam, M.S.**, **Karabulut Kurt, G.**, **Yanikomeroglu, H.**, **Zhu, P. and Dào, N.D.** (2021). High Altitude Platform Station Based Super Macro Base Station Constellations, *IEEE Communications Magazine*, *59*(1), 103–109.

[4] **ITU** (2016). Radio regulations articles, International Telecommunication Union, Recommendation.

[5] **Karabulut Kurt, G.**, **Khoshkholgh, M.G.**, **Alfattani, S.**, **Ibrahim, A.**, **Darwish, T.S.J.**, **Alam, M.S.**, **... and Yongacoglu, A.** (2021). A Vision and Framework for the High Altitude Platform Station (HAPS) Networks of the Future, *IEEE Communications Surveys Tutorials*, *23*(2), 729–779.

[6] **Fidler, F.**, **Knapek, M.**, **Horwath, J. and Leeb, W.R.** (2010). Optical communications for high-altitude platforms, *IEEE J. Sel. Topics Quantum Electron.*, *16*(5), 1058–1070.

[7] **Giggenbach, D.**, **Purvinskis, R.**, **Werner, M. and Holzbock, M.** (2002). Stratospheric optical inter-platform links for high altitude platforms, *Int. Commun. Satellite Systems Conf. and Exhibit*, p.1910.

[8] **Jiang, W.**, **Han, B.**, **Habibi, M.A. and Schotten, H.D.** (2021). The Road Towards 6G: A Comprehensive Survey, *IEEE Open J. of the Commun. Society*, *2*, 334–366.

[9] **Vishwakarma, N. and R, S.** (2021). Capacity Analysis of Adaptive Combining for Hybrid FSO/RF Satellite Communication System, *National Conference on Communications (NCC)*, pp.1–6.

[10] **Michailidis, E.T.**, **Nomikos, N.**, **Bithas, P.**, **Vouyioukas, D. and Kanatas, A.G.** (2018). Outage probability of triple-hop mixed RF/FSO/RF stratospheric communication systems, *IEEE Int. Conf. on Adv. in Satellite and Space Commun. (SPACOMM)*, pp.1–6.

[11] **Erdogan, E.** (2019). On the performance of cognitive underlay RF/FSO communication systems with limited feedback, *Optics Communications*, *444*, 87–92.

[12] **Arum, S.C.**, **Grace, D. and Mitchell, P.D.** (2020). A review of wireless communication using high-altitude platforms for extended coverage and capacity, *Computer Communications*, *157*, 232–256.

[13] **Andrews, L.C. and Phillips, R.L.** (2005). Laser beam propagation through random media (SPIE Press Monograph)., Bellingham, WA, USA: SPIE.

[14] **Nadeem, F.**, **Kvicera, V.**, **Awan, M.S.**, **Leitgeb, E.**, **Muhammad, S.S. and Kandus, G.** (2009). Weather effects on hybrid FSO/RF communication link, *IEEE J. Sel. Areas Commun.*, *27*(9), 1687–1697.

[15] **Kaushal, H. and Kaddoum, G.** (2016). Optical communication in space: Challenges and mitigation techniques, *IEEE Commun. Surveys Tuts.*, *19*(1), 57–96.

[16] **Abdi, A.**, **Lau, W.**, **Alouini, M.S. and Kaveh, M.** (2003). A new simple model for land mobile satellite channels: first- and second-order statistics, *IEEE Transactions on Wireless Communications*, *2*(3), 519–528.

[17] **Barrios Porras, R.** (May 2013). *Exponentiated Weibull Fading Channel Model in Free-Space Optical Communications under Atmospheric Turbulence*, Ph.D. dissertation, Dept. Signal Theory Commun., Univ. Politècnica de Catalunya (UPC), Barcelona, Spain.

[18] **Barrios, R. and Dios, F.** (2012). Exponentiated Weibull distribution family under aperture averaging for Gaussian beam waves, *Optics Express*, *20*(12), 13055–13064.

[19] **Erdogan, E.**, **Altunbas, I.**, **Karabulut Kurt, G.**, **Bellemare, M.**, **Lamontagne, G. and Yanikomeroglu, H.** (2021). Site Diversity in Downlink Optical Satellite Networks Through Ground Station Selection, *IEEE Access*, *9*, 31179–31190.

[20] **Arezumand, H.**, **Zamiri-Jafarian, H. and Soleimani-Nasab, E.** (2017). Outage and diversity analysis of underlay cognitive mixed RF-FSO cooperative systems, *Journal of Optical Communications and Networking*, *9*(10), 909–920.

[21] **Soleimani-Nasab, E. and Uysal, M.** (2016). Generalized Performance Analysis of Mixed RF/FSO Cooperative Systems, *IEEE Transactions on Wireless Communications*, *15*(1), 714–727.

[22] **Ashrafzadeh, B.**, **Zaimbashi, A.**, **Soleimani-Nasab, E. and Uysal, M.** (2020). Unified performance analysis of multi-hop FSO systems over double generalized gamma turbulence channels with pointing errors, *IEEE Transactions on Wireless Communications*, *19*(11), 7732–7746.

[23] **Kazemi, H.**, **Uysal, M. and Touati, F.** (2014). Outage analysis of hybrid FSO/RF systems based on finite-state Markov chain modeling, *Int. Workshop in Optical Wireless Commun. (IWOW)*, 11–15.

[24] **Krishnan, P.** (2018). Performance analysis of hybrid RF/FSO system using BPSK-SIM and DPSK-SIM over Gamma-Gamma turbulence channel with pointing errors for smart city applications, *IEEE Access*, *6*, 75025–75032.

[25] **Bag, B.**, **Das, A.**, **Ansari, I.S.**, **Prokeš, A.**, **Bose, C. and Chandra, A.** (2018). Performance analysis of hybrid FSO systems using FSO/RF-FSO link adaptation, *IEEE Photon. J.*, *10*(3), 1–17.

[26] **Bag, B.**, **Das, A.**, **Bose, C. and Chandra, A.** (2019). Hybrid FSO/RF-FSO Systems over Generalized Málaga Distributed Channels with Pointing Errors, *European Signal Process. Conf. (EUSIPCO)*, pp.1–5.

[27] **Amirabadi, M.A. and Vakili, V.T.** (2019). A novel hybrid FSO/RF communication system with receive diversity, *Optik*, *184*, 293–298.

[28] **Sundharam, V. and Johari, S.** (2018). Selection Combining in Hybrid RF/FSO Systems for IM/DD and Heterodyne Detection in Varying Weather Conditions, *Micro-Electronics and Telecom Eng (ICMETE)*, pp.286–291.

[29] **Ma, J.**, **Li, K.**, **Tan, L.**, **Yu, S. and Cao, Y.** (2015). Performance analysis of satellite-to-ground downlink coherent optical communications with spatial diversity over Gamma–Gamma atmospheric turbulence, *Applied optics*, *54*(25), 7575–7585.

[30] **Siddharth, M.**, **Shah, S. and R., S.** (2020). Outage Analysis of Adaptive Combining Scheme for Hybrid FSO/RF Communication, *IEEE National Conf. on Commun. (NCC)*, pp.1–6.

[31] **Shah, S.**, **Siddharth, M.**, **Vishwakarma, N.**, **Swaminathan, R. and Madhukumar, A.S.** (2021). Adaptive-Combining-Based Hybrid FSO/RF Satellite Communication With and Without HAPS, *IEEE Access*, *9*, 81492–81511.

[32] **Swaminathan, R.**, **Sharma, S. and MadhuKumar, A.** (2020). Performance Analysis of HAPS-Based Relaying for Hybrid FSO/RF Downlink Satellite Communication, *Veh. Technol. Conf. (VTC2020-Spring)*, IEEE, pp.1–5.

[33] **Swaminathan, R.**, **Sharma, S.**, **Vishwakarma, N. and Madhukumar, A.** (2021). HAPS-based Relaying for Integrated Space-Air-Ground Networks with Hybrid FSO/RF Communication: A Performance Analysis, *IEEE Trans. Aerosp. Electron. Syst.*, *17*, 1–17.

[34] **Wang, Z.**, **Liu, Q.**, **Li, M. and Kellerer, W.** (2019). Energy Efficient Analog Beamformer Design for mmWave Multicast Transmission, *IEEE Transactions on Green Communications and Networking*, *3*(2), 552–564.

[35] **ITU** (2003). Propagation data required for the design of Earth-space systems operating between 20 THz and 375 THz, International Telecommunication Union, Recommendation P.1622.

[36] **Araniti, G.**, **Orsino, A.**, **Cosmas, J.**, **Molinaro, A. and Iera, A.** (2016). A low computational-cost subgrouping multicast scheme for emerging 5G-satellite networks, *2016 IEEE International Symposium on Broadband Multimedia Systems and Broadcasting (BMSB)*, pp.1–6.

[37] **Tian, H.**, **Xu, Y.**, **Xie, W.**, **Yu, J. and Song, L.** (2010). Outage probability analysis of opportunistic cooperative multicast based on coded cooperation, *2010 IEEE 12th International Conference on Communication Technology*, pp.1035–1038.

[38] **Lee, I.**, **Lee, H. and Choi, H.** (2013). Exact Outage Probability of Relay Selection in Decode-and-Forward Based Cooperative Multicast Systems, *IEEE Communications Letters*, *17*(3), 483–486.

[39] **Ibrahim, A. and Alfa, A.S.** (2019). Optimizing radio resources for multicasting on high-altitude platforms, *EURASIP Journal on Wireless Communications and Networking*, *2019*(1), 1–34.

[40] **Shannon, C.E.** (1949). Communication theory of secrecy systems, *The Bell system technical journal*, *28*(4), 656–715.

[41] **Wyner, A.D.** (1975). The wire-tap channel, *Bell system technical journal*, *54*(8), 1355–1387.

[42] **Boluda-Ruiz, R. and Qaraqe, K.** (2019). Effect of Misalignment Error on Secrecy Outage Capacity of FSO Communication Links, *IEEE Wireless Commun. and Netw. Conf. (WCNC)*, pp.1–7.

[43] **Ai, Y.**, **Mathur, A.**, **Verma, G.D.**, **Kong, L. and Cheffena, M.** (2020). Comprehensive Physical Layer Security Analysis of FSO Communications Over Málaga Channels, *IEEE Photonics Journal*, *12*(6), 1–17.

[44] **Lopez-Martinez, F.J.**, **Gomez, G. and Garrido-Balsells, J.M.** (2015). Physical-Layer Security in Free-Space Optical Communications, *IEEE Photon. J.*, *7*(2), 1–14.

[45] **Saber, M.J. and Sadough, S.M.S.** (2017). On secure free-space optical communications over Málaga turbulence channels, *IEEE Wireless Communications Letters*, *6*(2), 274–277.

[46] **Monteiro, M.E.P.** *et al.* (2018). Maximum secrecy throughput of MIMOME FSO communications with outage constraints, *IEEE Transactions on Wireless Communications*, *17*(5), 3487–3497.

[47] **Zhu, J.**, **Chen, Y. and Sasaki, M.** (2016). Average secrecy capacity of free-space optical communication systems with on-off keying modulation and threshold detection, *2016 International Symposium on Information Theory and Its Applications (ISITA)*, IEEE, pp.616–620.

[48] **Sikri, A.**, **Mathur, A. and Verma, G.** (2021). Secrecy Performance Enhancement of Artificial Noise Injection Scheme-based FSO Systems, *2021 IEEE 94th Vehicular Technology Conference (VTC2021-Fall)*, IEEE, pp.01–05.

[49] **Kodheli, O.**, **Lagunas, E.**, **Maturo, N.**, **Sharma, S.K.**, **Shankar, B.**, **Montoya, J.F.M.**, **... and Goussetis, G.** (2021). Satellite Communications in the New Space Era: A Survey and Future Challenges, *IEEE Communications Surveys Tutorials*, *23*(1), 70–109.

[50] **Yi, X. and Yao, M.** (2015). Free-space communications over exponentiated Weibull turbulence channels with nonzero boresight pointing errors, *Optics Express*, *23*(3), 2904–2917.

[51] **Wang, Y.**, **Wang, P.**, **Liu, X. and Cao, T.** (2018). On the performance of dual-hop mixed RF/FSO wireless communication system in urban area over aggregated exponentiated Weibull fading channels with pointing errors, *Optics Commun.*, *410*, 609–616.

[52] **Yang, F.**, **Cheng, J. and Tsiftsis, T.A.** (2014). Free-space optical communication with nonzero boresight pointing errors, *IEEE Trans. on Commun.*, *62*(2), 713–725.

[53] The Wolfram Functions Site, `http://www.wolfram.com`.

[54] **Bhatnagar, M.R. and Arti, M.K.** (2013). Performance Analysis of Hybrid Satellite-Terrestrial FSO Cooperative System, *IEEE Photonics Technology Letters*, *25*(22), 2197–2200.

[55] **Touati, A.**, **Abdaoui, A.**, **Touati, F.**, **Uysal, M. and Bouallegue, A.** (2016). On the effects of combined atmospheric fading and misalignment on the hybrid FSO/RF transmission, *J. of Optical Commun. and Netw.*, *8*(10), 715–725.

[56] **ITU** (2003). Specific Attenuation Model for Rain for use in Prediction Methods, Recommendation P.838-3.

[57] **Paris, J.F.** (2010). Closed-form expressions for Rician shadowed cumulative distribution function, *Electronics Letters*, *46*(13), 952–953.

[58] **Gradshteyn, I.S. and Ryzhik, I.M.** (2014). *Table of Integrals, Series, and Products*, Academic Press.

[59] **Ai, Y.**, **Mathur, A.**, **Cheffena, M.**, **Bhatnagar, M.R. and Lei, H.** (2019). Physical layer security of hybrid satellite-FSO cooperative systems, *IEEE Photon. J.*, *11*(1), 1–14.

[60] **Ben Yahia, O.**, **Erdogan, E.**, **Karabulut Kurt, G.**, **Altunbas, I. and Yanikomeroglu, H.** (2022). HAPS Selection for Hybrid RF/FSO Satellite Networks (early access), *IEEE Transactions on Aerospace and Electronic Systems*, 1–13.

[61] **Guo, K.**, **Lin, M.**, **Zhang, B.**, **Wang, J.B.**, **Wu, Y.**, **Zhu, W.P. and Cheng, J.** (2020). Performance Analysis of Hybrid Satellite-Terrestrial Cooperative Networks With Relay Selection, *IEEE Trans. Veh. Technol.*, *69*(8), 9053–9067.

[62] **Aragon-Zavala, A.**, **Cuevas-Ruíz, J.L. and Delgado-Penín, J.A.** (2008). *High-Altitude Platforms for Wireless Communications*, volume 5, Wiley Online Library.

[63] **ITU** (2003). Prediction methods required for the design of Earth-space systems operating between 20 THz and 375 THz, International Telecommunication Union, Recommendation P.1622.

[64] **Awan, M.S.**, **Leitgeb, E.**, **Hillbrand, B.**, **Nadeem, F.**, **Khan, M.** *et al.* (2009). Cloud attenuations for free-space optical links, *Int. Workshop on Satellite and Space Commun.*, IEEE, pp.274–278.

[65] **Johari, S. and Sundharam, V.** (2017). Performance analysis of IM/DD vs. heterodyne detection techniques of an Earth-satellite FSO link for next generation wireless communication, *IEEE Malaysia Int. Conf. on Commun. (MICC)*, pp.191–196.

[66] **El Oualkadi, A.** (2011). *Trends and Challenges in CMOS Design for Emerging 60 GHz WPAN Applications*, InTech.

[67] **Ben Yahia, O.**, **Erdogan, E. and Kurt, G.K.** (2022). HAPS-assisted Hybrid RF-FSO Multicast Communications: Error and Outage Analysis, *IEEE Transactions on Aerospace and Electronic Systems (early access)*, 1–13.

[68] **Vuong, D.P.**, **Dao, M.Q. and Le, D.K.** (2018). Resource Allocation With Minimum Outage Probability in Multicarrier Multicast Systems, *IEEE Access*, *6*, 31191–31202.

[69] **Wang, X.**, **Tao, M. and Xu, Y.** (2014). Outage Analysis of Cooperative Secrecy Multicast Transmission, *IEEE Wireless Communications Letters*, *3*(2), 161–164.

[70] **Fidler, D.F.** (September 2007). *Optical Communications from High-Altitude Platforms*, Ph.D. dissertation, Vienna University of Technology, Vienna, Austria.

[71] **Adamchik, V. and Marichev, O.** (1990). The algorithm for calculating integrals of hypergeometric type functions and its realization in REDUCE system, *Proceedings of the international symposium on Symbolic and algebraic computation*, pp.212–224.

[72] **Zhang, R.**, **Li, Y.**, **Wang, C.X.**, **Ruan, Y. and Zhang, H.** (2017). Energy efficiency of relay aided D2D communications underlaying cellular networks, *2017 IEEE 28th Annual International Symposium on Personal, Indoor, and Mobile Radio Communications (PIMRC)*, pp.1–5.

[73] **Kolev, D.R. and Toyoshima, M.** (2017). Satellite-to-ground optical communications using small optical transponder (SOTA)-received-power fluctuations, *Optics Express*, *25*(23), 28319–28329.

[74] **Ben Yahia, O.**, **Erdogan, E. and Karabulut Kurt, G.** (2021). On the Use of HAPS to Increase Secrecy Performance in Satellite Networks, *IEEE Int. Conf. on Commun. Workshops (ICC Workshops)*, pp.1–6.

[75] **Guo, K.**, **Lin, M.**, **Zhang, B.**, **Ouyang, J. and Zhu, W.P.** (2018). Secrecy performance of satellite wiretap channels with multi-user opportunistic scheduling, *IEEE Wireless Commun. Lett.*, *7*(6), 1054–1057.

[76] **Bloch, M.**, **Barros, J.**, **Rodrigues, M.R. and McLaughlin, S.W.** (2008). Wireless information-theoretic security, *IEEE Trans. on Inf. Theory*, *54*(6), 2515–2534.

[77] **Liu, X.** (2012). Probability of strictly positive secrecy capacity of the Rician-Rician fading channel, *IEEE Wireless Commun. Lett.*, *2*(1), 50–53.

[78] **Ben Yahia, O.**, **Erdogan, E.**, **Karabulut Kurt, G.**, **Altunbas, I. and Yanikomeroglu, H.** (2021). Physical Layer Security Framework for Optical Non-Terrestrial Networks, *2021 28th International Conference on Telecommunications (ICT)*, pp.162–166.

[79] **Ben Yahia, O.**, **Erdogan, E.**, **Karabulut Kurt, G.**, **Altunbas, I. and Yanikomeroglu, H.** (2022). Optical Satellite Eavesdropping, *IEEE Transactions on Vehicular Technology (early access)*, 1–6.

[80] **Erdogan, E.**, **Kabaoglu, N.**, **Altunbas, I. and Yanikomeroglu, H.** (2020). On the Error Probability of Cognitive RF-FSO Relay Networks Over Rayleigh/EW Fading Channels With Primary-Secondary Interference, *IEEE Photonics Journal*, *12*(1), 1–13.

[81] **Sarker, N.A.**, **Badrudduza, A.S.M.**, **Islam, S.M.R.**, **Islam, S.H.**, **Ansari, I.S.**, **Kundu, M.K.**, **... and Yu, H.** (2020). Secrecy Performance Analysis of Mixed Hyper-Gamma and Gamma-Gamma Cooperative Relaying System, *IEEE Access*, *8*, 131273–131285.

[82] **Pattanayak, D.R.**, **Dwivedi, V.K.**, **Karwal, V.**, **Ansari, I.S.**, **Lei, H. and Alouini, M.S.** (2020). On the Physical Layer Security of a Decode and Forward Based Mixed FSO/RF Co-Operative System, *IEEE Wireless Communications Letters*, *9*(7), 1031–1035.

[83] **Ghassemlooy, Z.**, **Popoola, W. and Rajbhandari, S.** (2019). *Optical Wireless Communications: System and Channel Modelling with Matlab*, CRC Press.

APPENDICES

APPENDIX A : Calculation of beam wander parameters

APPENDIX A: Calculation of beam wander parameters

The Fried's parameter in (4.14) is given as [13, Sect. (12)]

$$r_0 = \left[0.42\sec(\xi_{\mathscr{H}_1,S})K^2 \int_{H_{\mathscr{H}_1}}^{H_S} C_n^2(h)dh\right]^{-3/5}. \tag{A.1}$$

In uplink communication, $C_n^2(h)$ is written as

$$\begin{aligned} C_n^2(h) = {} & 0.00594\Big(\frac{u_S}{27}\Big)^2\Big(10^{-5}h\Big)^{10}\exp\Big(-\frac{h}{1000}\Big) \\ & + 2.7\times 10^{-16}\exp\Big(-\frac{h}{1500}\Big) + C_0\exp\Big(-\frac{h}{100}\Big), \end{aligned} \tag{A.2}$$

where $u_S = \sqrt{v_S^2 + 30.69v_S + 348.91}$ is the root-mean-square (RMS) of the wind speed, v_S is the wind speed in m/s, C_0 is the nominal value of C_n^2 at the receiver. Generally, C_n^2 varies from 10^{-12} $\mathrm{m}^{-2/3}$ for the strong turbulence to 10^{-17} $\mathrm{m}^{-2/3}$ for the weak turbulence [83]. In addition, $\alpha_{pe} = \frac{\sigma_{pe}}{L_{\mathscr{H}_1,S}}$ where $L_{\mathscr{H}_1,S}$ denotes the propagation distance from $\mathscr{H}_1$ to S, and σ_{pe}^2 is the beam wander-induced pointing errors variance given as

$$\begin{aligned} \sigma_{pe}^2 = {} & 0.54(H_S - H_{\mathscr{H}_1})\sec^2(\xi_{\mathscr{H}_1,S})\Big(\frac{\lambda}{2W_0}\Big)^2\Big(\frac{2W_0}{r_0}\Big)^{5/3} \\ & \times\Big[1-\Big(\frac{C_r{}^2W_0{}^2/r_0{}^2}{1+C_r{}^2W_0{}^2/r_0{}^2}\Big)^{1/6}\Big], \end{aligned} \tag{A.3}$$

where C_r is a scaling constant, which is assumed as π for $\lambda = 1550$ nm, $W = w_0\sqrt{\Theta_0^2 + \Lambda_0^2}$, where Λ_0 and Θ_0 denotes the beam parameters at the transmitter, which can be expressed as $\Theta_0 = 1 - L_{\mathscr{H}_1,S}/F_0$ and $\Lambda_0 = \frac{2L_{\mathscr{H}_1,S}}{K(w_0)^2}$. F_0 is the phase front radius of curvature at the transmitter and $\Theta = \frac{\Theta_0}{\Theta_0^2+\Lambda_0^2}$. Finally, σ_{Bu}^2 can be expressed as

$$\sigma_{Bu}^2 = 8.7\mu_{3u}K^{7/6}(H_S - H_{\mathscr{H}_1})^{5/6}\sec^{11/6}(\xi_{\mathscr{H}_1,S}), \tag{A.4}$$

where μ_{3u} is given as

$$\mu_{3u} = \Re\int_{H_{\mathscr{H}_1}}^{H_S} C_n^2(h)[i\varepsilon(1-\varepsilon)]^{5/6}dh, \tag{A.5}$$

and ε is the normalized distance variable given as $\varepsilon = 1 - (h - H_{\mathscr{H}_1})/(H_S - H_{\mathscr{H}_1})$ for the uplink communication.

CURRICULUM VITAE

Name Surname : Olfa BEN YAHIA

EDUCATION :

- **B.Sc.** : 2013, Applied License in information and communication science and technology in the Institute of Electronics and Communication of Sfax, Tunisia
- **BENG.** : 2016, Telecommunications Engineering Degree in the National School of Electronics and Telecommunications of Sfax, Tunisia

PROFESSIONAL EXPERIENCE AND REWARDS:

- Graduation Project: Huawei Tunisia: 01/2016 to 05/2016:
  Dimensioning, planning, and optimization of LTE Networks using Huawei's software
- Internship Student: ND for Web Company: 07/2015 to 08/2015:
  Develop an SMS application using Visual Basic
- Internship Student: Tunisian Company of Electricity and Gas (STEG): 07/2014 to 08/2014:
  Data base Project with "WinDev17"
- Graduation Project: ENET'COM: 02/2013 to 05/2013:
  Configuration, installation, and deployment of VoIP server (CISCO UC500)
- Internship Student: Tunisia Telecom: 06/2012 to 07/2012:
  Monitoring the actions of the Transmission Center and supervision of the stations linked to the CTN

PUBLICATIONS, PRESENTATIONS AND PATENTS ON THE THESIS:

- Journals

    1. **O. Ben Yahia**, E. Erdogan, G. Karabulut Kurt, I. Altunbas, and H. Yanikomeroglu, "A weather-dependent hybrid RF/FSO satellite communication for improved power efficiency", *IEEE Wireless Communications Letters*, vol. 11, no. 3, pp. 573–577, 2022.
    2. **O. Ben Yahia**, E. Erdogan, G. Karabulut Kurt, I. Altunbas, and H. Yanikomeroglu, "HAPS selection for hybrid RF/FSO satellite networks", *IEEE Transactions on Aerospace and Electronic Systems* (early access), pp. 1–13, 2022.
    3. **O. Ben Yahia**, E. Erdogan, G. Karabulut Kurt, I. Altunbas, and H. Yanikomeroglu, "Optical Satellite Eavesdropping", IEEE Transactions on Vehicular Technology (early access), pp. 1–6, 2022.
    4. **O. Ben Yahia**, E. Erdogan, G. Karabulut Kurt, "HAPS-assisted Hybrid RF-FSO Multicast Communications: Error and Outage Analysis", IEEE Transactions on Aerospace and Electronic Systems (early access), pp. 1-13, 2022.

- International Conferences

    1. **O. Ben Yahia**, E. Erdogan, and G. Karabulut Kurt, "On the use of HAPS to increase secrecy performance in satellite networks", in *IEEE International Conference on Communications Workshops (ICC Workshops)*, 2021, pp. 1–6.
    2. **O. Ben Yahia**, E. Erdogan, G. Karabulut Kurt, I. Altunbas, and H. Yanikomeroglu, "Physical layer security framework for optical non-terrestrial networks", in *International Conference on Telecommunications (ICT)*, 2021, pp. 162–166.

- Presentations

    1. **O. Ben Yahia**, Oral Presentation, in *2021–2022 Carleton 6G Workshop*, Ottawa, ON, Canada.

OTHER PUBLICATIONS, PRESENTATIONS AND PATENTS:

1. **O. Ben Yahia**, E. Erdogan, G. Karabulut Kurt, I. Altunbas, and H. Yanikomeroglu, "Secure RF/FSO Communications Towards the 6G Era", in *IEEE Tech Focus on Security and Privacy*, accepted.

2. M. Y. Abdelsadek, A. U. Chaudhry, T. Darwish, E. Erdogan, G. Karabulut Kurt, P. G. Madoery, **O. Ben Yahia**, and H. Yanikomeroglu, "Future Space Networks: Toward the Next Giant Leap for Humankind", in *IEEE Transaction On Communications*, under review.